Heterogeneous Photocatalysis and Sensitized Photolysis for Enhanced Degradation of Bisphenol A and its Analogues

zur Erlangung des akademischen Grades eines

DOKTORS DER NATURWISSENSCHAFTEN

(Dr. rer. nat.)

Fakultät für Chemie und Biowissenschaften

Karlsruher Institut für Technologie (KIT) - Universitätsbereich

genehmigte

DISSERTATION

von

Diplom-Chemiker Aleksandr O. Kondrakov

aus Rjasan

Dekan: Prof. Dr. Peter Roesky
Referent: Prof. Dr. Stefan Bräse
Korreferent: Prof. Dr. Fritz H. Frimmel
Tag der mündlichen Prüfung: 13. Februar 2015

Contents

1 Introduction

1.1 Motivation

This is a study of degradation of bisphenols (BPs) by TiO_2 photocatalysis and natural organic matter-(NOM)-sensitized photolysis. BPs are represented here by bisphenol A (BPA) and its three analogues – bisphenol F (BPF), bisphenol S (BPS) and bisphenol AF (BPAF). These four BPs form a weighty group of high production volume chemicals for polymer industry; the global annual demand of BPs currently exceeds the value of 5.4 million tons [1]. Because of their extensive use and scarce environmental regulations, BPs became ubiquitous micropollutants in the aquatic environment. BPs and their degradation intermediates can provoke diverse developmental abnormalities in aquatic organisms already at environmentally relevant doses [2]. Wastewater effluents and landfill leachates were found to be the primary sources of BPs in surface waters [3, 4]. Moreover, it has been demonstrated that BPs are pseudo-persistent pollutants, which means that their continuous release causes their permanent presence in the aquatic environment despite the rapid degradation rates [2–8]. Today, there are only a few competitive environmentally friendly analogues of BPs-based polymers and a BPs production drop is therefore not expected. In this perspective, protection of the aquatic environment against pollution caused by BPs is an issue of paramount importance.

Advanced oxidation processes (AOPs) are a group of chemical oxidation methods exploiting high oxidation power of *in-situ* generated OH radicals (·OH) for wastewater treatment. When properly developed, AOPs provide the most optimal solution for the problem of micropollutants – their complete mineralization. Typically, ·OH can be generated out of hydrogen peroxide, ozone and water by UV photolysis or in auto- and photocatalytic processes. Heterogeneous TiO_2 photocatalysis utilizes the energy of solar light for ·OH generation and can essentially excel the H_2O_2/O_3-based AOPs in energy efficiency [9–11]. Though TiO_2 photocatalysis is an attractive method for elimination of BPs from contaminated water, there is still a lack of knowledge on several fundamental aspects, which constrains its further development. These aspects are related to the chemistry of

photocatalytically generated ·OH. Particularly, it is not completely clear which site is responsible for ·OH formation and in which chemical form ·OH may exist [12, 13]. If ·OH exists in a form of a TiO_2 surface hydroxyl group conjugated with a photogenerated valence band hole (h^+_{VB}), then oxidation of a pollutant proceeds via electron transfer and the overall efficiency of the process is controlled by adsorption. If ·OH results from reactive oxygen species (ROS) in bulk solution, then the oxidation can proceed far off the TiO_2 surface. All the other components of an aqueous matrix can therefore affect the process efficiency. Most of the data indicate that both of the mechanisms can take place [14]. However, their relative roles in the overall process performance are not clear [15]. Thus, the knowledge on the mechanisms of the ·OH generation and the ROS reactions occurring later on should serve as a basis for design of highly efficient photocatalytic treatment of BPs contaminated water and should be therefore improved.

Once the rest amounts of a contaminant are released from a wastewater treatment plant into the water body, the natural processes of biodegradation and sunlight photolysis can take place. In natural waters, the largest fraction of the UV-vis light in the photic zone is absorbed by NOM in both its dissolved and particulate forms [16]. NOM may act as a photosensitizer and can drastically accelerate photolysis of aqueous contaminants [17]. Currently, the data on BPs photolytic transformations in natural waters are scarce. Model experiments in natural-like conditions show that BPA sunlight photolysis can be essentially enhanced by the presence of various photosensitizers, such as Suwanee fulvic acid or riboflavin [18, 19], but little is known about photolysis of BPA analogues. In view of ubiquitous presence, potential of persistence and hazardous effects of BPs and their products, kinetics and mechanism of their photosensitized degradation in natural-like conditions need to be given more attention. It seems to be especially important to improve the knowledge on the environmental fate of potentially highly stable fluorine containing BPs, such as BPAF.

1.2 Goals of the Study

In summary, this work deals with elucidation of BPs transformations occurring in the processes of TiO_2 photocatalysis, UV photolysis and NOM-sensitized photolysis. In view of the extensive evidences on the ubiquitous environmental presence of BPA and plausible genotoxicity of its by-products [20–29], the potential of TiO_2 photocatalysis and UV photolysis for degradation of BPA (as the most relevant BPs representative by now) was studied. A special attention was paid to elucidation of the mechanism of photocatalytic

generation of ROS in order to explore their sources, amounts and roles in the degradation process. Today, there is a great lack of knowledge concerning environmental transformations of BPA and its analogues, such as BPS, BPF and BPAF. Therefore, the kinetics and mechanisms of the degradation of these BPs by NOM-sensitized photolysis were studied in this work well. The main goals of the study were therefore identification of BPs intermediates and analysis of the BPs degradation kinetics as well as elucidation of the mechanisms of ROS generation in these processes. Particularly in this thesis:

- section 3.1 presents the investigation of the mechanisms of BPA degradation by the processes of TiO_2 photocatalysis and direct UV photolysis at λ= 254 nm. An accurate HPLC-MS-MS/ToF analysis was used to identify the formed intermediates and to explore potentials of generation of undesirable BPA intermediates, such as genotoxic BPA-quinones. A special attention was payed to the differences in composition of BPA intermediates generated via ·OH- and h^+_{VB}-mediated photocatalytic oxidation. For this, the experiments with tert-butanol (tBuOH) as a selective ·OH scavenger were conducted.

- section 3.2 describes the results on an isotopic labeling study of the reactions of free ·OH (·OH_{free}) generated in the process of TiO_2 photocatalysis. Photocatalytic degradation of a probe compound, 1,3,5-trichlorobenzene (TCB), adsorbed in pores of SG microparticles, was used for estimation of the quantum yield of ·OH_{free} generation. The small diameter (4 nm) of the SG pores prevented penetration of the TiO_2 particles (25 nm in size) to the adsorbed TCB. Therefore, the TCB degradation was driven by reaction with ·OH_{free}, but neither with h^+_{VB} nor ·OH adsorbed on the TiO_2 surface (·OH_{surf}). The details of the ·OH_{free} generation mechanism were investigated in the experiments with $^{18}O_2$ and scavengers for ·OH and h^+_{VB}.

- in section 3.3, the results of the study on BPs degradation by photolysis sensitized by HO24 (an NOM sample isolated from the boggy lake Hohloh) are presented. Photolability of BPs was assessed comparing the rates of HO24-sensitized and direct photolysis under simulated solar light. Influence of inorganic constituents, such as Fe^{3+}, NO_3^- and HCO_3^-, was assessed at the concentrations, typical for surface waters. A combination of the HPLC-MS-MS/ToF and SEC-DOC/UV/FL methods with the experiments on kinetic isotope effects of $^{18}O_2$ and D_2O was implemented to study the ROS formation mechanism.

2 Background

2.1 Bisphenol A (BPA) and its Analogues

BPs are diphenylmethane derivatives with two hydroxyl groups on aromatic rings (Figure 2.1). They exhibit an endocrine-disrupting action and can hazardously affect aquatic species already at the concentrations below 1 µg L^{-1} [2].

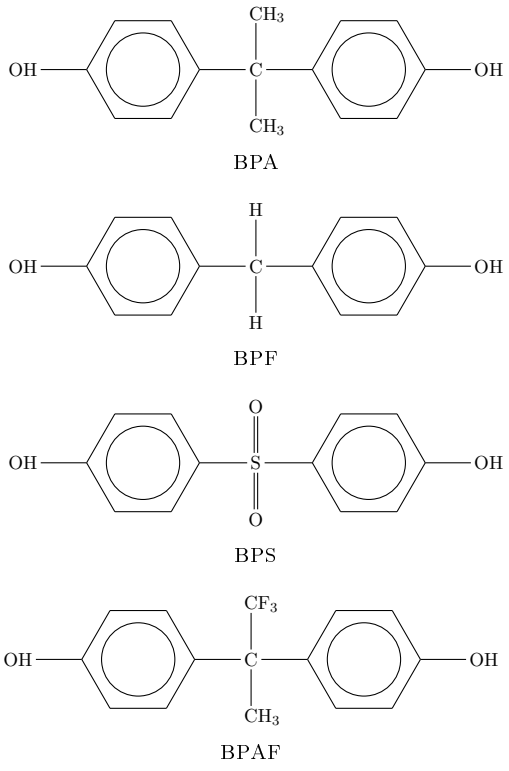

Figure 2.1: Structures of the primarily used BPs.

It was demonstrated that the BPs concentrations in surface waters are closely related to the BPs amounts in the industrial wastewater plants effluents [3–8]. In spite of the growing environmental risks, BPs are the chemicals of a very extensive industrial use and their complete ban can not be currently expected. The following section describes

the areas of the BPs primary use and summarizes available data on the BPs production volumes.

2.1.1 Applications and Production Volumes

BPs are important materials for polymer industry; they are used as monomers, plastisizers, preservers and color developers [30]. BPs-based polymers exhibit excellent mechanical, thermal and optical properties, good durability and high chemical resistance. The major part of BPs is utilized in manufacturing of BPA polycarbonates (PCs). Excellent mechanical properties of BPA PCs became the benchmark for the engineering thermoplastics. Due to its structure, the BPA PC polymer chain can efficiently dissipate excess of energy produced by an impact. The loss of mechanical energy is facilitated by flip motions of BPA units around the carboxyl groups in internal polymer volume, which preserves the PC material from breaking [30].

Light and durable BPA containing materials and BPA-based polymers are present in many consumer products, including food and beverage containers [31–34]. Misgivings about safety of the BPA use in food contact applications, especially for infant nutrition, stimulated an intensive search for BPA alternatives, such as BPS, BPF and BPAF. In 2012, BPA has been banned from baby bottles in the European Union and the US and thermally printed cash receipts in Japan [35, 36]. Many manufacturers switched to using the analogues of BPA in order to comply with arising regulations. Products containing the BPA analogues were marked as “BPA free” and introduced to the market [37]. New regulations provoked the replacements of BPA by its analogues in consumer products, but did not induced a slow down of the BPs market. On the contrary, it has shown 10% growth [39]. Today, BPA is one of the mostly produced organic chemicals with a global demand of 5.4 million tons [39]. According to the US Environmental Protection Agency (US EPA) data, the US production volumes of BPS, BPF and BPAF are remarkably lower in comparison to BPA (Figure 2.2). Unfortunately, data on the global demand of BPS, BPF and BPAF are incomplete. BPS is gradually replacing BPA in thermal printing applications and can serve as an alternative PCs monomer [40]. BPF is a monomer for PCs production on a par with BPA and sometimes BPF- and BPA-based polymers are used in the mixture [41, 42]. Incorporation of BPAF as a comonomer in PC chain improves thermal and chemical properties of a material and is used in special polymer applications, such as high-temperature composites for electronics [43, 44].

Today, scarce environmental regulations do not restrict direct discharges of BPs into the aquatic environment [45]. Moreover, extremely high production volumes accentuate

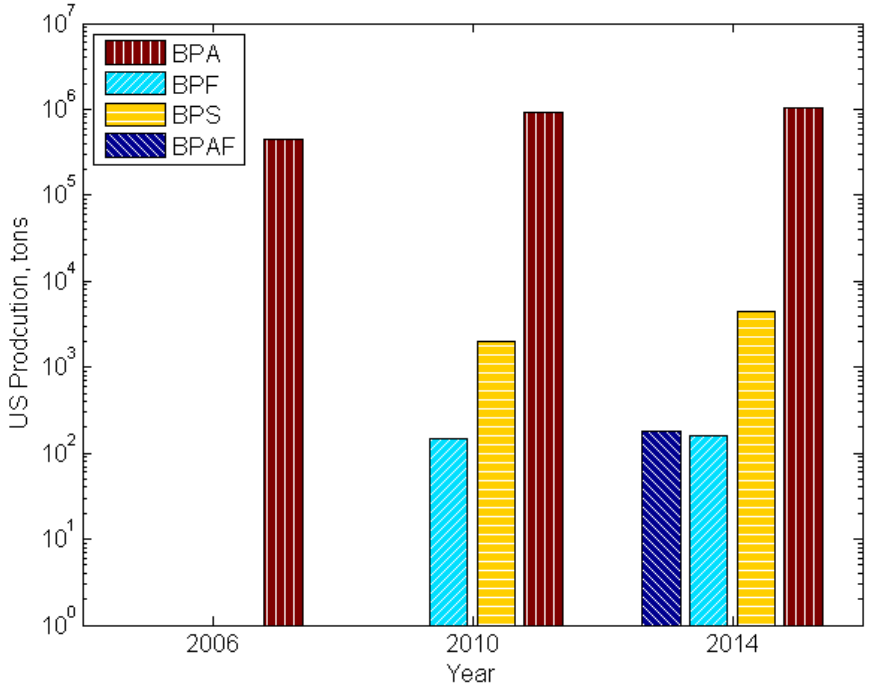

Figure 2.2: Production volumes of BPA and its analogues in the United States [38].

the utilization problem and can cause permanent presence of BPs in the water body. Continuous exposure of wildlife to BPs posses a threat to highly sensitive aquatic ecosystems and requires an urgent assessment of the risks we are faced.

2.1.2 Environmental Occurence and Risks

BPs were not considered as hazardous chemicals during the long period of their intensive use. Manufacturers and researchers were not aware of direct surface water discharges over decades, since acute toxicity and potential of persistence of BPs were reported to be relatively low [38]. Although estrogenic activity of BPA and other diphenylmethane derivatives were already known in 1936 [46], the first cases of BPA induced developmental abnormalities were reported only in the early 1980s [47]. Later, reports on possible migration of BPA residues from PC material into food and beverages [48], raised concerns about safety of the BPA use and stimulated extensive monitoring of BPA and other BPs in the environment. It has been demonstrated that BPs are pseudo-persistent pollutants, which means that a continuous release causes their permanent presence in the aquatic environment despite the rapid degradation rates [2].

Wastewater effluents and landfill leachate are the primary sources of BPs in the water body [3, 4, 49]. Distribution of BPs after release can be estimated on the base of their

physicochemical properties. All the BPs considered, have low volatility (vapor pressure between 7.09×10^{-3} and 4.72×10^{-10} mm Hg at 25 °C) and low or moderate hydrophobicity ($\log K_{ow}$ between 1.6 and 4.47) and are therefore expected to remain in water and sediments [38]. Rates of biodegradation and degradation by photolysis define steady-state environmental levels of BPs and, thus, a potential of persistence. Absorption spectra of different BPs are very similar, but do not overlap with the spectrum of terrestrial solar irradiance [50–52], so the photolysis is expected to be significantly slower than biodegradation. Biodegradation of BPA, BPF and BPS requires from 1 to 10 weeks [38], however some of the metabolites can be more persistent [53]. BPAF is a very persistent chemical with low biodegradability rate and may retain up to 180 days in water and up to 360 days in soil (estimated by the US EPA "PBT Profiler" [54]). Data on typical environmental BPs concentrations are summarized in Table 2.1.

Though quantification of BPs health effects at low doses still evokes some controversies, they are without doubt representative endocrine-disrupting chemicals (EDCs) [43, 44, 59–64]. EDCs interact with an endocrine system and disrupt the functions it controls [65, 66]. Due to similarities in molecular structures (Figure 2.3), EDCs mimic hormones and induce receptors response [67–69]. For example, BPA activates estrogen receptors (ERs), ERα and ERβ, by imitating 17β-estradiol (E_2) [70]. Activated ERs bind DNA and regulate the expression of specific genes, thereby controlling growth and developments of tissues [71, 72]. Irruption of BPs in the hormone regulation can result in neural and behavioral dysfunctions and negatively affect reproduction and fertility [73, 74].

Whereas mammalian and human toxicity of BPs, especially of BPA, are well documented phenomena [75], the knowledge on the BPs effects on aquatic environment and wildlife remains scarce. *In-situ* determinations of the BPs toxicity to the aquatic wildlife is a very challenging task. Concentration of BPs can vary spatially and temporally [76, 77], which may result in non-uniform exposure of different species. Their susceptibility to BPs can also change seasonally [2]. If an organism is affected in the periods of development and growth, the risk of abnormalities increases, although they are not obviously expressed and may be only observed at mature stages [2]. Today, data on aqueous hazard assessment of BPS, BPF and BPAF are lacking and only BPA effects have been investigated, though BPs estrogenic activities are very similar [5]. Laboratory studies demonstrate that some of the aqueous species can be hypersensitive to BPA and experience developmental abnormalities at environmentally occurring exposure levels [78–86]. Particularly, 1 µg L^{-1} of BPA has resulted in superfeminization (additional female organs, enlarged and deformed oviduct) and increased mortality of freshwater ramshorn snail [2,

Table 2.1: Global environmental occurrence of BPs in waters (µg L^{-1}) and sediments (µg in kg of dry weight). Locations are denoted by ISO 3166 country codes.

Compound	Wastewater effluents	Surface waters	Groundwaters	Sediments
BPA	0.2-17200, JP [20, 21]	0.07-4.0, PT [22]	1-1.9, US [23]	1.1-56, NE [24]
	<0.02-5.62, NL [24]	0.0088-1.0, NL [24]	0.05-0.18, ES [25]	0.7-27.3, CN [55]
	0.11-1.7, US [23]	0.06-0.33, JP [26]		n.d.-2.7, JP [56]
	n.d.-1.054, CA [57]	0.0015-0.262, CN [55]		
		n.d.-0.147, US [27]		
		0.0005-0.014, DE [28]		
BPF	0.022-0.123, DE [42]	0.0001-0.180, DE [42]		1.2-7.3, DE [42]
BPS				n.d.-4.65, US [58] n.d.-4.46, JP [58] n.d.-1970, KO [58]
BPAF	n.d.-15.3, CN [8]		n.d.-0.3, CN [8]	0.52-2000, CN [8]

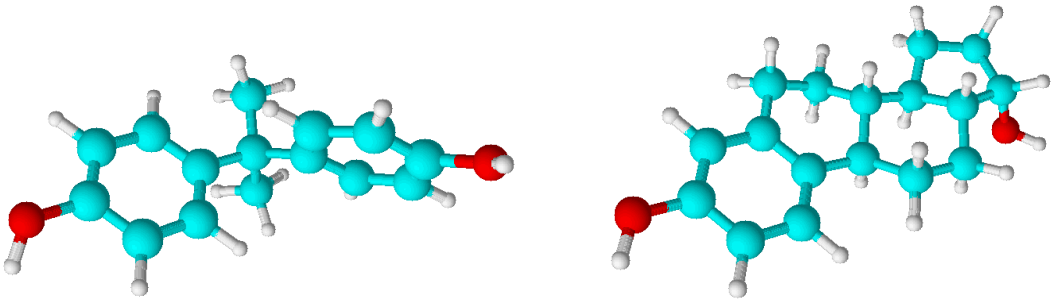

(a) (b)

Figure 2.3: Three-dimensional structures of BPA (a) and 17β-estradiol (b) [30].

87]. BPA inhibits development of marine copepods at 0.08 µg L^{-1} [88] and suppresses estrogen synthesis of longchin goby at 0.1 µg L^{-1} [2, 89].

These studies show that BPA can be harmful to aquatic biota at environmentally relevant concentrations. A predicted no-effect concentration (PNEC) of BPA has been recently reassessed and lowered from 100 µg L^{-1} to 0.02 µg L^{-1} [2]. Table 2.1 shows that alone for BPA, the environmental concentrations frequently reach much higher values than PNEC, which means that the health of dozens of sensitive aquatic species can be continuously affected. In this context, urgent strengthening of the BPs regulations and development of remediation strategies are issues of high importance.

2.1.3 Remediation Strategies

European water quality directive 2008/105/EC states:
"As a matter of priority, causes of pollution should be identified and emissions should be dealt with at source, in the most economically and environmentally effective manner."
In this directive, BPA receives special attention and is suggested to be concerned as a priority hazardous substance or priority substance. Another European directive 2008/105/EC is aimed at chemical protection of the aquatic environment by reducing emissions of priority hazardous substances. In view of similarities of BPs harmful effects [5], overall BPs emissions should be minimized as well. This aim may be achieved by shortening of the BPs production volumes and by efficient removal of BPs from wastewater.

There are several competitive analogues of BPs containing polymers, but BPs are apparently ideal raw materials in production of high-quality engineering thermoplastics and it seems to be unrealistic to find a universal non-toxic alternative at the moment [90]. BPA-based PCs can be replaced by poly(cyclohexane carbonate) in low impact applica-

tions or by copolyesters based on *cis*- and *trans*-2,2,4,4-tetramethyl-1,3-cyclobutanediol. Replacements of BPA in epoxy resins require an individual solution for each particular use [30]. Most of these alternative polymers are designed for food contact applications, but they still can not compete with BPs-based polymers in other areas of use. A drop in BPs production is therefore not to be expected. In this perspective, efficient removal of BPs from industrial and domestic wastewater arises as an important task.

Table 2.1 shows that conventional wastewater treatment plants are in many cases not capable to efficiently eliminate BPs without additional pretreatment steps [91, 92]. Performance of a typical wastewater treatment plant is measured by percentages of reduction of biological oxygen demand, chemical oxygen demand and total suspended solids [93], which does not always reflect efficiency of micropollutants removal [94]. In addition, the data on BPs wastewater occurrence suggest that wastewater treatment plant effluents continuously introduce BPs in surface waters at microgram-per-litre concentrations [95], which can be harmful for aquatic biota [2, 83, 87, 88].

AOPs belong to the group of chemical oxidation methods exploiting the high oxidizing power of ·OH for the wastewater treatment. The great advantage of AOPs over the conventional phase separation methods (sedimentation, absorption, filtration) lies in the possibility of complete mineralization of the pollutants [96–103]. ·OH has a redox potential of 2.8 eV and is able to oxidize most of the organic compounds [104]. AOPs differ from each other in the respect of the mean of ·OH generation. Typically, ·OH can be generated out of hydrogen peroxide, ozone and water by UV photolysis or in auto- and photocatalytic processes [96].

One of the simplest methods of ·OH generation is a direct UV photolysis of hydrogen peroxide. Though H_2O_2 is a thermodynamically unstable compound, its UV photolysis rate is very low [105]. Because of different geometries of the ground and excited states of a H_2O_2 molecule [106], quantum selection rules forbid electronic transitions induced by 250-380 nm light, which results in a very weak UV absorption ($\varepsilon_{H_2O_2} = 19\ M^{-1}\,cm^{-1}$ at 254 nm [107]). H_2O_2 decomposition can be enhanced by use of Fe^{2+}-salts as a catalyst (UV-Fenton treatment) [108] or ozone as a radical initiator (UV-H_2O_2-O_3 hybrid treatment) [99]. In practice, energy efficiency of these processes is low, because they require a continuous input of expensive reagents and UV light [109]. Particularly, in the Fenton catalytic cycle, Fe^{2+}-ions can be hydrated and lost by precipitation [110]. On the other hand, ozone is an expensive and highly reactive reagent; its generation is possible *in-situ* only and is attended by considerable energy losses at the conductor/insulator interface [111].

2.2 Heterogeneous Photocatalysis with TiO_2

The global annual energy demand is roughly equivalent to the amount of the solar light energy reaching the earth surface every hour [112, 113]. Heterogeneous photocatalysis utilizes the energy of solar light for ·OH generation and may excel the H_2O_2/O_3-based AOPs in energy efficiency. More rigorously, photocatalytic oxidation is primarily driven by electron-hole pairs photogenerated at a photocatalyst surface, which further form ·OH and other ROS [12, 13]. Though researchers have not reached consensus on all the mechanistical aspects of photocatalysis, its basics deserve to be elucidated in detail.

2.2.1 Electronic Excitation in Semiconductors

TiO_2 is a broadly used material for heterogeneous photocatalysis due to its wide band gap, chemical stability, non-toxicity and low cost. Photoexcitation of a TiO_2 crystal by photon absorption is the primary event in the process of photocatalytic oxidation, so understanding of electronic properties of TiO_2 is of fundamental importance here.

TiO_2 is a semiconductor, which is a material with electrical conductivity between those of conductors and insulators. Electrical conductivity of semiconductor materials is related to their *band* structure of electronic energy states. For a crystal, electrons can be characterized by a quantum mechanical Bloch's theorem [114]. Atoms of the crystal are periodically located in a lattice and create a periodic potential, which effects electrons. In other words, electrons are in an electrical field, which has the same periodicity $\mathbf{k}$ as the crystal. If we define behavior of electrons by their wavefunctions $\psi(\mathbf{r})$ and take into account the periodic potential, we obtain Equation 2.1, which expresses the resultant electronic states.

$$\psi(\mathbf{r}) = \mathrm{e}^{\mathrm{i}\mathbf{k}\cdot\mathbf{r}} u(\mathbf{r}) \tag{2.1}$$

where $\mathbf{r}$ is a coordinate; $u(\mathbf{r})$ is a function reflecting the periodicity of the potential; $\mathrm{e}^{\mathrm{i}\mathbf{k}\cdot\mathbf{r}}$ is a phase factor, which arises due to a complex-valued nature of the wavefunction.

For the crystal containing a large number of atoms (order of 10^{20} cm^{-3}), the number of Equation 2.1 solutions also becomes large. These discrete energy levels become very closely spaced and form continuous electronic energy *bands*. Figure 2.4 shows differences in the band structures of metals, semiconductors and insulators. In metals, the highest occupied band is only partially filled and some fraction of the electrons is able to absorb available thermal energy ($k_BT \approx 0.025$ eV at 300 K) [115]. These electrons are so called *free electrons*, which do not participate in chemical bonding and provide sufficient electrical

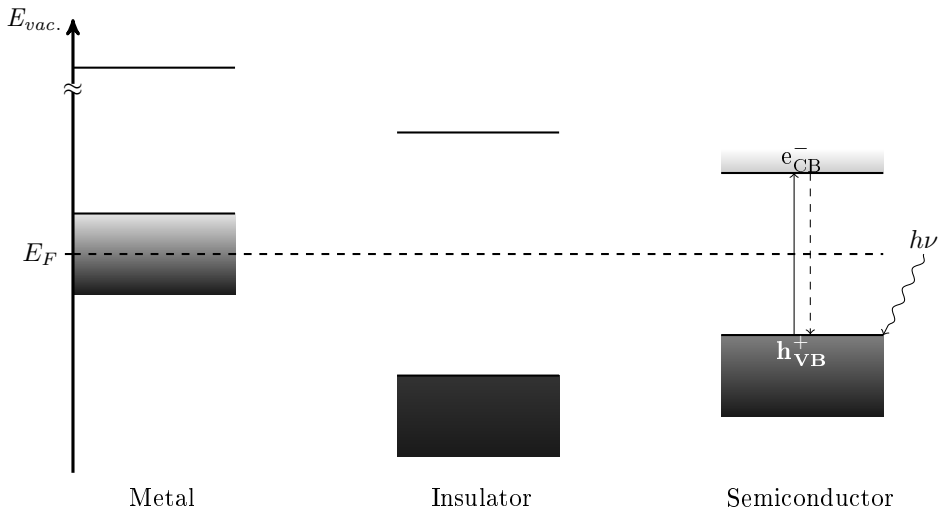

Figure 2.4: Electronic band structure of different types of materials.

conductivity under normal conditions [116]. The electronic bands of semiconductors and insulators are either completely filled or completely empty and separated by a band gap [114]. The closest bands beneath and above the band gap are called *a valence band* (VB) and *a conduction band* (CB), respectively. A minimal amount of the energy required for an electron transition across the band gap is determined by the band gap width [9, 116]. In wide-band gap semiconductors, such as TiO_2, the band gap width is in an energy range similar to that of visible and UV light and the electronic transitions can be driven by photon absorption [10].

Once photoexcitation of the semiconductor occurs, pairs of CB electrons (e^-_{CB}) and VB holes (h^+_{VB}) are generated. h^+_{VB} are indeed positively-charged quasi-particles corresponding to the empty VB states resulted from the electron transitions across the band gap (Figure 2.4). h^+_{VB} and e^-_{CB} mediate the processes of electron transfer between the TiO_2 surface and adsorbed species. The process of photoexcitation and electron transfer are accompanied by an e^-_{CB}-h^+_{VB} recombination. Whereas the photoexcitation happens within a few fs, the recombination proceeds orders of magnitudes slower, which maintains a steady-state concentration of e^-_{CB}-h^+_{VB} pairs. By the analogy of the free electrons in metals, photogenerated e^-_{CB} and h^+_{VB} are mobile and can migrate throughout the crystal. If h^+_{VB} and e^-_{CB} become spatially separated, they can be trapped inside the crystal or at the crystal surface and recombination is suppressed [117, 118]. Therefore trapping at the semiconductor surface maintains a steady-state concentration of h^+_{VB} and e^-_{CB}, whose amounts define the photocatalytic activity [11, 119].

2.2.2 Photocatalytic Generation of Reactive Oxygen Species (ROS) at TiO_2 Surface

The most commonly used commercial TiO_2 photocatalyst is the AEROXIDE® P25 (hereafter labeled as P25) nanoparticles powder from Evonik (former Degussa), which consists of anatase and rutile 25 nm crystallites in a ratio about 3:1. Apparently, enhanced separation of the e^-_{CB}-h^+_{VB} pairs between the phases and efficient trapping at the large surface are the reasons, why the mixed-phase nanosized P25 has higher photocatalytic activity compared to the single-phase bulk TiO_2 [120–127].

Surface science sheds light on the mechanistic aspects of the e^-_{CB}-h^+_{VB} pairs behavior in nanosized TiO_2. By the use of a set of such powerful methods as scanning tunneling microscopy (STM) and density functional theory calculations (DFT), the phenomena of the charges transfer and trapping at the TiO_2 surface can be investigated in detail.

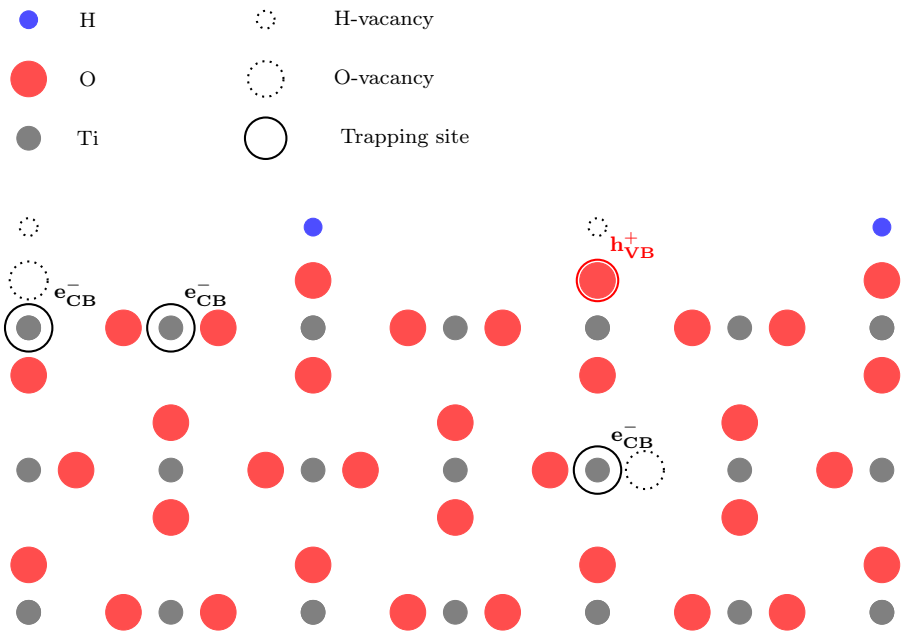

Figure 2.5: Possible trapping sites in a TiO_2 rutile crystal.

DFT calculations predict different mobility and spatial distribution of h^+_{VB} and e^-_{CB} in the TiO_2 crystal, because they differently interact with the surrounding lattice atoms [124, 128–130]. h^+_{VB} seem to be more mobile and tend to be trapped at Ti^{4+}–O^- surface sites, whereas e^-_{CB} can be trapped either on Ti atoms of a subsurface (one level beneath) or in a form of uncoordinated Ti^{3+} surface sites [131] (Figure 2.5). STM measurements

Table 2.2: Characteristic times of the photon-induced events in TiO_2 [135, 136].

Event	Characteristic time
Photon absorption	<fs
e^-_{CB}-h^+_{VB} pairs generation	fs
e^-_{CB} trapping	0.1-10 ns
h^+_{VB} trapping	10 ns
e^-_{CB}-h^+_{VB} recombination	10-100 ns
e^-_{CB} transfer	0.1-1 µs
h^+_{VB} transfer	10-100 ns

demonstrate that crystal defects, e.g. oxygen vacancies, are the primary traps for e^-_{CB} [15, 132]. Oxygen vacancies prevent e^-_{CB}-h^+_{VB} recombination by stabilizing the excess of e^-_{CB} even if there are no other electron acceptors available [133, 134]. Trapped h^+_{VB} and e^-_{CB} drive the photocatalytic process mediating the electron transfer at the interface between the TiO_2 surface and the adsorbed species [137]. If the adsorbed species is an electron acceptor, it receives the e^-_{CB}; if it is an electron donor, it injects an e^-_{CB} to the h^+_{VB}. Kinetics of these redox processes strongly depend on the structure of an intermediate state, formed at the interface TiO_2/adsorbate [138].

Table 2.2 gives an overview of characteristic times of the generation, trapping and charge transfer processes. Typically, a h^+_{VB}-mediated oxidation occurs on a nanosecond timescale, whereas a e^-_{CB}-driven reduction is slower and occurs on the microsecond timescale [135, 136]. In terms of photocatalytic treatment, the reduction by e^-_{CB} is considered as an e^-_{CB} scavenging, since it competes with the recombination process and favors the steady state concentration of h^+_{VB} for oxidation. In presence of dissolved O_2, these processes are even more strongly interconnected, because O_2 serves both as an e^-_{CB} scavenger and as a source of ROS, e.g. $\cdot OH_{free}$ [138]. It means that photocatalytic oxidation with TiO_2 is not a pure heterogeneous process *per se*, but it is accompanied by ROS-driven homogeneous oxidation. There are still a lot of debates about the relative roles of ROS and h^+_{VB} in photocatalytic oxidation [12, 13], so this issue is addressed here in more detail.

In contrast to surface-trapped h^+_{VB}, $\cdot OH$ can exist in both surface-bound and free forms [14]. The surface-bound $\cdot OH$, $\cdot OH_{surf}$, is indeed an electron-deficient titanol group, $>Ti{-}OH\cdot$, formed in the h^+_{VB}-mediated electron transfer reaction (1):

$$>Ti{-}OH^- + h^+_{VB} \longrightarrow >(Ti{-})\cdot OH_{surf} \qquad (1)$$

Mechanism of the $\cdot OH_{free}$ formation is more complex; it involves both ROS reactions in solution and the electron transfer at the TiO_2 surface [139]. O_2 is the main precursor in all the cases: it captures e^-_{CB} forming a hydroperoxyl radical, $HO_2\cdot$, (2), which initiates a cascade of fast ($k \approx 10^6 - 10^{10}$ M s^{-1}) radical reactions (3)-(7):

$$O_2 + e^-_{CB} + H^+ \longrightarrow HO_2\cdot \tag{2}$$

$$HO_2\cdot + HO_2\cdot \longrightarrow H_2O_2 + O_2 \tag{3}$$

$$H_2O_2 \xrightarrow{h\nu} 2\cdot OH \tag{4}$$

$$\cdot OH + H_2O_2 \longrightarrow H_2O + HO_2\cdot \tag{5}$$

$$HO_2\cdot + \cdot OH \longrightarrow H_2O + O_2 \tag{6}$$

$$\cdot OH + \cdot OH \longrightarrow H_2O_2 \tag{7}$$

At the TiO_2 surface, $HO_2\cdot$ undergoes stepwise reduction by e^-_{CB}, finally forming $\cdot OH_{free}$:

$$HO_2\cdot + e^-_{CB} + H^+ \longrightarrow H_2O_2 \tag{8}$$

$$H_2O_2 + e^-_{CB} \longrightarrow \cdot OH + OH^- \tag{9}$$

Estimation of the concentrations of ROS and h^+_{VB} is a challenging task. Rates of interfacial reactions (2), (8) and (9) depend on adsorption ability of single ROS and on the availability of the surface sites at which e^-_{CB} is localized [140]. Furthermore, the overall rate of generation of $\cdot OH_{free}$ via ROS radical chain reactions (2)-(9) is pH dependent, since dissociated and protonated forms of $HO_2\cdot$ and H_2O_2 have drastically different reactivity [104, 141, 142].

Nevertheless, understanding of ROS chemistry is important, since ROS are involved both in generation of $\cdot OH_{free}$ and in electron transfer at the TiO_2 surface. In this connection, the following section overviews existing kinetics models, which are aimed at a

quantitative description of photocatalytic oxidation, and highlights the questions, which still remain open.

2.2.3 Existing Models and Open Questions

By analogy with ordinary heterogeneous catalysis, many authors have claimed that kinetics of photocatalytic reactions on TiO_2 conforms with the Langmuir-Hinshelwood (L-H) mechanism [143–153]. The L-H mechanism postulates that adsorption (10) is a rapid prerequisite event, whereas the following single reaction at an "active site" S is a slow, rate-limiting step (11).

$$\mathrm{A} + \mathrm{S} \underset{k_{-1}}{\overset{k_1}{\rightleftharpoons}} \mathrm{AS} \tag{10}$$

$$\mathrm{AS} \xrightarrow[(slow)]{k_{app.}} \mathrm{PS} \tag{11}$$

In this consideration, equilibrium of adsorption (10) is expressed by the Langmuir adsorption equation (Equation 2.3) and the overall reaction rate is determined by the rate of reaction (11):

$$r = -\frac{d[\mathrm{AS}]}{dt} = k_{app.}[\mathrm{AS}] \tag{2.2}$$

$$\theta = \frac{[\mathrm{AS}]}{[\mathrm{S_0}]} = \frac{K[\mathrm{A}]}{1 + K[\mathrm{A}]} \tag{2.3}$$

where [AS] is the concentration of an adsorbed reactant; $k_{app.}$ is an experimental pseudo-first-order rate constant of the reaction (11); θ is a term of a fractional surface coverage; $[\mathrm{S_0}]$ is the total concentration of active sites; $K = k_1/k_{-1}$ is an equilibrium constant of adsorption (10) and [A] is the concentration of an non-adsorbed reactant.
Consequently, the term of adsorbed reactant concentration [AS] can be expressed by means of Equation 2.3 and the resulting L-H kinetic equation is thus:

$$r = -k_{\text{L-H}} \frac{K'[\mathrm{A}]}{1 + K'[\mathrm{A}]} \tag{2.4}$$

where K' is an apparent adsorption constant and $k_{\text{L-H}} = k_{app.}[\mathrm{S_0}]$ is a L-H reaction rate constant.

From Equation 2.4 follows, that there is a linear reciprocal relation between the reaction rate r and reactant concentration $[A]$. In this connection, kinetics of photocatalytic reactions are frequently discussed by means of the L-H mechanism, when linearity of

the plot r^{-1} *versus* $[\mathrm{A}]^{-1}$ is observed. Nevertheless, routine experiments reveal several deficiencies of the L-H formalism [12, 154]. Particularly, it has been demonstrated that the apparent adsorption constant K' is not the same as the adsorption equilibrium constant K, measured in the dark, and depends on the intensity of the incident light [12, 143]. These discrepancies can be related to a misconception of the term "active site". This term was originally transfered from the L-H mechanism of ordinary heterogeneous catalysis and corresponded to an amount of the catalyst surface sites, where chemical reaction between two adsorbed reactants should take place. In photocatalysis, reaction proceeds between adsorbed reactant and short-living h^+_{VB} or e^-_{CB}, whose amounts strongly depend on incident light intensity, efficiency of trapping and rate of mutual recombination [12].

Since dependence of e^-_{CB}-h^+_{VB} pairs concentration on the incident light intensity is not reflected in the L-H model, the L-H rate equation has been modified. For this reason, the reaction of oxidation (11) has been considered as a second-order reaction between the reactant A and ·OH with the rate given by Equation 2.6 and pseudo-steady-state approach for the mass balance has been used (Equation 2.5) [143, 155]. The overall ·OH concentration [·OH] can be expressed by a light intensity term αI (Equation 2.6) and the reaction rate is thus given by Equation 2.7:

$$\frac{d\theta}{dt} = k_1[\mathrm{A}](1-\theta) - k_{-1}\theta - k_2[\cdot\mathrm{OH}]\theta = 0 \tag{2.5}$$

$$k_{app.} = k_2[\cdot\mathrm{OH}] = k_2\alpha I \tag{2.6}$$

$$r = -k_2[\cdot\mathrm{OH}] \cdot \frac{\frac{k_1}{k_{-1}+k_2\alpha I} \cdot [\mathrm{A}]}{1 + \frac{k_1}{k_{-1}+k_2\alpha I} \cdot [\mathrm{A}]} \tag{2.7}$$

The pseudo-steady-state L-H rate equation (Equation 2.7) reproduces a dependence of the L-H parameters K' and $k_{\text{L-H}}$ on the light intensity term αI, if the term αI is high, and transforms to the ordinary L-H equation (Equation 2.4), if the term αI is low.

A kinetic model that has taken into account most of the mechanistic aspects related to the photocatalytic surface oxidation is the direct-indirect (D-I) model [156]. In the D-I model, the processes of generation, recombination and trapping of e^-_{CB}-h^+_{VB} pairs are thoroughly considered in view of the pseudo steady-state L-H model (Equation 2.7) [156]. Moreover, the D-I model in its present state takes into account the case of "back reaction", i.e. reduction of oxidized reactants by e^-_{CB}, and the case of non-specific adsorption [154].

The present-day kinetic models provide a theoretical basis for kinetics of e^-_{CB}- and h^+_{VB}-mediated reactions at the photocatalyst surface, but unfortunately ignore the ROS chemistry, thereby disclaiming experimentally observed solution-phase oxidation by $\cdot OH_{free}$ [14]. This is possibly related to the fact, that there is still no consensus on the ROS roles in the e^-_{CB}- and h^+_{CB}-mediated reactions and their impact on $\cdot$OH generation. Nevertheless, an improved understanding of these aspects is one of the key milestones towards achieving the ultimate goal of photocatalytic research: design of truly efficient photocatalysts with tailored properties.

2.3 Photochemistry of Natural Organic Matter (NOM)

The rest amounts of BPs released with wastewater effluents into surface waters are normally exposed to natural sunlight. However, a large fraction of UV and visible light in the photic zone is absorbed by NOM [16]. On the other hand, NOM can act as a photosensitizer accelerating the BPs photolysis. NOM-sensitized photolysis is a process of natural decontamination, which importance is frequently underestimated [19]. The knowledge on BPs photolytic degradation in presence of NOM is currently scarce. Because of potentials of persistence and hazardous effects of BPs and their products, understanding of the NOM role in the photolytic transformations of BPs is an issue of high importance. Therefore, in this chapter, the key aspects of NOM photochemistry are overviewed.

NOM is an organic material formed by decay and transformation of plant and microbial remains [16]. In other words, NOM is a left over biological material, which is accumulated in enormous quantities due to its poor biodegradability [16]. An estimated amount of NOM in the aquatic environment is 700 Gt, which exceeds the total biosphere carbon amount of 573 Gt [157]. Humic substances (HS), e.g. humic acids and fulvic acids, are the principal components of the soluble part of NOM.

Due to the strong UV-vis absorption, NOM plays a very important role in natural photochemical processes, particularly, it acts as sensitizer in micropollutants photolysis [17, 19, 158–160]. Even though NOM consists of molecularly heterogeneous HS, whose complex structure may strongly vary depending on the origin, there are several key spectral features, which can be well understood by means of modern spectroscopic methods. In this concern, the following section deals with the molecular electronic excitation, as a fundamental issue in molecular spectroscopy.

2.3.1 Molecular Electronic Excitation

Efficiency of photochemical reactions is controlled by the intensity of light absorption. If the electronic structure of a molecule is known, the photon absorption probability can be calculated by the use of the Fermi's golden rule:

$$P \propto E_0^2 |\mu_{if}^2| \tag{2.8}$$

where E_0 is the photon energy; $\mu_{if} = \langle \Psi_f | \mu | \Psi_i \rangle$ is the transition dipole moment of the molecule.

The transition dipole moment μ_{if} corresponds here to an electrical dipole of transition

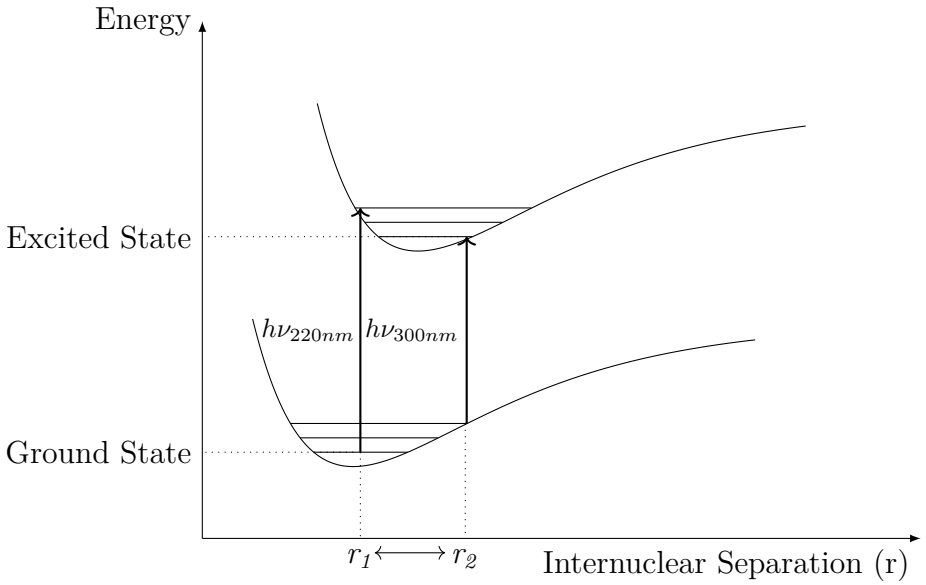

Figure 2.6: Illustration of the Franck-Condon principle in H_2O_2 photolysis.

between initial state i and final state f of the molecule. By analogy with a classical dipole, the transitional dipole moment reflects the fact that there is an interaction of the electric field of the light wave with the electric field of the molecule. The transition dipole moment depends on the electron distribution and the geometry of the molecule:

$$\langle \Psi_f | \mu | \Psi_i \rangle = \langle \psi_f | \mu | \psi_i \rangle \cdot \langle \zeta_f | \zeta_i \rangle \cdot \langle \varkappa_f | \varkappa_i \rangle \tag{2.9}$$

where $\langle \psi_f | \mu | \psi_i \rangle$ is a term of the electronic transition moment; $\langle \zeta_f | \zeta_i \rangle$ is a spin overlap integral and $\langle \varkappa_f | \varkappa_i \rangle$ is a nuclei overlap integral.

The transition dipole moment μ_{if} as well as the probability of the photon absorption P become zero, if one of the terms of Equation 2.9 is zero. Therefore, by examining properties of each term in Equation 2.9, one can obtain quantum selection rules for electronic transitions induced by the photon absorption. The electronic transition term $\langle \psi_f | \mu | \psi_i \rangle$ depends on the nature of electronic distribution in the molecule and can be estimated by examining the symmetry of the spatial wavefunctions ψ_f, ψ_i [10]. The spin term $\langle \zeta_f | \zeta_i \rangle$ contains spin wavefunctions ζ_f and ζ_i, which are orthogonal, i.e. the spin term becomes zero if the transition changes the spin configuration.

According to the Franck-Condon principle, nuclei, which are much more massive than electrons, remain frozen at equilibrium during electronic transitions. Therefore, the electronic transitions, which do not require the change in the molecule geometry via nuclei motion, are most probable, so the nuclear overlap integral $\langle \varkappa_f | \varkappa_i \rangle$ has a largest value. As

an example, consider UVA photolysis of H_2O_2, which proceeds very slowly in spite of the fact that even the energy of visible light photons exceeds the HO−OH bond energy [161]. This is due to the different geometry of H_2O_2 molecule in the ground and excited states [162]. Figure 2.6 shows that the HO−OH bond needs to be stretched in order to reach a vertical transition of UVA photon energy. This means that the transition is unlikely under normal conditions and only a very small fraction of photons can be absorbed.

Changes in molecular geometry because of vibrational and rotational motion lead to a split of each electronic level into vibrational and rotational levels, so their broad spectral bands are observed. Furthermore, the quantum selection rules represent an ideal case with some relatively simple formulations and are not always followed in reality. For example, one may observe "forbidden" according to Equation 2.9 singlet-triplet transitions in molecules with highly charged nuclei, if a spin-orbit coupling occurs. Nevertheless, the quantum selection rules work well for organic compounds composed of relatively light atoms representing a powerful tool for interpretation of molecular spectra as well as experimental data in photochemistry [10].

2.3.2 Spectral Properties of NOM

NOM has a characteristic brown color caused by an overlap of the absorption bands of multiple chromophores. The NOM chromophores are supposed to be conjugated ketonic, carboxyl, and quinone-like groups [16]. A typical NOM UV-vis absorption spectrum displays exponentially decreasing absorbance without distinct characteristic absorption bands [163]. The overall slope of log-linearized NOM absorbance can vary with pH due to the change of dissociation degree of phenolic and carboxyl groups [16].

Comparison of the spectra of terrestrial sunlight with the typical NOM UV-vis absorption spectrum reveals that NOM (at its environmentally occurring level with ρ(DOC) between 2 and 30 mg L^{-1}) can absorb essential fraction of UV-vis light (Figure 2.7). Strong UV-vis absorption is typical for the structures with conjugated double bonds, e.g. −C=C− and −C=O. Results of ^{13}C-NMR measurements of different NOM samples show that the absorbance at $\lambda = 254$ nm is mainly due to high content of aromatic carbon [16]. The NOM fluorescence excitation maximum at λ_{ex} in the range between 320 and 380 nm is also typical for highly conjugated structures [16]. All these data indicate high content of delocalized electrons and suggest high probability of the π-π^* and π^*-n electronic transitions.

In spite of the strong UV absorbance of NOM, the fluorescence quantum efficiency of NOM is low (1-5%) and is strongly dependent on the chemical environment. This is

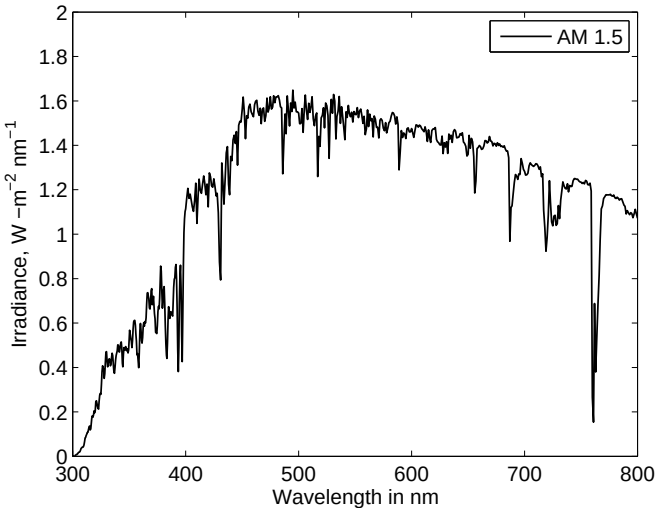

(a)

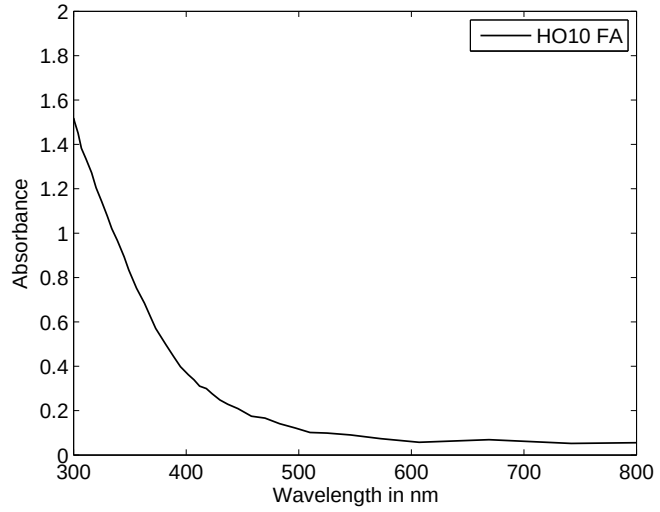

(b)

Figure 2.7: UV-vis part of the spectrum of terrestrial solar irradiance (a) and absorbance of HO10 FA solution (b) (ρ(HO10 FA) = 0.00987 g L^{-1}, path length – 5 cm, chosen according to [164]) [16].

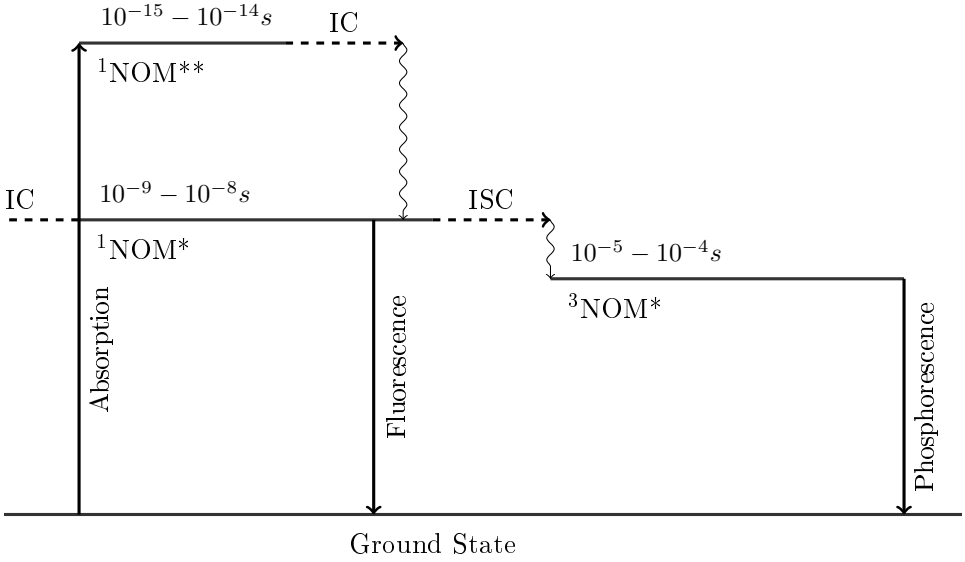

Figure 2.8: Jablonski diagram of excited NOM transients.

attributed to the efficient non-radiative relaxation of NOM molecules in the excited state [16]. The NOM Stokes shift is usually relatively large ($\Delta\lambda \approx 100$ nm), so predominance of the relaxation via internal conversion (IC) and inter-system crossing (ISC) can be deduced. Although ISC is a low-probability transition, because it leads to the change in the spin configuration (Figure 2.8), the average lifetime of the resulting triplet-state NOM transients (^{3}NOM*) can be of the order of 10^{-5} s and 10^{-4} s [165]. The lifetimes of NOM fluorescence lie in the broad range between 1 and 50 ns. Analysis of the characteristic times of NOM electronic transitions, summarized in a Jablonski diagram (Figure 2.8) shows that the generation of sufficient amounts of the ^{3}NOM* transients can be expected.

In aqueous solution, the ^{3}NOM* transients rapidly undergo relaxation via quenching by dissolved O_2. In the ground triplet state, the highest occupied molecular orbital of O_2 has two unpaired electrons with parallel spins, so the energy excess obtained from triplet NOM transients can be utilized for singlet oxygen ($^1O_2$) generation. $^1O_2$ is a highly reactive molecule and can rapidly oxidize unsaturated organic compounds forming other ROS, e.g. $\cdot$OH, H_2O_2 and $HO_2\cdot$, as by-products. ROS have a broad impact on the carbon cycling in the aquatic environment, in particular, they facilitate degradation of aqueous micropollutants. Therefore, in following subsection, the main mechanistic aspects of NOM-photosensitized generation of ROS are considered.

2.3.3 NOM-sensitized Generation of ROS

It is well accepted that the concentrations of ROS in the natural waters are directly proportional to the sunlight intensity in a photic zone [166]. However, only a small fraction of the photons absorbed by NOM induces the photosensitized generation of ROS. While a steady-state concentration of the $^3NOM^*$ transients is in the range between 10^{-15} and 10^{-13} M, the overall steady-state concentration of ROS can be several orders of magnitude higher (Table 2.3). Electronically excited NOM transients are the main ROS precursors, but the resulting steady-state ROS concentrations are mainly dependent on the rates of multiple radical reactions occurring between single ROS after photosensitization.

Table 2.3: Typical steady state-concentrations of ROS in the photic zone and their reactivity.

Species	Concentration, M	Quantum yield at 300 nm	Specific rate constant of reactions with phenol, $M^{-1}s^{-1}$
$^3NOM^*$	$10^{-15} - 10^{-13}$	$0.001 - 0.010$ [167]	
$^1O_2$	$10^{-15} - 10^{-12}$ [165]	$0.001 - 0.030$ [167]	2.6×10^6 [168]
$O_2^{\cdot -}$	$10^{-9} - 10^{-8}$ [157]		5.8×10^2 [169]
H_2O_2	$10^{-7} - 10^{-6}$ [157]	0.001 [167]	
e^-	10^{-17} [157]	$10^{-5} - 4 \times 10^{-3}$ [167]	2.0×10^7 [170]
$\cdot OH$	$10^{-18} - 10^{-17}$[157, 167]		8.6×10^9 [171]

The steady-state concentrations of specific ROS correlate well with their reactivity: the highly reactive ROS, such as $^1O_2$ and $\cdot OH$ are rapidly consumed, whereas $O_2^{\cdot -}$ and H_2O_2 are much more stable and can be accumulated in large quantities. Hereafter, the reactions of the NOM-sensitized ROS generation [166], are summarized with the ROS radical chain reactions, known from the ozone chemistry [172–174].

Excited $^1NOM^*$ transients are formed as a result of the photon absorption by NOM molecules in the initial ground state (12). Formed $^1NOM^*$ transients can reject an electron (13) or turn into the triplet-state transients $^3NOM^*$ via ISC (14).

$$NOM \xrightarrow{h\nu} {}^1NOM^* \tag{12}$$

$$^1NOM^* \rightleftharpoons NOM \cdot^+ + e^- \tag{13}$$

$$^1\mathrm{NOM}^* \xrightarrow{ISC} {}^3\mathrm{NOM}^* \tag{14}$$

If dissolved O_2 is present, it rapidly captures the rejected electron and forms superoxide, $O_2^{\cdot -}$. By analogy with the ROS chemistry in photocatalysis ((3)-(7)), accumulation of $O_2^{\cdot -}$ induces generation of ·OH (15). Moreover, $^3\mathrm{NOM}^*$ transients can directly interact with O_2 and generate $^1O_2$ (16).

$$\mathrm{e}^- + \mathrm{O}_2 \longrightarrow \mathrm{O}_2^{\cdot -} \xrightarrow{h\nu,\ 2\mathrm{H}^+} \cdot\mathrm{OH} \tag{15}$$

$$^3\mathrm{NOM}^* + \mathrm{O}_2 \longrightarrow \mathrm{NOM} + {}^1\mathrm{O}_2 \tag{16}$$

The overall efficiency of photosensitized generation of ROS can be drastically decreased by the processes of quenching and scavenging. The effect of quenching becomes significant in the water matrices with high content of aromatics and heterocyclic organics [167]. Quenching occurs via energy dissipation and mainly affects $^1O_2$ and $^3\mathrm{NOM}^*$ transients (17). Those pathways of ROS generation, which involve radical reactions are mainly diminished by side reactions with non-target matrix compounds (scavengers, S) (18).

$$^3\mathrm{NOM}^*/{}^1\mathrm{O}_2 \xrightarrow[-h\nu]{quencher} \mathrm{NOM}/\mathrm{O}_2 \tag{17}$$

$$\cdot\mathrm{OH} + \mathrm{S} \xrightarrow[-\mathrm{H}^+]{} \mathrm{S}\cdot + \mathrm{OH}^- \tag{18}$$

The data presented in Table 2.3 demonstrate that ·OH has the highest reactivity among all the ROS and is thus expected to be the primary oxidizing species [166]. ·OH can react with organic compounds via addition, hydrogen abstraction and electron transfer mechanisms [175]. In the case of BPA, elucidation of the reaction mechanism becomes especially important, as significantly different organic products can be formed depending on the reaction type. Particularly, the electron transfer reaction leads to formation of genotoxic quinones, whereas the reaction of ·OH-addition results in formation of non-harmful catechols [176].

Today, the data on mechanisms and kinetics of NOM-photosensitized photolysis of BPs are still scarce. Especially little is known about the intermediates and products of BPs degradation and the efficiency of ROS generation in presence of NOM. In view of ubiquitous presence and pseudo-persistence of BPs, the mechanism of NOM-sensitized

photolysis needs to be investigated in more depth. It seems to be especially important to improve the knowledge on the environmental fate of fluorine containing BPs, such as BPAF.

3 Results and Discussion

3.1 Degradation of BPA by TiO_2 Photocatalysis and UV Photolysis*

The processes of direct UV photolysis at $\lambda = 254$ nm and TiO_2 photocatalysis demonstrate high efficiency in treatment of BPA contaminated water [177–182]. Nevertheless, it has been reported that the mixture of BPA intermediates formed during photocatalytic treatment may result in even higher estrogenic activity than BPA itself [183]. Accumulation of such potentially harmful intermediates as a result of an incomplete treatment (not complete mineralization) can lead to secondary pollution of the treated water. In order to avoid this, in-depth understanding of the BPA degradation mechanism is needed. So far, three main intermediates of BPA photocatalytic degradation by TiO_2 have been reported [180, 184–192]. 4-Hydroxyacetophenone has been identified by HPLC-MS measurements using an authentic standard [193]. Two more molecular formulae have been suggested on the basis of HPLC-MS data on molecular ions and GC-MS spectral data [180, 184–187, 193, 194], but no reliable structural information has been obtained. Moreover, no attempts to identify BPA products formed by UV photolysis at $\lambda = 254$ nm were made. The overall estrogenic activities of the BPA solutions treated by UV photolysis [195] and TiO_2 photocatalysis were measured [183], but the knowledge on the degradation mechanisms still remains deficient. Recently, Kitamura et al. have pointed out, that *in vitro* and *in vivo* endocrine-disrupting activity of BPs is directly related to the molecular structure, particularly to the positions and number of hydroxyl groups in aromatic rings [196]. Therefore, acquisition of structural information on aromatic and particularly phenolic products of BPA photooxidation is crucial for the comprehensive assessment of the secondary pollution risks.

This section contains an investigation of BPA degradation by TiO_2 photocatalysis and UV photolysis at $\lambda = 254$ nm. The main focus is given to elucidation of the formation

*The main findings presented in this section have been published in *Applied Catalysis B: Environmental* by Kondrakov et al. [176]

mechanisms of aromatic products using HPLC-MS-MS and HPLC-MS-ToF methods. Further, the endocrine-disrupting activity and toxicity are evaluated on the base of literature data. The kinetics of both the processes are compared and the role of ·OH is investigated in experiments with and without tBuOH as a scavenger. Contribution of the h^+_{VB}-mediated oxidation to the overall degradation of BPA and formation of aromatic products are assessed as well. In addition, the quantum yields of BPA removal and mineralization are estimated.

3.1.1 Degradation Rates and Mineralization Efficiency

In order to understand the integral kinetics of BPA mineralization and generation of organic intermediates, evolution of organic carbon has been investigated. For this purpose, BPA and CO_2 concentrations were monitored throughout the reactions. The concentration of organic carbon contained in intermediates was calculated according to Equation 3.1.

$$c(org.\ carb.) = 15 \cdot c(\mathrm{BPA}) - c(\mathrm{CO_2}) \tag{3.1}$$

where $c(org.\ carb.)$ is the total concentration of organic intermediates in terms of moles of carbon (mol(C) L^{-1}); c(BPA) is the concentration of BPA and $c(CO_2)$ is the concentration of CO_2 recalculated to the solution volume (M). The coefficient at the term c(BPA) equals to 15, which is a number of C-atoms in a BPA molecule.

Figure 3.1 shows the carbon balance for the photolytic and photocatalytic processes. UV photolysis resulted in complete removal of BPA at 130 min of treatment, which agrees well with previous findings [195]. However, only 12% of the organic carbon were transformed into CO_2 at 240 min of the treatment. On the base of the spectral data obtained in HPLC-UV measurements, incomplete BPA mineralization can be explained by a poor UV light absorbance of the formed photolysis products. In case of TiO_2 photocatalysis, BPA was completely decomposed in 45 min and was completely mineralized in 240 min, apparently, due to the generation of a sufficient amount of highly reactive ·OH and h^+_{VB}.

Since sufficient degradation and partial mineralization of BPA have been observed in the process of UV photolysis, it was necessary to evaluate the contribution of the photolysis to BPA degradation by TiO_2 photocatalysis. In presence of TiO_2, BPA should absorb a much smaller amount of UV light, thus, the rate of its photolytic decay can be significantly

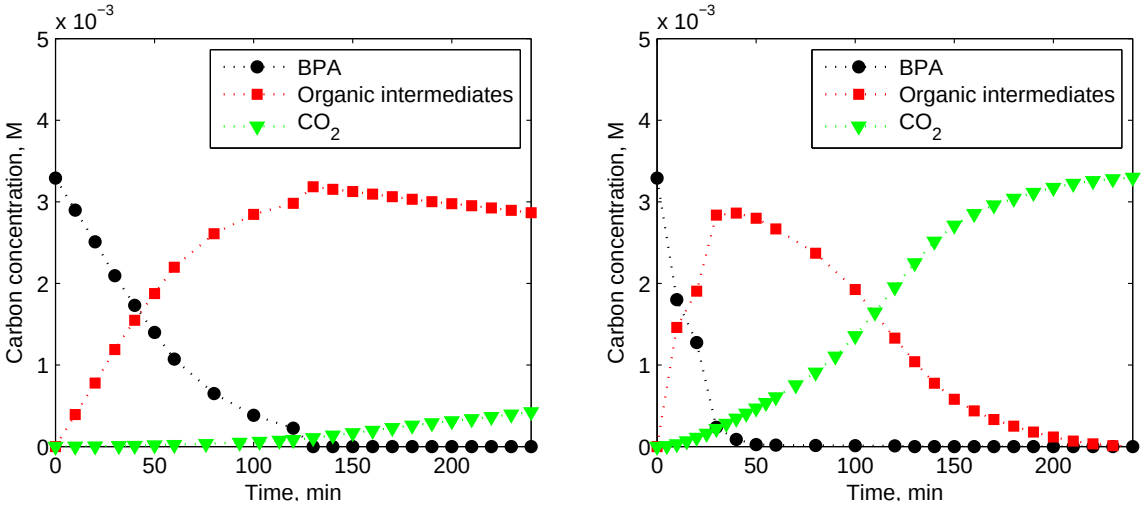

Figure 3.1: Carbon balance for BPA oxidation by UV photolysis (a) and TiO_2 photocatalysis (b) (c_0(BPA) = 0.2 mM, I_0 = 4 µE s^{-1}, ρ(TiO_2) = 0.1 g L^{-1}, pH 7, T =20 °C).

decreased. The fraction of UV irradiation absorbed by BPA in presence of TiO_2 can be evaluated by the inner filter model [197]:

$$F_{\mathrm{BPA}} = \frac{\mu(\mathrm{BPA})\rho(\mathrm{BPA})}{\mu(\mathrm{BPA})\rho(\mathrm{BPA}) + \mu(\mathrm{TiO_2})\rho(\mathrm{TiO_2})} \tag{3.2}$$

where F_{BPA} is the fraction of light absorbed by BPA; μ(BPA) and $\mu(TiO_2)$ are mass extinction coefficients of BPA and TiO_2 (g L^{-1} cm), respectively; ρ(BPA) and $\rho(TiO_2)$ are mass concentrations of BPA and TiO_2 (g L^{-1}), correspondingly. It is assumed that only BPA and TiO_2 absorbed UV light (light absorption by other compounds is neglected). For UV light at λ = 254 nm, μ(BPA)= 1.9 g L^{-1} cm (section 3.3.1) and $\mu(TiO_2)$ = 12.5 g L^{-1} cm [198]. In the photocatalytic experiments, ρ(BPA) = 0.05 g L^{-1} and $\rho(TiO_2)$ = 0.1 g L^{-1}. Under these conditions, according to Equation 3.2, BPA absorbed only 7% of UV light, and 93% were absorbed by TiO_2. Consequently, it is assumed that BPA degradation was mainly driven by photogenerated h^+_{VB} and ·OH.

Efficiencies of photolytic and photocatalytic processes have been compared on the basis of quantum yields of BPA removal and mineralization. The quantum yield (Φ) of a photochemical process is defined as the ratio of the moles of transformed molecules to the moles of absorbed photons, or alternatively:

$$\Phi = \frac{\Delta n}{\Delta t} \cdot I_{abs}^{-1} \tag{3.3}$$

Table 3.1: Quantum yields of BPA removal and mineralization.

	Φ_{removal}	$\Phi_{\text{mineralization}}$
UV photolysis	0.0039 ± 0.0004	
TiO_2 photocatalysis	0.0044 ± 0.0005	$(8.7 \pm 0.7) \times 10^{-4}$

where $\frac{\Delta n}{\Delta t}$ is the reaction rate (mol s^{-1}) and I_{abs}^{-1} is the intensity of absorbed light (E s^{-1}). Calculated values of the quantum yields show that both the processes had nearly equal efficiencies in BPA removal, but mineralization was observed in the case of TiO_2 photocatalysis only (Table 3.1).

Thus, treatment of the BPA solution by UV photolysis led to the significant accumulation of organic intermediates even at the high levels of BPA conversion.

3.1.2 Intermediates of BPA Degradation

In order to get preliminary structural information on the intermediates of BPA degradation, an HPLC-MS screening have been firstly conducted. The samples for the screening were taken at 120 min of the photolytic and at 30 min of the photocatalytic treatment. As it can be seen in Figure 3.1, these time points correspond to the highest concentrations of organic intermediates.

Table 3.2 summarizes the results of the HPLC-MS measurements. In the UV photolysis samples, the HPLC-MS screening revealed two pseudomolecular ions, $[M\text{-}H]^-$, at m/z of 243 and 167. In the samples taken in the photocatalytic process, $[M\text{-}H]^-$ ions at m/z of 243, 259, 241, 257, 245, 261 and 167 were detected. By use of the HPLC-MS-ToF method, the exact molecular masses were obtained and the elemental compositions for all the detected $[M\text{-}H]^-$ ions were calculated (Table 3.2). Further, the structures of the intermediates were chosen among possible isomers according to best matches between the estimated and experimentally measured $\log P$ coefficients (for details, see subsection 6.2.5). For short, the intermediates are numbered from **1** to **7**. The MS-MS spectra are given in subsection A.1.7.

Structures of all the intermediates identified are depicted in Figure 3.2. Intermediate **1** with a $[M\text{-}H]^-$ ion at m/z of 243 has been identified as BPA catechol, which is known as a primary product of BPA oxidation by TiO_2 photocatalysis [177, 186, 188]. The ion at m/z of 259 has been identified as a $[M\text{-}H]^-$ ion of BPA dicatechol (intermediate **2**). Previously, it had been detected in BPA solution treated by TiO_2 photocatalysis coupled with high-frequency sonolysis [188]. The elemental composition of $[M\text{-}H]^-$ ions at m/z

Table 3.2: HPLC-MS and $\log P$ data of the intermediates detected in BPA solutions treated by UV photolysis and TiO_2 photocatalysis.

Structure No.	$[M\text{-}H]^-$, m/z	Formula	MS fragments, m/z	$\log P$		Process		Previous reports
				exp.	calc.	UV	TiO_2	
1	243.1026	$C_{15}H_{16}O_3$	228, 149, 167, 124	2.9±0.1	2.8±0.2	+	+	[177, 186, 188]
2	259.0975	$C_{15}H_{16}O_4$	244, 228, 109	2.5±0.1	2.2±0.3	-	+	[188]
3	241.0870	$C_{15}H_{14}O_3$	226, 211, 198, 185, 171, 133, 121, 107, 93	3.2±0.1	2.5±0.4	-	+	No
4	257.0819	$C_{15}H_{14}O_4$	242, 227, 214, 201, 189	2.7±0.1	1.0±0.6	-	+	No
5	245.0819	$C_{14}H_{14}O_4$	227, 209, 109	1.4±0.1	1.9±0.2	-	+	No
6	261.0768	$C_{14}H_{14}O_5$	243, 149	0.9±0.1	1.3±0.3	-	+	No
7	167.0713	$C_9H_{12}O_3$	149, 134, 124, 121	0.6±0.1	0.4±0.4	+	+	No

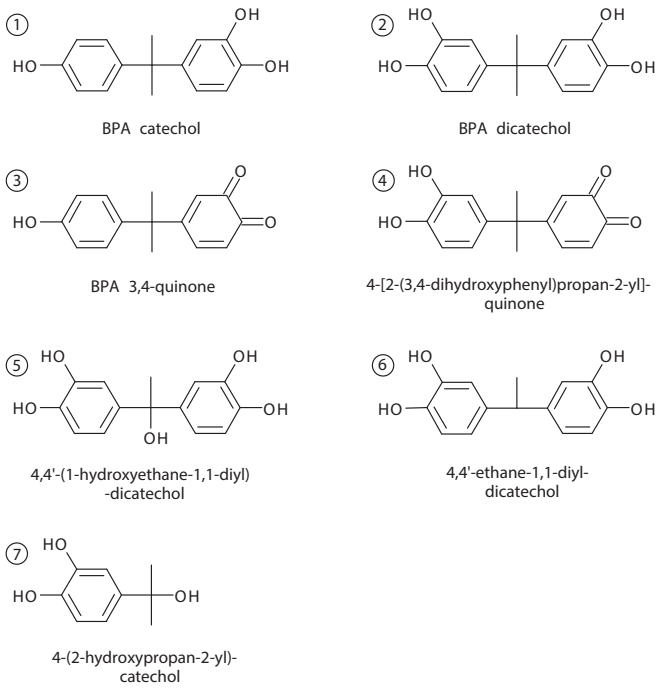

Figure 3.2: Intermediates formed during TiO_2 photocatalysis (**1**-**7**) and UV photolysis (**1** and **7**).

of 241 and 257 suggested them to be quinone derivatives of BPA and BPA dicatechol (intermediates **3** and **4**, respectively). $[M\text{-}H]^-$ ions at m/z at of 261, 245 and 167 have been attributed to 4,4'-(1-hydroxyethane-1,1-diyl)dicatechol, 4,4'-ethane-1,1-diyldicatechol and 4-(2-hydroxypropan-2-yl)catechol (intermediates **5**, **6** and **7**, respectively).

Remarkably, intermediates **1** and **7** were detected in both the photolytic and the photocatalytic processes. This observation is discussed in subsection 3.1.5.

3.1.3 Hazard Assessment of the Newly Identified Intermediates

Column 9 of Table 3.2 summarizes available literature data on the occurrence of intermediates **1**-**7** in the processes of BPA degradation by UV photolysis and TiO_2 photocatalysis. There was no reports found, which describe formation of intermediates **3**, **4**, **5**, **6** and **7** in these reactions. Moreover, Figure 3.3 with a comparison of total ion current chromatograms (TIC) and extracted ion current chromatograms (XIC) obtained by the HPLC-MS screening shows that $[M\text{-}H]^-$ ions at m/z of 241 and 257 corresponding to the quinone-like intermediates **3** and **4** occurred in the photocatalysis samples only. Therefore, the literature was analyzed in order to estimate the harmfulness of the newly found intermediates.

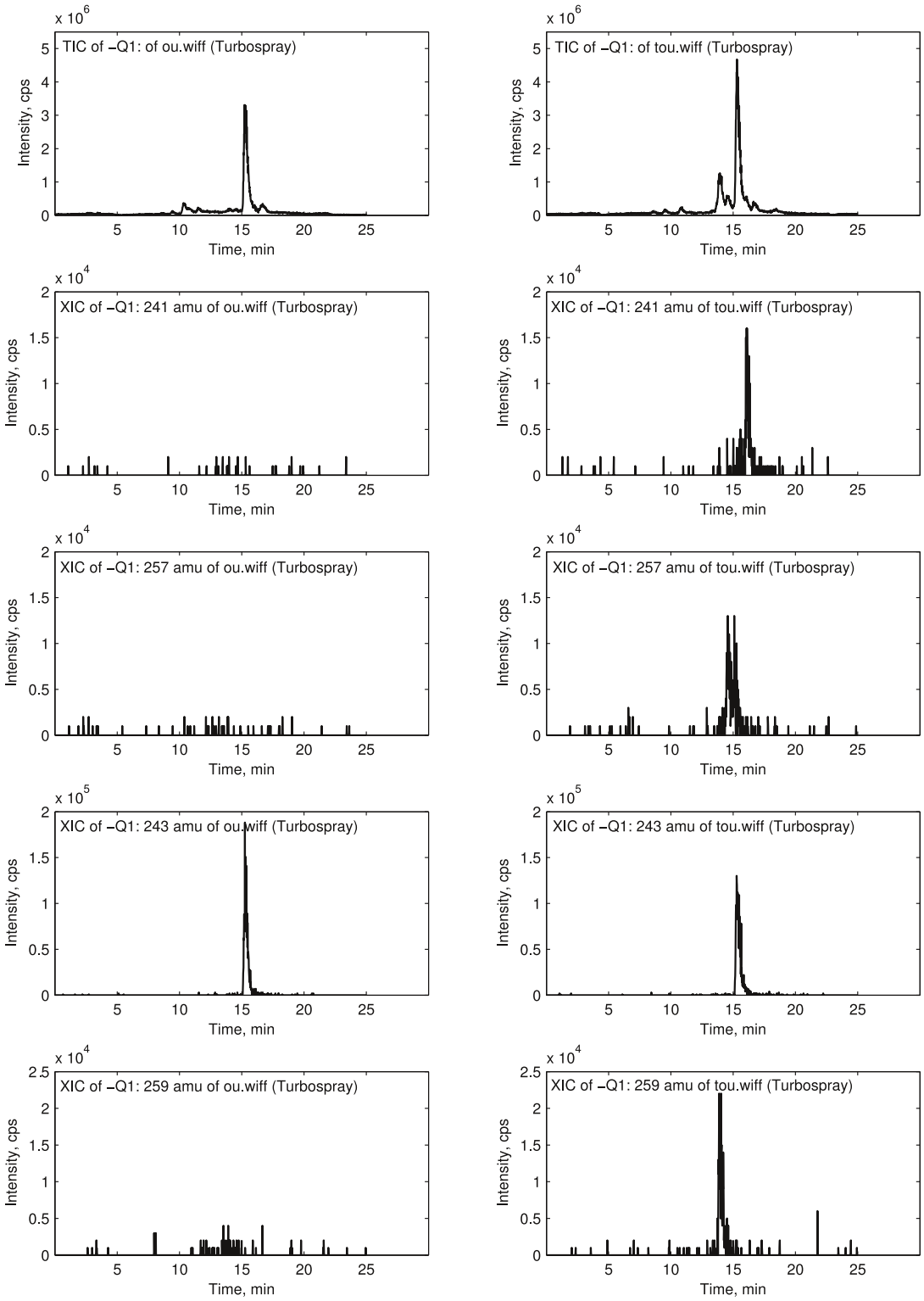

Figure 3.3: TIC and XIC data obtained for BPA solution treated by direct UV photolysis at $\lambda = 254$ nm (left) and TiO_2 photocatalysis (right) during 40 min.

It was found that 3,4-quinone of BPA (intermediate **3**), formed only in TiO_2 photocatalysis, acts as DNA binding agent [29, 199, 200]. It has been previously shown, that metabolic activation of BPA can result in formation of DNA adducts in rat prostate cells, rat liver and mice mammary tissue [199, 201, 202]. Formation of these adducts were related to the covalent modifications in DNA induced by BPA 3,4-quinone [199]. Unfortunately, no information on the hydroxylated derivative of 3,4-quinone of BPA (intermediate **4**) was found. Direct UV photolysis at $\lambda = 254$ nm has been reported to reduce the overall estrogenic activity of a BPA solution [195]. We detected only two products of BPA photolytic degradation, which may be estrogenically active due to their phenolic structures [196]. They were BPA catechol (intermediate **1**) and 4-(2-hydroxypropan-2-yl)-catechol (intermediate **7**). BPA catechol is known to be a compound with a weak MCF-7 cell estrogenic activity, which is approximately three times lower, than the one of BPA [203]. Thus, the estrogenic activity of intermediate **7** was concluded to be lower, compared to BPA, as well.

All the intermediates, which had hindered hydroxyl groups on an aromatic ring (intermediates **2** and **6**) or a hydroxylated propane group (intermediates **5** and **7**), were supposed to be less estrogenically active than BPA. This assumption was based on the data on the estrogenic activity of BPA-related compounds in ovariectomized mice and MCF-7 cells obtained by Kitamura et al. [196]. They figured out, that a phenolic hydroxyl group and a propane bridge group are essential for interactions with a binding pocket of the estrogen receptor. In particular, they showed that incorporation of these groups in the aromatic ring decreases the estrogenic activity [196].

Summing up, we suggest that catechol derivatives of BPA (intermediates **1** and **7**), formed during direct UV photolysis, should not increase the estrogenic activity of the initial BPA solution [195, 196]. However, the quinone derivatives of BPA (intermediates **3** and **4**) are potentially genotoxic [29, 199, 200] and their formation in the photocatalytic process should be thoroughly monitored.

3.1.4 Role of Free OH Radicals in BPA Degradation

Mineralization of BPA occurred in both processes of TiO_2 photocatalysis and UV photolysis. This observation could be explained by formation of $\cdot OH_{free}$ and h^+_{VB}. Therefore, degradation experiments were carried out in presence of tBuOH as radical scavenger [43]. tBuOH does not absorb 254 nm UV light, but can efficiently deactivate $\cdot OH_{free}$ in bulk solution and by this can inhibit the $\cdot OH_{free}$-driven oxidation of BPA.

The obtained results show that tBuOH retarded photolytic and photocatalytic degra-

Table 3.3: Effect of tBuOH on the rates of BPA removal by UV photolysis and TiO_2 photocatalysis.

Process	c(tBuOH), M	Rate constant, min^{-1}	R^2
UV photolysis	0	0.0186	0.9860
	0.054	0.0144	0.9979
TiO_2 photocatalysis	0	0.0973	0.9698
	0.054	0.0254	0.9988

dation of BPA suggesting an important role of $\cdot OH_{free}$ in both the processes. The reaction kinetics were fitted by first-order kinetics. The corresponding experimental rate constants of BPA disappearance are given in Table 3.3. We assumed that $\cdot OH_{free}$ were completely scavenged in presence of tBuOH at the concentration of 0.054 M and consequently used the inhibition effect for their quantification. For the UV photolysis, the concentration of $\cdot OH_{free}$ was calculated as follows:

$$c(\cdot OH) = \frac{k - k_{tBuOH}}{k_{BPA-\cdot OH}} \tag{3.4}$$

where $c(\cdot OH)$ is the concentration of $\cdot OH_{free}$ (M); k and k_{tBuOH} are the pseudo-first-order rate constants of BPA disappearance in absence and presence of tBuOH, respectively (min^{-1}) and $k_{BPA-\cdot OH}$ is the second-order rate constant for the reaction of BPA with $\cdot OH$ (M^{-1} min^{-1}). According to Equation 3.4, the concentration of $\cdot OH_{free}$ generated during UV photolysis was $c(\cdot OH) = 7{\times}10^{-15}$ M.

In the photocatalytic process, two types of $\cdot OH$ may exist; these are surface-bound $\cdot OH$, $\cdot OH_{surf}$, generated out of adsorbed water by photogenerated h^+_{VB} and $\cdot OH_{free}$ in bulk solution. Indeed, $\cdot OH_{surf}$ are chemically indistinguishable from h^+_{VB} [12], so we used the term "h^+_{VB}" for both. tBuOH adsorption on TiO_2 is rather low [204], therefore it scavenges mainly $\cdot OH_{free}$. More rigorously, competition of tBuOH and BPA for h^+_{VB} can be evaluated by means of the L-H model [204]:

$$F_{surf} = \frac{k_{tBuOH-h^+_{VB}} K_{tBuOH}\ c(tBuOH)}{k_{tBuOH-h^+_{VB}} K_{tBuOH}\ c(tBuOH) + k_{BPA-h^+_{VB}} K_{BPA} c(BPA)} \tag{3.5}$$

where F_{surf} is the fraction of h^+_{VB}, reacting with tBuOH; $k_{tBuOH-h^+_{VB}}$ and $k_{BPA-h^+_{VB}}$ are the second-order rate constants for the reactions of h^+_{VB} with tBuOH and BPA (M^{-1} s^{-1});

K_{tBuOH} and K_{BPA} are Langmuir constants of tBuOH and BPA adsorption on TiO_2 surface (M^{-1}); c(tBuOH) and c(BPA) are the concentrations of tBuOH and BPA in bulk solution (M).

We assume that the reactions of BPA and tBuOH with h^+_{VB} proceeded with the same rate constants as for the reactions of BPA and tBuOH with $\cdot OH_{free}$. Substitution of the values $k_{\mathrm{tBuOH}-h^+_{VB}}$=5.0×10^8 M^{-1} s^{-1} [201], $k_{\mathrm{BPA}-h^+_{VB}}$=6.0×10^9 M^{-1} s^{-1} [202], K_{tBuOH} = 17 M^{-1} [204], K_{BPA} = 3.7×10^5 M^{-1} [205], c(tBuOH) = 0.054 M and c(BPA) = 2×10^{-4} M in Equation 3.5 results in $F_{surf} = 10^{-3}$. Therefore, only 0.1% of h^+_{VB} were scavenged by tBuOH in the photocatalysis experiment. Thus, we also applied Equation 3.4 to quantify $\cdot OH_{free}$ formed in the TiO_2 suspension and obtained $c(\cdot OH) = 1.2\times10^{-13}$ M. Further, the concentration of h^+_{VB}, $c(h^+_{VB})$, was calculated as follows:

$$c(h^+_{VB}) = \frac{k_{\mathrm{tBuOH}}}{k_{\mathrm{BPA}-\cdot OH}} \tag{3.6}$$

Calculation according to Equation 3.6 resulted in $c(h^+_{VB}) = 1.36\times10^{-14}$ M. This value corresponds to 10% of the total concentration of h^+_{VB} and $\cdot OH_{free}$ together and agrees well with the moderate BPA adsorption capacity of P25 as reported elsewhere [205]. Concentration of the reactive oxidants, e.g. $\cdot OH_{free}$ and h^+_{VB}, generated in the photocatalytic process, were almost two orders of magnitude higher than in case of photolysis. These results explained the enhanced efficiency of photocatalytic mineralization. Nevertheless, the amounts of $\cdot OH_{free}$ generated during UV photolysis contributed to the BPA degradation rate by 23% (Table 3.3) and apparently provided partial mineralization Figure 3.1.

3.1.5 Mechanisms of BPA Degradation

The mechanism of BPA degradation was elucidated by monitoring of the formation kinetics of the major intermediates **1**, **2**, **3** and **7** in both the processes. Special attention was given to the formation of potentially genotoxic 3,4-quinone of BPA (intermediate **3**), which was observed in the photocatalytic process. Since no standards of the products identified were available, time courses of their HPLC-UV peak areas were analyzed. They are depicted in Figure 3.4 and Figure 3.5 covering the first 60 min of the degradation process. In the experiments with the scavenger, the complete deactivation of $\cdot OH_{free}$ during this time was ensured by the use of a relatively high initial concentration of tBuOH (c_0(tBuOH) = 0.054 M). Formation of intermediates **1** and **7** during UV photolysis was rather slightly affected by tBuOH at the initial stages (Figure 3.4). It indicates that their

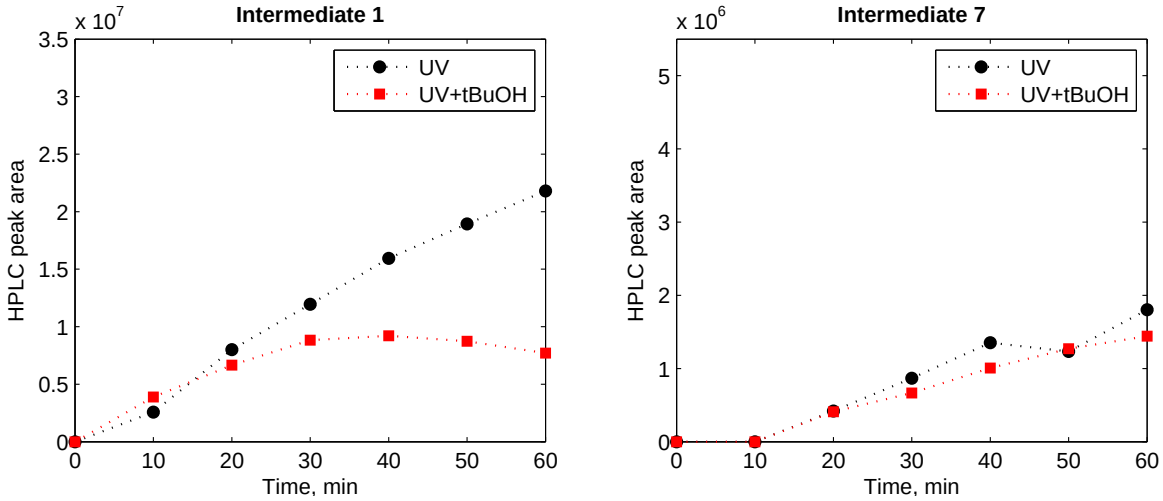

Figure 3.4: Kinetic profiles of the primary intermediates formed during direct UV photolysis of BPA. c(BPA) = 0.2 mM, c_0(tBuOH) = 54 mM, I_0 = 4 µE s^{-1}, pH 7, T = 25 °C.

generation was driven by direct photolytic cleavage of a BPA molecule with subsequent oxidation by dissolved O_2.

In case of TiO_2 photocatalysis, the influence of direct UV photolysis was negligible (see subsection 3.1.1), and both $\cdot OH_{free}$ and h^+_{VB} were therefore the main oxidizing species. The kinetic profiles shown in Figure 3.5 illustrate that catechol and quinone intermediates were formed, even when $\cdot OH_{free}$ were completely suppressed. This evidences that catechol and quinone were mainly produced via the h^+_{VB}-mediated oxidation. Moreover, scavenging of $\cdot OH_{free}$ led to a blockage of BPA dicatechol formation, but favored generation of BPA 3,4-quinone. Evidently, BPA catechol was a precursor of BPA quinones [203], and a competition between h^+_{VB} and $\cdot OH_{free}$ for the catechol oxidation could be observed. It is reasonable to assume that h^+_{VB} were responsible for the transformation of BPA catechol into BPA quinone, while $\cdot OH_{free}$ turned BPA catechol to BPA dicatechol by hydroxylation.

Finally, the mechanisms of BPA degradation by UV photolysis (Figure 3.6) and TiO_2 photocatalysis (Figure 3.7) were compiled. UV photolysis resulted in the rapid formation of BPA catechol (intermediate **1**) and 4-(2-hydroxypropan-2-yl)-catechol (intermediate **7**) that have lower estrogenic-disrupting activity comparing to BPA [195, 196]. $\cdot OH_{free}$, detected by tBuOH probing, provided partial mineralization of organic carbon. It should be noted that TiO_2 photocatalysis also led to generation of intermediates **1** and **7**. This observation could be explained in terms of similar mechanisms of oxidation of phenolic compounds by $\cdot OH_{free}$ and UV light. Obviously, $\cdot OH_{free}$ attacked an electron-rich aromatic

ring of a BPA molecule forming a cyclohexadienyl radical [175]. On the other hand, if absorption of a photon takes place, it results in the formation of a phenoxy radical of BPA [206]. Hence, in presence of O_2 both cyclohexadienyl and phenoxy BPA radicals can be further hydroxylated to intermediates **1** and **7**.

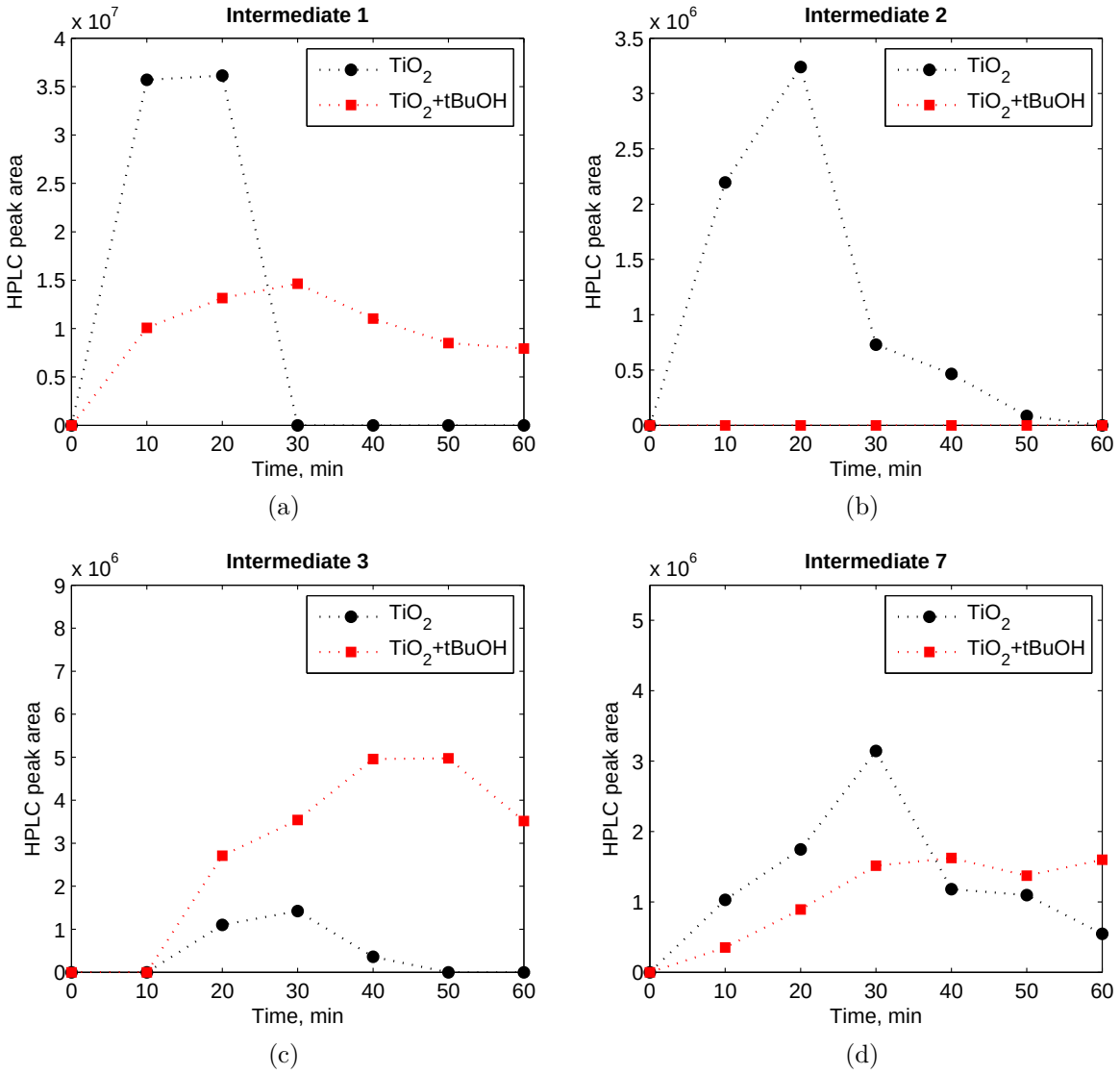

Figure 3.5: Kinetic profiles of major intermediates formed during photocatalytic degradation. c(BPA) = 0.2 mM, c_0(tBuOH) = 54 mM, I_0 = 4 µE s^{-1}, $\rho(TiO_2)$ = 0.1 g L^{-1}, pH 7, T = 25 °C.

Oxidation of BPA by TiO_2 photocatalysis was driven by h^+_{VB} and $\cdot OH_{free}$ and resulted in the formation of seven intermediates. Scavenging of $\cdot OH_{free}$ caused a mechanism change and intensified the formation of potentially genotoxic 3,4-quinone of BPA. Intermediate **7** was the most stable aromatic compound formed in the photolytic and photocatalytic

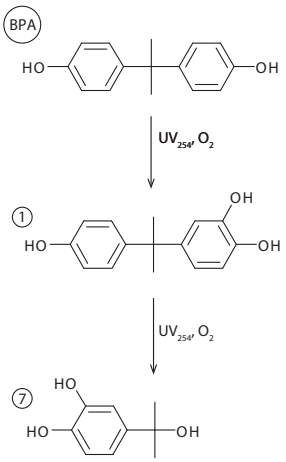

Figure 3.6: Mechanism of BPA degradation by UV photolysis.

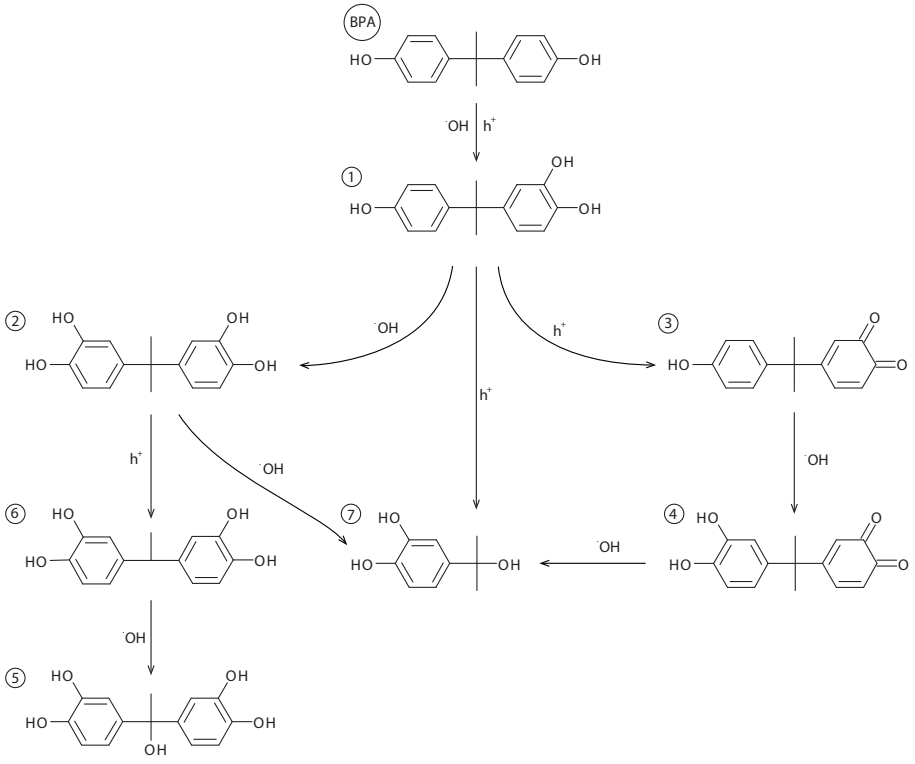

Figure 3.7: Mechanism of BPA degradation by TiO_2 photocatalysis.

treatment. However, it was not detected after 120 min of the TiO_2 photocatalytic treatment and not after 240 min of UV photolysis. During this time period, all the aromatic intermediates were degraded, and the pH dropped. Products formed afterwards, were assumed to be non-aromatic acids with low potential of estrogenic activity.

3.1.6 Interim Summary

The results of this section demonstrate a high performance of the combination of the HPLC–MSMS/ToF analysis with logP model estimations for the investigation of the intermediate products of BPA oxidation by UV photolysis at $\lambda = 254$ nm and TiO_2 photocatalysis. This enhanced analytical approach provided identification of five new potentially toxic intermediates, in particular, those formed on the TiO_2 surface. Whereas an $\cdot OH_{free}$-attack and the direct UV photolysis resulted in formation of non-harmful catechols, oxidation by photogenerated h^+_{VB} led to the formation of genotoxic 3,4-quinone of BPA. Although direct UV photolyiss looked more feasible for the elimination of BPA, its complete mineralization was achieved in the photocatalytic process only.

3.2 Relative Roles of Free and Surface-Bound OH Radicals in TiO_2 Photocatalysis†

It has been well established that exposure of aqueous suspensions of TiO_2 to UV light results in generation of e^-_{CB}-h^+_{VB} pairs and ROS, such as $.O_2^-$, H_2O_2 and ·OH [135]; but there is still no consensus on their particular mobilities and formation mechanisms [15]. ·OH and h^+_{VB} possess the highest reactivity towards most of the organic compounds and, thus, can be efficiently exploited for decontamination of water [139]. Frequently, those h^+_{VB}, which are trapped at the TiO_2 surface as electron deficient titanol groups $>Ti{-}OH\cdot$, are defined as surface-bound ·OH, $\cdot OH_{surf}$. It is generally accepted that $\cdot OH_{surf}$ or h^+_{VB} react with an adsorbed contaminant via the direct electron transfer mechanism, whereas $\cdot OH_{free}$ typically participate in the ·OH-addition and hydrogen abstraction reactions in the solution bulk. Thus, relative efficiencies of $\cdot OH_{surf}$ and $\cdot OH_{free}$ generation determine a rate limiting step as well as a predominate reaction pathway of the photocatalytic process. In other words, they may define not only where – at the TiO_2 surface or in the solution bulk – but also how the photocatalytic degradation occurs and what intermediates are formed. In view of the fact that degradation of BPA via $\cdot OH_{surf}$-mediated electron transfer reaction may lead to the formation of genotoxic quinone-like products [176], distinguishing between the two ·OH types seems to be especially important.

By now, electron spin resonance (ESR) trapping have been extensively used for ·OH detection [121, 139, 208, 209]. However, interpretation of ESR data remains a challenging task, because both $\cdot OH_{surf}$ and $\cdot OH_{free}$ may react with the spin traps identically, so unambiguous assignment of the observed ESR signals is not possible [14]. Nevertheless, data on degradation of isotopically labeled organic compounds with different adsorption affinity towards TiO_2 surfaces suggest that photocatalytic degradation occurs via a dual $\cdot OH_{surf}$/$\cdot OH_{free}$-mediated mechanism [14, 15]. As far as we know, no quantitative data on the contributions of $\cdot OH_{surf}$ and $\cdot OH_{free}$ in the overall process performance have been reported yet. The dual $\cdot OH_{surf}$/$\cdot OH_{free}$-mediated mechanism remains under debates and general understanding of the photocatalysis mechanism is not consistent [12, 13]. In this perspective, further development of the methods, aimed at investigation of the particular roles of $\cdot OH_{surf}$ and $\cdot OH_{free}$, is highly necessary.

In this section, we report on a study of sources, amounts and mobility of ·OH generated in aqueous suspension of TiO_2 irradiated by simulated solar light. We approached the

†The main findings presented in this section have been submitted to *Applied Catalysis B: Environmental* by Kondrakov et al. [207]

problem of selective quantification of $\cdot OH_{surf}$ and $\cdot OH_{free}$ by a newly developed remote photocatalysis technique with the use of isotopic labeling throughout specific reaction pathways. The developed approach is based on oxidation of a hydrophobic probe compound, 1,3,5-trichlorobenzene (TCB), adsorbed in pores of SG microparticles. Small size of the SG pores (4 nm) prevented penetration of 25 nm TiO_2 particles and ruled out the possibility of a $\cdot OH_{surf}$-mediated reaction. Due to the structural symmetry, attack of $\cdot OH_{free}$ resulted in transformation of TCB to its single degradation product - 2,4,6-trichlorophenol (TCP). We therefore expected that the degradation of TCB inside the SG pores was predominantly driven by reaction with $\cdot OH_{free}$ and used its kinetics for the determination of the quantum yield of the $\cdot OH_{free}$ production. Finally, we conducted experiments with isotopically labeled O_2 ($^{18}O_2$) and scavengers for e^-_{CB} and h^+_{VB} in order to estimate their roles in $\cdot OH_{free}$ formation.

3.2.1 Estimation of the Total Amounts of OH Radicals

Prior to determination of quantum yield of $\cdot OH_{free}$ generation, the total amounts and generation quantum yields of $\cdot OH_{surf}$ and $\cdot OH_{free}$ formed in aqueous suspension of TiO_2 under irradiation by simulated solar light were estimated. We assumed that $\cdot OH_{surf}$ and $\cdot OH_{free}$ reacted identically and denoted both the species as $\cdot OH$ for simplicity. Then, the formation kinetics of TCP in the photocatalytic degradation of TCB dissolved in the TiO_2 suspension bulk was analyzed.

The kinetic profiles of TCB and TCP in Figure 3.8 demonstrate a significant time overlap and indicate that both the degrading TCB and forming TCP competed for $\cdot OH$.

$$\mathrm{TCB} + \cdot\mathrm{OH} \longrightarrow \mathrm{TCP} \tag{1}$$

$$\mathrm{TCP} + \cdot\mathrm{OH} \longrightarrow \mathrm{Products} \tag{2}$$

Under these conditions, the rates of TCB degradation and TCP formation can be defined by Equation 3.7 and Equation 3.8, respectively:

$$[\mathrm{TCB}] = c_0(\mathrm{TCB})\mathrm{e}^{-k_1 t} \tag{3.7}$$

$$[\mathrm{TCP}] = c_0(\mathrm{TCB})\frac{k_1}{k_2 - k_1}(\mathrm{e}^{-k_1 t} - \mathrm{e}^{-k_2 t}) \tag{3.8}$$

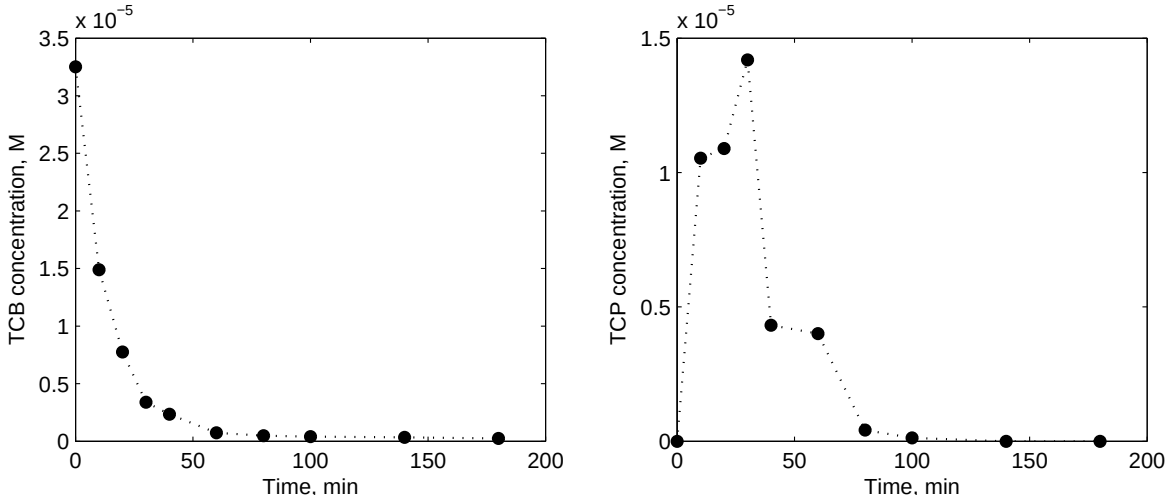

Figure 3.8: Degradation of the dissolved TCB (a) and formation of TCP (b) in an aqueous suspension of TiO_2. c_0(TCB) = 33.1 µM, $\rho(TiO_2)$ = 0.1 g L^{-1}, I_0 = 5 µE s^{-1}, pH 7, T = 25 °C.

where [TCB] and [TCP] are momentary concentrations of TCB and TCP (M), respectively; c_0(TCB) is an initial concentration of TCB (M); k_1 and k_2 are pseudo-first-order rate constants of reactions (1) and (2), respectively (s^{-1}).

The terms k_1 and k_2 can be further expressed as a ·OH steady-state concentration term $[\cdot OH]_{ss}$ multiplied by the corresponding second-order reaction rate constants:

$$k_1 = k_{\cdot\text{OH-TCB}}[\cdot OH]_{ss} \tag{3.9}$$

$$k_2 = k_{\cdot\text{OH-TCP}}[\cdot OH]_{ss} \tag{3.10}$$

where $k_{\cdot\text{OH-TCB}} = 5.0\times10^9$ M^{-1} s^{-1} (taken as equivalent to that reported for 1,2,4-TCB [210]) and $k_{\cdot\text{OH-TCP}}=1.2\times10^{10}$ M^{-1} s^{-1} (taken as equivalent to that reported for 2,4,5-TCP [211]). Thus, if we combine these equations, we obtain the $[\cdot OH]_{ss}$ values by fitting calculated TCB and TCP kinetic profiles to the experimental data as shown in Figure 3.9.

Table 3.4 shows significant differences in the calculated $[\cdot OH]_{ss}$ values. In particular, the $[\cdot OH]_{ss}$ value obtained from Equation 3.7 is essentially higher than that obtained from Equation 3.8. This difference can be attributed to the fact that Equation 3.7 considers reaction (1) between TCB and ·OH only and neglects that forming TCP competes for ·OH as well, which results in the overestimated $[\cdot OH]_{ss}$ value. Therefore, it seems to be

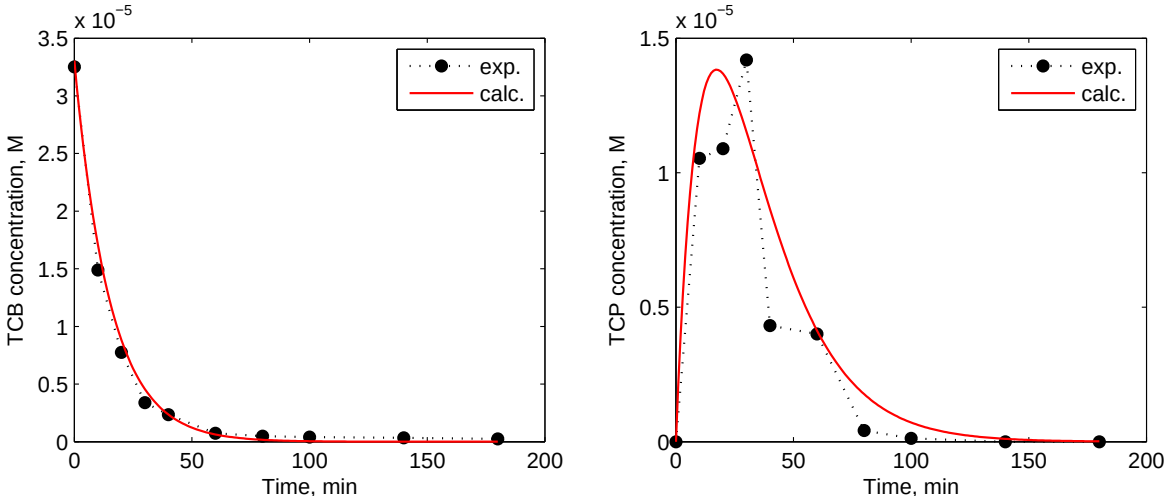

Figure 3.9: Kinetic analysis of degradation of dissolved TCB (a) and formation of TCP (b) in the aqueous suspension of TiO_2. The experimental conditions are the same as those given in Figure 3.8.

Table 3.4: Concentrations of ·OH estimated by analysis of degradation of dissolved TCB.

Process	$[\cdot OH]_{ss}$, M	Calculated acc.
TCB degradation	$2.5 \pm 0.5 \times 10^{-13}$	Equation 3.7
TCP formation	$0.8 \pm 0.3 \times 10^{-13}$	Equation 3.8

reasonable to use the value $[\cdot OH]_{ss} = 0.8 \times 10^{-13}$ M, because it takes into account both reactions (1) and (2).

The quantum yield of ·OH generation can be estimated from the kinetics of TCP formation assuming that its formation rate at the initial stage (0-20 min) is constant and that the transformation of TCB into TCP is exclusively driven by ·OH. Supposing that along the 4 cm light path used, UVA light is completely absorbed by TiO_2 ($I_{abs} = I_0 = 5$ µE s^{-1}), we can calculate the ·OH generation quantum yield (Φ) according to Equation 3.3. Thus, irradiation of aqueous TiO_2 suspension with $\rho(TiO_2) = 0.1$ g L^{-1} by simulated solar light results in generation of $\cdot OH_{surf}$ and $\cdot OH_{free}$ at the total steady-state concentration of 0.8×10^{-13} M with $\Phi = 0.042$. The obtained Φ value agrees well with the value $\Phi = 0.04$ reported previously [212].

3.2.2 Effects of Hole, Electron and OH Radical Scavengers on the Photocatalytic Performance

The experiments described in the previous subsection were aimed at the estimation of the total ·OH quantities assuming the $\cdot OH_{free}$–$\cdot OH_{surf}$ equivalence, therefore, clarification of the particular roles of $\cdot OH_{free}$ and $\cdot OH_{surf}$ required more detailed investigation. Generally, it is believed that $\cdot OH_{surf}$ can be generated via h^+_{VB}-mediated oxidation of H_2O, whereas $\cdot OH_{free}$ – via reduction of dissolved O_2 by e^-_{CB} [15, 204]. In addition, at initial stages, the photocatalytic process can be driven by direct h^+_{VB}-mediated oxidation of the organic compound [213]. Therefore, we designed experiments on the degradation of dissolved TCB in presence of selective e^-_{CB}, h^+_{VB} and $\cdot OH_{free}$ scavengers in order to get insight in their roles at different stages of the process. Here, Ag^+, HCOOH and tBuOH were chosen as commonly used scavengers for e^-_{CB}, h^+_{VB} and $\cdot OH_{free}$, respectively [204, 214].

The obtained kinetic profiles of TCB degradation and TCP formation in presence of Ag^+, HCOOH and tBuOH are shown in Figure 3.10. Interestingly, all the scavengers retarded the degradation of TCB in a quite similar way. In addition, in the experiments with the scavengers, the TCB kinetic profiles demonstrate more complex shapes compared to the blank experiment, where no scavengers were present. A distinct change in the rates of TCB degradation can be seen at ca. 40 min of the processes. During the initial time period (0-40 min), formation of TCP proceeded non-equimolarly and was apparently accompanied by an alternative oxidation pathway. Although the conventional view holds that photocatalytic oxidation of chlorobenzenes proceeds via formation of chlorohydroxycyclohexadienyl radicals, which can be further oxidized to chlorophenols and chloroquinones or dechlorinated to phenols and quinones [215], the formation of such species was not observed in our experiments. Because only a negligible amount of dichlorobenzene was detected at the end of the processes, reduction of TCB by e^-_{CB} was ruled out. In addition, rather strong adsorption of TCB on the TiO_2 surface via Cl-atoms was favored [216, 217]. Taken together, these data suggest that TCB degradation initially proceeded via $\cdot OH_{surf}$-oxidation of the pre-adsorbed TCB to polar and/or non-volatile ring opening products, which were not detectable by GC-MS analysis (Figure 3.11).

The amounts of $\cdot OH_{surf}$ responsible for the degradation of the pre-adsorbed TCB fraction can be estimated by substitution of the $[\cdot OH]_{ss}$ term in Equation 3.7 to $[\cdot OH_{surf}]_{ss}$. The value $[\cdot OH_{surf}]_{ss} = 3.0\times10^{-14}$ M is further obtained on the basis of the fitting of the equation solution to the experimental data on the TCB degradation in presence of tBuOH during the initial 40 min time period. It should be noted that poorly adsorbing

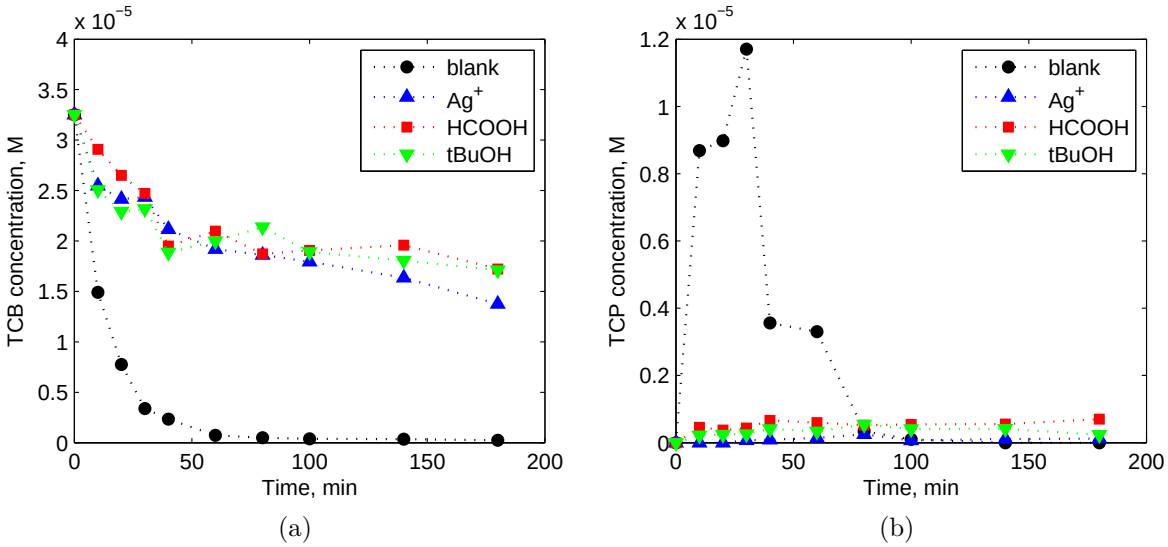

Figure 3.10: Effects of Ag^+, HCOOH and tBuOH on the degradation of dissolved TCB (a) and formation of TCP (b) in the aqueous suspension of TiO_2. c_0(TCB) = 33.1 µM, $\rho(TiO_2)$ = 0.1 g L^{-1}, $c_0(Ag^+)$ = 2 mM, c_0(HCOOH) = 45 mM, c_0(tBuOH) = 54 mM, I_0 = 5 µE s^{-1}, pH 7, T = 25 °C.

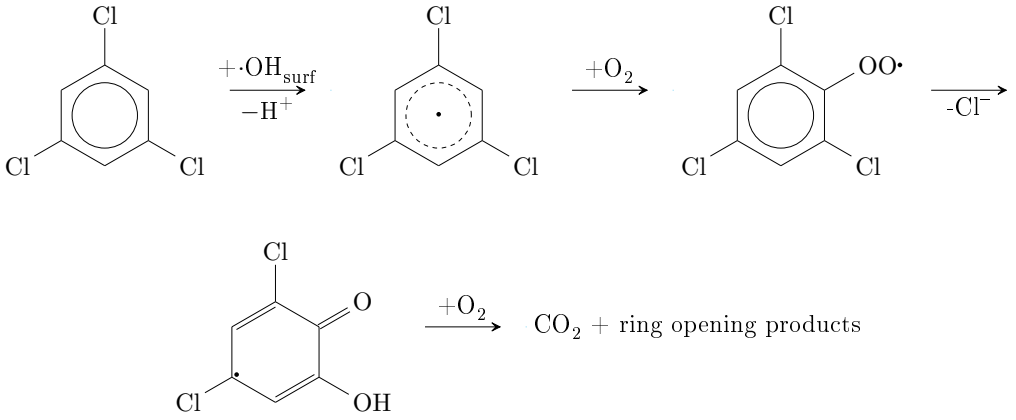

Figure 3.11: Proposed mechanism of $\cdot OH_{surf}$-mediated oxidation of TCB.

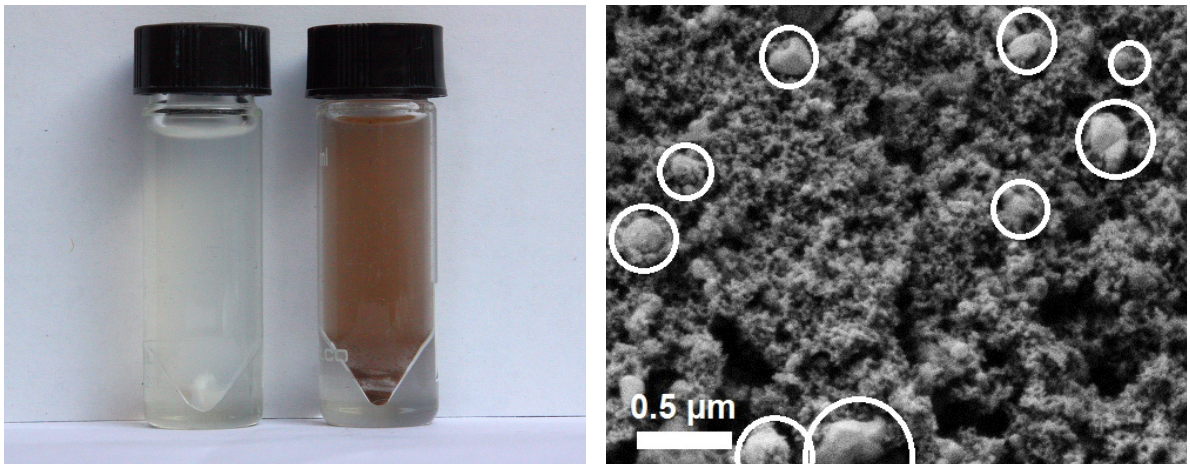

(a) (b)

Figure 3.12: Changes of the TiO_2 suspension color after 1 hr of the photocatalytic reaction in presence of 0.002 M Ag^+ (a; from left to right) and SEM micrograph illustrating Ag^0 deposition with the largest Ag-particles marked by white circles (b).

tBuOH is expected to scavenge only $\cdot OH_{free}$ in the solution but not $\cdot OH_{surf}$ at the TiO_2 surface [204].

During the time period later on, degradation of TCB was strongly suppressed when the scavengers were present. Fitting of these experimental data in the same way as described above results in $[\cdot OH]_{ss} = 3{\times}10^{-15}$ for all the three cases (Table 3.5). Whereas the decrease of $[\cdot OH]_{ss}$ caused by HCOOH and tBuOH addition can be attributed to the scavenging of $\cdot OH_{surf}$ and $\cdot OH_{free}$, respectively, the effect of Ag^+ seems to be rather dual. On the one hand, reaction of Ag^+ with e^-_{CB} is expected to suppress the production of $\cdot OH_{free}$ via e^-_{CB}-mediated reduction of dissolved O_2 on the TiO_2 surface [218]. The counterion, NO_3^-, is a poorly reacting species with $k_{.OH\text{-}NO_3^-} = 2.8{\times}10^5$ M^{-1} s^{-1} [219] and is therefore unable to compete with TCB for $\cdot OH_{free}$ or $\cdot OH_{surf}$. On the other hand, photocatalytic reduction of Ag^+ can lead to deposition of significant amounts of Ag^0 on the TiO_2 surface, which may decrease the efficiency of light absorption by TiO_2 [218]. A significant change of the TiO_2 suspension color occurred after 1 h of the process (Figure 3.12-a). Moreover, analysis of SEM micrographs reveals the formation of large Ag-particles, which could decrease the fraction of UV light available for TiO_2 (Figure 3.12-b). The pre-adsorbed TCB could act as an efficient h^+_{VB} trap suppressing the h^+_{VB}-e^-_{CB} recombination and intensifying the Ag^0 deposition. Such assumptions do not contradict the observations reported previously [218]. Therefore, a complex interaction of all these factors do not allow us to unambiguously attribute the Ag^+ retardation effect to the e^-_{CB} scavenging.

Table 3.5: Effects of scavengers on the total ·OH amounts.

Scavenger	$[\cdot OH]_{ss}$, M	$[\cdot OH_{surf}]_{ss}$, M
none	8.0×10^{-14}	
tBuOH	3×10^{-15}	$3.0\times10^{-14*}$
HCOOH	3×10^{-15}	
Ag^+	3×10^{-15}	

*estimated for the initial 40 min of the process.

It is important to note that HCOOH could also act as a non-selective scavenger reacting with $\cdot OH_{free}$ in the solution. Thus, similar $[\cdot OH]_{ss}$ values obtained for the experiments with tBuOH and HCOOH (Table 3.5) could be explained by a hypothesis that in the initial time period, pre-adsorbed TCB was primarily degraded by $\cdot OH_{surf}$ or h^+_{VB}. Subsequently, H_2O started to compete for the h^+_{VB} sites, which gave rise to $\cdot OH_{free}$ until they were scavenged by dissolved tBuOH and HCOOH in the solution. The effect of Ag^+ was predominantly accompanied by light depletion caused by Ag^0 deposition, which obstructs the clarification of a truly role of e^-_{CB}. Summing up, it seems to be possible to make tentative estimations of the effects of e^-_{CB}, h^+_{VB} and $\cdot OH_{free}$ scavengers on TCB degradation but, unfortunately, the origin and chemical form of ·OH, primarily responsible for the TCB degradation can not be figured out explicitly.

3.2.3 Adsorptive Behavior of a Model Compound in Mesopores of a Silica Gel (SG) Carrier

In the experiments on remote photocatalytic oxidation aimed at the estimation of quantum yield of $\cdot OH_{free}$ generation, highly porous (pore size = 4 nm) SG microparticles, whose pore surface was enriched by TCB, were used. In order to investigate the adsorptive behavior of TCB on the SG phase, its adsorption kinetics was monitored by the MS detector of a GC-MS system. In short, a column packed with 420 mg of SG phase was connected to a He flow carrying the TCB vapors at 1.6 mL min^{-1} flow rate on the one side and to the MS detector operating in electron ionization (EI) mode on the other side. Thus, the breakthrough and adsorbed amounts of TCB were calculated. As a result, TCB adsorption isotherms were obtained and analyzed by means of the BET method [220]. For details on the adsorption and the analysis procedure, please refer to subsection 6.3.3.

The obtained TCB adsorption isotherm and its BET plot $(n_{ads}(p/p_0-1))^{-1}$ *vs.* p/p_0 are

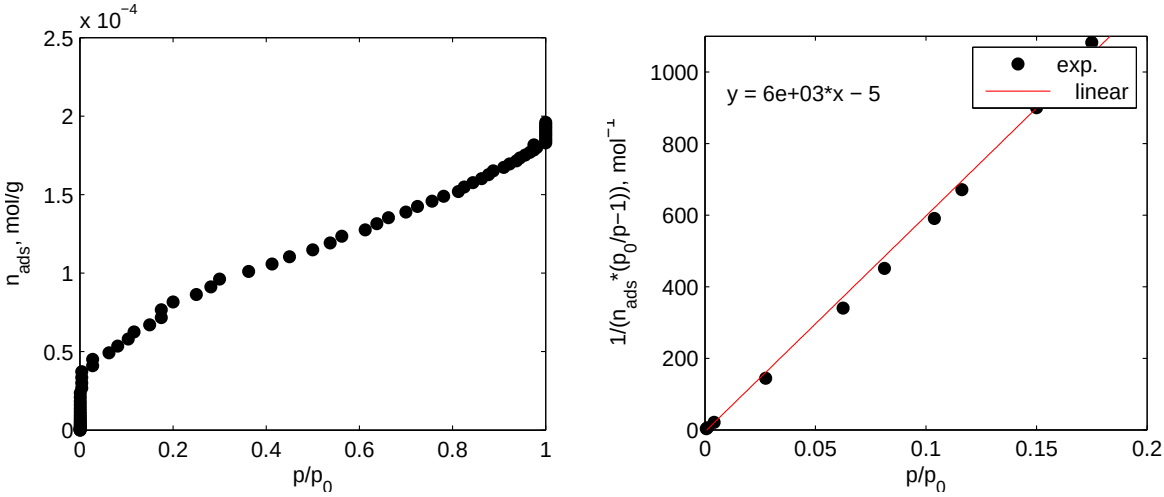

Figure 3.13: BET isotherm (a) and BET plot (b) for TCB adsorption in SG pores.

Table 3.6: Characteristics of TCB adsorption in SG pores.

Characteristics	Value
n_{max}, mol g^{-1}	1.5×10^{-4}
R^2	0.9983
TCB adsorption site area, nm^2	4.4
Area of a single TCB molecule, nm^2	1.35 ± 0.01 [222]

depicted in Figure 3.13. TCB exhibits an adsorption isotherm form, which is characteristic for the narrow slit mesoporous adsorbents [221]. The BET plot is linear in the p/p_0 range between 0.0 and 0.2, which corresponds to the formation of a TCB monolayer. By the use of previously reported data on a SG BET surface area [221] and the measured SG adsorptive capacity, the adsorption site size at the monolayer TCB coverage can be estimated. These data and the results of BET plot analysis are given in Table 3.6. The difference in the adsorption site size and the area of a single TCB molecule can be attributed to the formation of a rather moderately dense filled TCB monolayer.

Even though the isotherm analysis shows that only 40% of the TCB molecules constituted a monolayer, analysis of a supernatant of the SG aqueous dispersion revealed a negligible (0.05%) TCB migration from SG to the water phase. Thus, the major part of TCB was expected to be strongly retained in SG pores as a moderately dense packed monolayer available for the $\cdot OH_{free}$-attack.

3.2.4 Reactions of Free OH Radicals in the SG Pores

The results suggesting a dual $\cdot OH_{surf}/\cdot OH_{free}$-driven mechanism of photocatalytic degradation of TCB (subsection 3.2.2) are unfortunately rather tentative in respect to the relative roles of $\cdot OH_{surf}$ and $\cdot OH_{free}$. Therefore, we have developed a new remote photocatalysis approach to selectively investigate the relative role of $\cdot OH_{free}$ in the photocatalytic process and to estimate their amounts. As demonstrated in subsection 3.2.3, the major part of TCB could be adsorbed in the 4 nm pores of the SG phase as a moderately dense packed monolayer available for $\cdot OH_{free}$-driven oxidation. Figure 3.14 shows that a small part of TCB migrated into the aqueous phase and was oxidized there, but the amounts of the freely dissolved TCB and TCP were negligible in comparison to those retained in the SG pores. In addition, analysis of the dark and TiO_2-free control samples pointed out that there was neither TCB disappearance nor TCP formation. Therefore, we neglect the competition of the dissolved TCB and TCP fractions for $\cdot OH_{free}$ as well as losses of TCB because of a dark photocatalytic reaction or evaporation.

Figure 3.14 represents kinetic profiles of transformation of TCB into TCP, which was selectively driven by $\cdot OH_{free}$. A comparison between the kinetic profiles given in Figure 3.14 with those obtained for the TCB degradation in the solution (Figure 3.8) reveals several essential differences, which need a detailed explanation. First of all, a different stoichiometry of TCB-TCP transformation in the pores of the SG phase and in solution can be observed. In particular, degradation of TCB in the solution demonstrates an approximately 2-fold higher TCP yield compared to degradation of TCB in the SG phase. Secondly, on the contrary to the results depicted in Figure 3.9, it is not possible to obtain a satisfactory fit for both TCB and TCP profiles using Equation 3.7 and Equation 3.8. Moreover, even when the $[\cdot OH]_{ss}$ values in these equations are varied independently, no satisfactory fit for the TCP profile can be obtained (Figure 3.15).

Kinetic Formalization

Indeed, the mentioned above disagreements are rather instructive and argue for an alternative formalization of TCB degradation kinetics in the pores. Strictly speaking, Equation 3.7 and Equation 3.8 are valid for homogeneous reactions of $\cdot OH_{free}$ with TCB and TCP under steady-state approximation. In that case, it is assumed that all the reagents are able to diffuse throughout the solution freely and react with each other independently. However, in the case of the reaction in the heterogeneous porous medium, the major parts of both TCB and TCP remain adsorbed inside the SG phase. It imply that the reaction between TCB and $\cdot OH_{free}$ should not occur until $\cdot OH_{free}$ reaches the site where TCB is

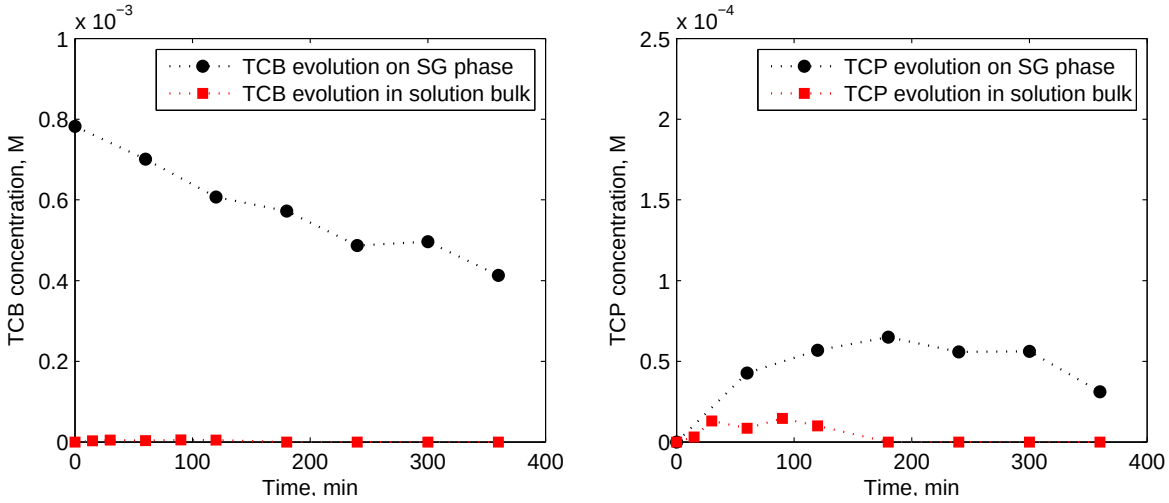

(a) (b)

Figure 3.14: Evolution of TCB (a) and TCP (b) in the solution and in the pores of a SG phase during the photocatalytic reaction. $\rho(\mathrm{TCB}) = 142$ mg L^{-1} (recalculted with respect to a virtual TCB concentration in the aqueous phase), $\rho(\mathrm{TiO_2}) = 0.1$ g L^{-1}, $\rho(\mathrm{SG})$ $= 4.0$ g L^{-1}, $I_0 = 5$ µE s^{-1}, pH 7, T = 25 °C.

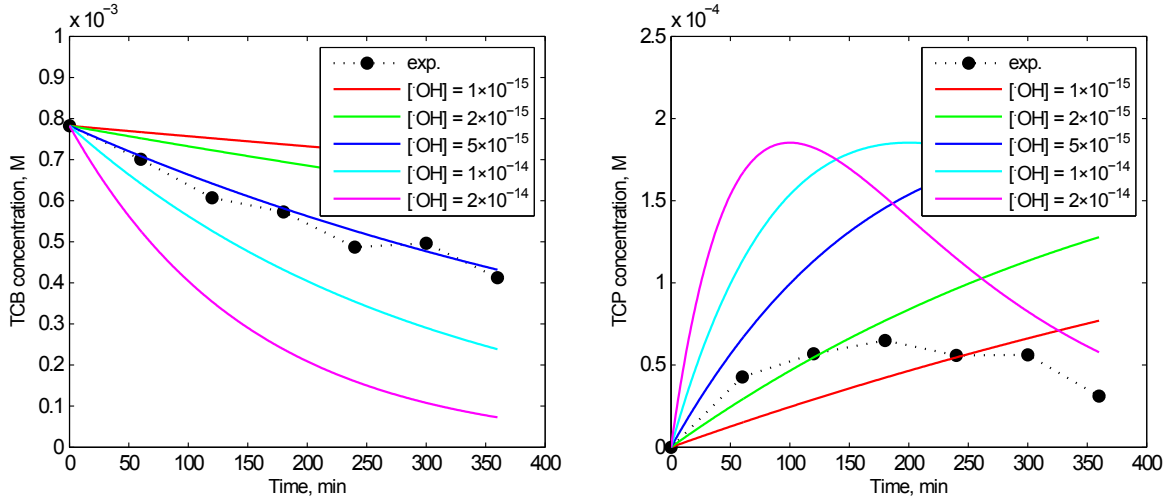

(a) (b)

Figure 3.15: Comparison between the experimental and calculated according to Equation 3.7 and Equation 3.8 kinetics profiles of TCB and TCP.

Table 3.7: Estimation of the diffusion half-lengths of $\cdot OH_{free}$ in the solution and SG pores.

Locus	A	[A], M	$t_{1/2}$, s	$L_{1/2}$, m
Solution	$\cdot OH_{free}$	8.0×10^{-14}	1.0×10^{4}	1.0×10^{-2}
Pores	TCB, TCP	1.6×10^{-1} *	5.0×10^{-10}	3.0×10^{-9}

adsorbed. Therefore, we firstly estimate the ability of $\cdot OH_{free}$ to penetrate throughout the solution and pores of the SG phase. In view of the fact that the SG pores were also filled with a solution, the half-length values of $\cdot OH_{free}$ diffusion in both media satisfy

$$L_{1/2} = 2\sqrt{D_{\cdot OH} \cdot t_{1/2}} \tag{3.11}$$

where $D_{\cdot OH} = 2.3 \times 10^{-9}$ m^2 s^{-1} is the $\cdot OH_{free}$ diffusion coefficient [223]; $t_{1/2}$ is the $\cdot OH_{free}$ half-live given by

$$t_{1/2} = 1/(k_{\cdot OH\text{-}A}[A]) \tag{3.12}$$

where $k_{\cdot OH\text{-}A}$ and [A] are the second-order rate constant (M^{-1} s^{-1}) and concentration of a species A (M) reacting with $\cdot OH_{free}$, respectively.
In the solution, $\cdot OH_{free}$ reacted with each other only and, thus, $[A] = [\cdot OH_{free}]_{ss} = 8.0 \pm 0.8 \times 10^{-14}$ M. In the pores, $\cdot OH_{free}$ predominantly reacted with TCB and $[A] \approx [TCB] = 1.6 \times 10^{-1}$ M*. Substitution of these values to Equation 3.12 and then to Equation 3.11 results in significantly different $L_{1/2}$ values for $\cdot OH_{free}$ diffusion (Table 3.7). It shows that $\cdot OH_{free}$ was able to traverse large distances through the solution, but its penetration into the pores was strongly limited by the reaction with high amounts of the adsorbed TCB. It should be kept in mind that the $L_{1/2}$ values for $\cdot OH_{free}$ diffusion in the SG pores are obtained under the assumption that the concentration of TCB did not significantly change during the process. Indeed, the TCB to TCP transformation mechanism is more complex (Figure 3.16). Firstly, $\cdot OH_{free}$ diffused through the pore of area S and attacked the TCB molecules situated along the pore depth equaled to $L_{1/2}$. After a while dt, TCB was partially converted to TCP and $\cdot OH_{free}$ reacted with both TCP and TCB until they were degraded up to poorly reacting products. Then, $\cdot OH_{free}$ diffused further and reacted with the TCB adsorbed on the depth of $L_{1/2} + dl$. It is assumed that the $\cdot OH_{free}$ reaction

*recalculated with respect to the SG phase volume.

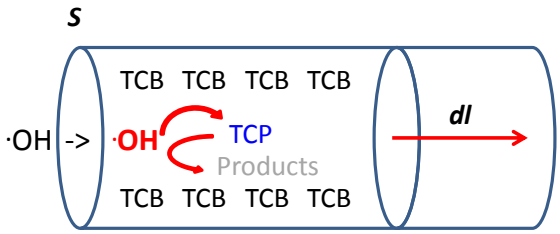

Figure 3.16: Sketch illustrating the developed kinetic model of TCB degradation in the SG pores.

zone was expanding along the pore depth at the $\cdot OH_{free}$ diffusion rate. According to the thin film theory [224], this is given by

$$\frac{dl}{dt} = D_{\cdot OH} S \tag{3.13}$$

where S is a ratio of a total SG pore entrance area to the solution volume (m^{-1}); and, thus, $\cdot OH_{free}$ reacted with the adsorbed TCB at the rate

$$\frac{d^2[\cdot OH_{bulk}]}{dtdl} = I_{abs}\Phi - \frac{D_{\cdot OH} S}{dl}[\cdot OH_{bulk}] - k_{\cdot OH\text{-}TCP}[\cdot OH_{bulk}][TCP] \tag{3.14}$$

$$\frac{d[\cdot OH_{pore}]}{dt} = \frac{D_{\cdot OH} S}{dl}[\cdot OH_{bulk}] - k_{\cdot OH\text{-}TCB}[\cdot OH_{pore}][TCB] \tag{3.15}$$

Indeed, the total number of possible combinations of the terms $D_{\cdot OH}$, S and dl resulting in a fit with experimental data is virtually infinitely large and therefore only the set, which asserts a physically realistic description of the process should be chosen. Thus, we set the $\cdot OH_{free}$ diffusion coefficient $D_{\cdot OH}$ to be equal to the self diffusion coefficient of H_2O [223]; use the S value obtained on the basis of a SG particle size value extracted from the SEM micrographs as described in subsection A.1.6 and, finally, choose the boundary conditions for the integration along dl on the basis of the described above $\cdot OH_{free}$ diffusion half-length estimations. References for the equations used for the parameters calculation are summarized in Table 3.8. Consequently, fitting of a numerical solution of the system 3.14-3.15 with the parameters summarized in Table 3.8 to the experimental data (Figure 3.17) results in the $\cdot OH_{free}$ generation quantum yield $\Phi = 0.045$.

This is, to our knowledge, the first quantitative result demonstrating quantum efficiency of generation of $\cdot OH_{free}$. We define $\cdot OH_{free}$ as those that are able to diffuse along distances

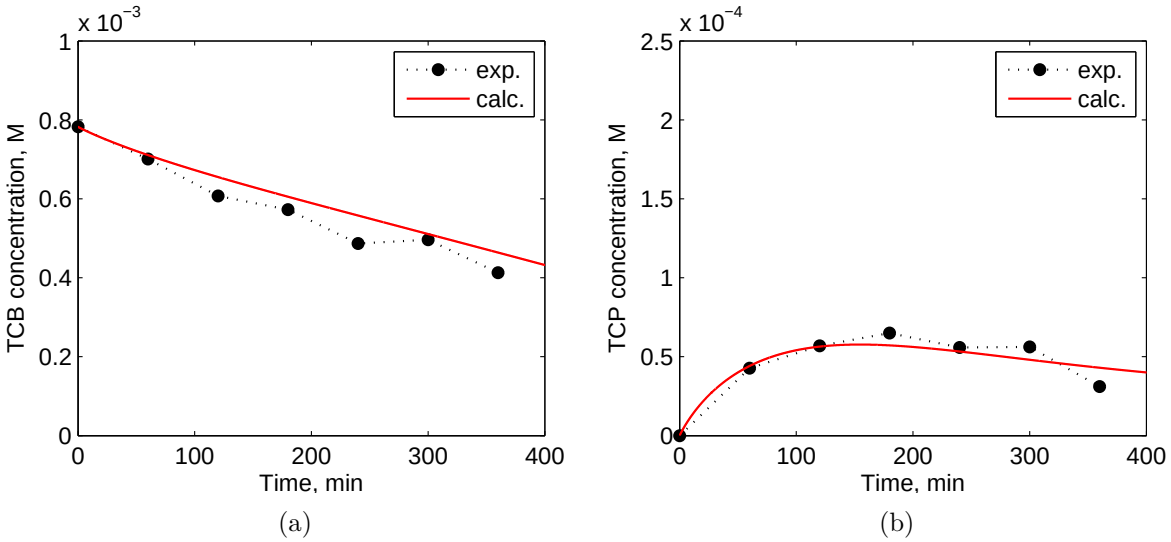

Figure 3.17: Experimental (dotted lines) and calculated on the base of numerical solution of the system of Equations 3.14-3.15 (solid lines) kinetic profiles for evolution of TCB and TCP in the SG pores.

Table 3.8: Estimated quantum yield of $\cdot OH_{free}$ generation and model parameters.

Parameter	Value	Reference
Φ	0.045	
D, $m^2\ s^{-1}$	2.3×10^{-9}	[223]
S, m^{-1}	3.076×10^{5}	Equation A.2
dl boundaries, m	0; 1.5×10^{-9}	Equation 3.11

over µm in the solution and further throughout the mesoporous SG medium. Moreover, the Φ value estimated here for the remote photocatalytic reaction is almost identical to that $\Phi = 0.042$, obtained for photocatalytic degradation of TCB in solution. Taken together, our results suggest that all the ·OH generated in irradiated suspensions of TiO_2 could be considered as $\cdot OH_{free}$. Their amounts are therefore mainly dependent on the availability of surface h^+_{VB} sites for H_2O oxidation. The fraction of the compound degraded via $\cdot OH_{surf}$-mediated mechanism should be mostly dependent on the compound adsorption and availability of $\cdot OH_{surf}$ surface sites. However, if the adsorption of a compound is low and h^+_{VB} sites are not occupied by molecules of a competing solute, h^+_{VB}-mediated oxidation of H_2O and e^-_{CB}-driven reduction of O_2 can promote intensive generation of $\cdot OH_{free}$ as well. Summing up, both h^+_{VB}-mediated oxidation of H_2O and e^-_{CB}-driven reduction of O_2 can result in generation of significant amounts of highly mobile $\cdot OH_{free}$ with quantum efficiency $\Phi = 0.045$, which is equivalent to the total quantum efficiency of ·OH generation [212].

3.2.5 Isotopic Composition of the Free OH Radicals Generated in Presence of Dissolved $^{18}O_2$

An intriguing issue, which arose the previous subsection, was devoted to the source of $\cdot OH_{free}$. It is believed that ·OH in its both surface-bound and free forms can be generated via e^-_{CB}-driven reduction of O_2 and h^+_{VB}-mediated oxidation of H_2O. As demonstrated above, illumination of an air-saturated aqueous suspension of TiO_2 can result in generation of $\cdot OH_{free}$ in amounts, equal to those of all ·OH generated in solution with dissolved TCB in subsection 3.2.1. Unfortunately, those experiments did not allow us to delineate the processes of e^-_{CB}-driven O_2 reduction and h^+_{VB}-mediated H_2O oxidation, because the reaction product of $\cdot OH_{free}$ was the same for both the processes. Therefore, we performed isotopic labeling experiments with use of $^{18}O_2$ and investigated the influence of h^+_{VB} and $\cdot OH_{free}$ scavengers on the isotopic distribution of O-atoms in formed TCP. In these experiments, aerial $^{16}O_2$ was completely replaced by $^{18}O_2$ according to the procedure described in subsection 6.3.4. Initial $^{18}O_2$ concentration was 9 mg L^{-1}; all the reaction vessels were isolated from the atmosphere and all the experiments were conducted in triplicates under the same conditions as described in subsection 3.2.4. Isotopic distribution of O-atoms in the TCP formed was determined on the base of *m/z* signals of TCP molecular ions extracted from GC-MS data. The contribution of ^{18}O-atoms contained in water on the level of its natural abundance of 0.2% was neglected. On the base of results reported previously, isotopic exchange of O-atoms between H_2O, $^{18}O_2$ and hydroxylation products was considered to be negligible [225].

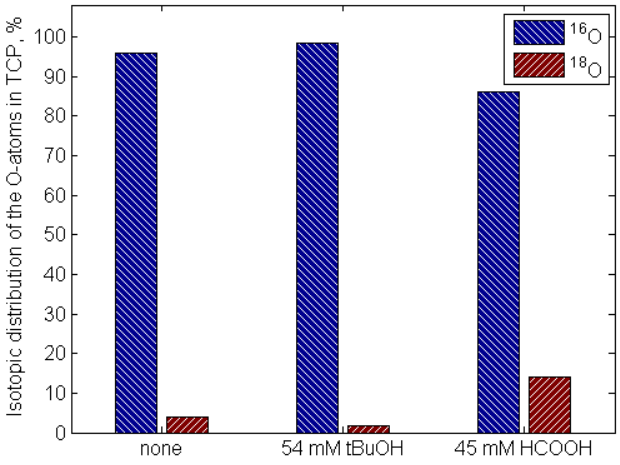

Figure 3.18: Effects of h^+_{VB} and $\cdot OH_{free}$ scavengers on the isotopic distribution of O-atoms in TCP formed upon $\cdot OH_{free}$-attack in presence of $^{18}O_2$ dissolved in $H_2{}^{16}O$. $\rho(TCB) = 142$ mg L^{-1}, $\rho(TiO_2) = 0.1$ g L^{-1}, $\rho(SG) = 4.0$ g L^{-1}, $I_0 = 5$ µE s^{-1}, 6 h irradiation time, pH 7, T = 25 °C.

Obtained results of the effects of h^+_{VB} and $\cdot OH_{free}$ scavengers on the isotopic distribution of O-atoms in TCP formed upon $\cdot OH_{free}$-attack in presence of $^{18}O_2$ dissolved in $H_2{}^{16}O$ are summarized in Figure 3.18. Results of the blank experiment (without scavengers) reveal insufficient contribution of ^{18}O in generated $\cdot OH_{free}$. The fraction of TCP containing the labeled ^{18}O-atoms was 5% and remained nearly constant during the complete 6 h of irradiation. This observation was explained by the difference in the kinetics of $\cdot OH_{free}$ generation via e^-_{CB}- and h^+_{VB}-mediated mechanisms. In particular, e^-_{CB}-reduction of O_2 is a complex 3-electron process, whereas direct oxidation of H_2O by h^+_{VB} is a rapid one-electron transfer process.

Results of the scavenging experiments with tBuOH and HCOOH also support the hypothesis of predominance of the h^+_{VB}-mediated mechanism of $\cdot OH_{free}$ formation. tBuOH is a poorly adsorbing species [204] and its reaction with h^+_{VB} sites on the TiO_2 surface was not expected. Therefore tBuOH was able to scavenge $\cdot OH_{free}$, but could not selectively retard formation of $\cdot OH_{free}$ via h^+_{VB}- or e^-_{CB}-mediated mechanisms. Accordingly, concentration of $\cdot OH_{free}$ was lowered, but the isotopic distribution of O-atoms in $\cdot OH_{free}$ changed insignificantly. On the contrary, HCOOH was adsorbed on the TiO_2 surface and acted as an efficient scavenger for h^+_{VB} and $\cdot OH_{surf}$. Therefore, concentration of h^+_{VB} available for oxidation of H_2O was lower and isotopic distribution of O-atoms in $\cdot OH_{free}$ changed towards $^{18}O_2$. Larger amounts of TCP with ^{18}O-atoms formed in presence of HCOOH agreed with this supposition. These results suggested that >95% of $\cdot OH_{free}$ were formed

out of H_2O by the direct h^+_{VB}-mediated oxidation and emphasized the high importance of availability of the TiO_2 surface for H_2O for the $\cdot OH_{free}$ generation.

3.2.6 Interim Summary

The experiments on the remote photocatalytic oxidation described above allowed us to investigate the $\cdot OH_{free}$-driven oxidation pathway of TCB selectively. It was possible to provide evidences of a high mobility of the $\cdot OH_{free}$ and high quantum efficiency ($\Phi = 0.045$) of $\cdot OH_{free}$ generation. The results obtained in the isotopic labeling experiments with the use of $^{18}O_2$ dissolved in $H_2{}^{16}O$ suggest predominance of the h^+_{VB}-mediated H_2O oxidation pathway for $\cdot OH_{free}$ generation. The low relative contribution ($<5\%$) of dissolved O_2 in the formation of $\cdot OH_{free}$ can be explained by a lower rate of the three-electron O_2 reduction by e^-_{CB} compared to the one-electron H_2O oxidation by h^+_{VB}. Nevertheless, formation of $\cdot OH_{free}$ via the e^-_{CB}-mediated reduction of dissolved O_2 can become more important, when the H_2O oxidation is suppressed by addition of h^+_{VB} scavengers.

3.3 Degradation of BPA and its Analogues by NOM-Sensitized Photolysis[‡]

Public concern about BPA safety and recent legislation has caused an intensive search on BPA alternatives. BPF, BPS and BPAF are considered as possible BPA analogues replacing BPA in consumer products [7]. As a consequence, production of BPF, BPS and BPAF is intensified and the distribution of BPs in the environment changes. In particular, relative amounts of BPF, BPS and BPAF in lake sediments increases [3]. By now, toxicological studies have shown that BPF and BPAF can exhibit toxicity, genotoxicity and estrogenic activity, similar to that of BPA, whereas BPS is considered to be less harmful [196].

Current environmental regulations do not restrict direct discharges of BPs into the aquatic environment. Therefore, understanding of their environmental fates is an issue of paramount importance. Assessment of BPs persistence requires detailed knowledge on the photo- and biodegradation rates. Recently, it has been demonstrated that photolysis in presence of NOM is one of the most important natural transformation pathways of BPA, whose rates are comparable with the biodegradation rates [17, 19]. Unfortunately, the knowledge on the rates, mechanisms and primary intermediates of photolysis of BPF, BPS and BPAF remains scarce. Although BPs are expected to have similarly weak sunlight absorbance due to similarities in their structures, their reactivity towards ROS, such as $\cdot OH$, $^1O_2$ and $\cdot O_2^-$ generated in the process of NOM-sensitized photolysis can vary. Therefore, the roles of NOM in degradation of BPF, BPS and BPAF and the formation of ROS by sunlight photolysis need to be comprehensively studied.

In this work, NOM isolated from the boggy lake Hohloh, Black Forest, Germany, was chosen as a natural sensitizer for the investigation of photolysis of BPF, BPS and BPAF under simulated solar light. Hereafter, the NOM sample used will be denoted as HO24 (specific code according to sampling). Extensive information on the HO24 characteristics is given in subsection 6.1.3. The rates of NOM-sensitized and direct photolysis of BPs were compared in order to estimate their photolability in presence/absence of HO24. Further, effects of Fe^{3+}, NO_3^- and HCO_3^- on the rates of HO24-sensitized BPs degradation were studied. Applied concentrations of these ions were typical for surface waters. In addition, the role of $\cdot OH$ was examined using isopropanol (iPrOH) as a selective scavenger. Major BPs products formed during the NOM-sensitized photolysis were determined by

[‡]The main findings presented in this section have been submitted to *Environmental Science & Technology* by Kondrakov et al. [226]

an accurate mass HPLC-MS-MS/ToF analysis. Finally, in order to get insights in the mechanisms of ROS generation by HO24-sensitized photolysis, kinetic isotope effects of dissolved O_2 and solvent by the use of $^{18}O_2$ and D_2O, respectively, were investigated.

3.3.1 Kinetics of Bisphenols (BPs) Degradation

Degradation of BPs by Direct Photolysis

Degradation of BPs by direct sunlight requires absorption of the photons of energies, which are high enough for BPs bonds breaking. Dissociation energies of the bonds in the phenolic and bridge groups of BPs tend to lie in the range between 250 and 400 kJ mol^{-1} [227] and correspond to the UVA photons energies.

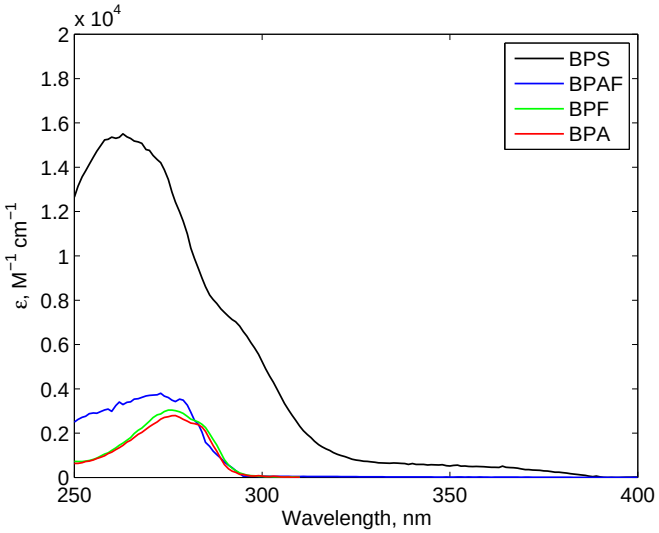

(a)

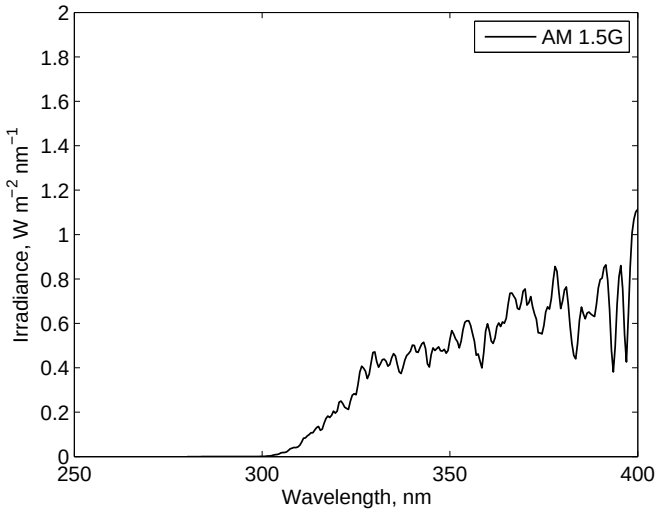

(b)

Figure 3.19: UV spectra of BPA, BPF, BPS and BPAF (a) and a UVA fraction of AM1.5G solar irradiance spectrum (b).

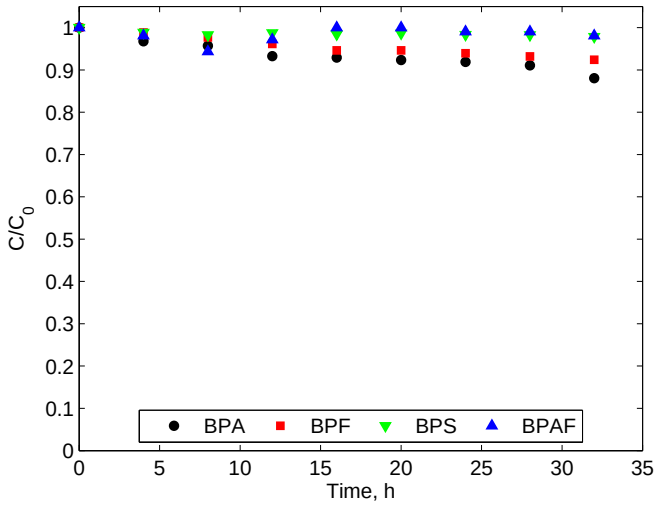

Figure 3.20: Degradation of BPs by direct photolysis under simulated solar light. ρ_0(BPA) = ρ_0(BPF) = ρ_0(BPS) = 10 mg L^{-1}, ρ_0(BPAF) = 3 mg L^{-1}, I_0 = 5 µE s^{-1}, c_0(iPrOH) = 140 mM, pH 7, T = 25 °C.

UVA photons constitute a relatively small part of the solar light spectrum, which makes sufficient absorbance of BPs in this region the necessary condition for direct photolysis. Figure 3.19 gives a comparison between the UV absorption spectra of BPs and the spectum of solar irradiance in the UVA region. All the BPs investigated exhibit wide shouldered spectra with maxima in the range between 260 and 280 nm, that are typical for bisphenol-like structures [50–52, 194]. Nevertheless, only the spectra of BPS and BPAF demonstrate significant overlap with the solar spectrum. Integral UV light absorbances of BPA, BPF and BPAF are similarly weak and ranged as BPAF>BPF>BPA, whereas absorbance of BPS is significantly higher, which can be ascribed to a higher degree of conjugation via the bridging sulfonyl group. In view of the fact that the proper light absorption is a necessary but not sufficient condition of the direct photolysis, the kinetics of BPs degradation upon irradiation by simulated solar light was investigated (subsection 6.3.2). It should be noted that in our preliminary experiments on the direct BPs photolysis, we concluded that mutual interactions between excited BP molecules could lead to the enhancement of the degradation via autosensitized photolysis involving reactions with ·OH or other radicals as discussed in subsection A.1.2. In order to assure that BPs degradation was purely driven by a photolytic cleavage, iPrOH was added as a scavenger for radical species, which could be potentially formed in side reactions.

While BPA and BPF were relatively slowly degraded, nearly no degradation of BPS and BPAF was observed (Figure 3.20). In spite of the lower absorbance, BPA was rapidly

Table 3.9: Quantum yields of direct photolysis (Φ) and half-live times ($t_{1/2}$) of BPs.

Compound	$t_{1/2}$, d	Φ
BPA	14	0.0006
BPF	17	0.0006
BPS	104	3×10^{-7}
BPAF		≈0

photolyzed due to the formation of stable isopropylphenyl and phenyl radicals, as previously reported [206]. Thus, in view of structural similarities of BPA and BPF, it seems to be reasonable to explain the similarly rapid degradation of BPF suggesting formation of stable radicals as well. In much the same way, we interpret the slow degradation of BPS and BPAF in terms of energetic unfavourableness of their radical intermediates formed upon the photolytic cleavage.

Table 3.9 summarizes values of the half-live times ($t_{1/2}$) and photolysis quantum yields (Φ) of BPs. The $t_{1/2}$ and Φ values were calculated out of pseudo-first-order rate constants and according to Equation 3.3, respectively. The pseudo-first-order rate constants were estimated by linear regression of the relative logarithmic kinetic profiles of BPs (subsection A.1.2). The $t_{1/2}$ value obtained for BPA agrees well with the BPA half-live time reported previously [19]. All the other $t_{1/2}$ and Φ values presented in Table 3.9 have been determined for the first time. Assessment of the calculated $t_{1/2}$ values suggests that direct photolysis may be an essential degradation pathway for BPA and BPF, whose rates are similar to the rates of biodegradation [38], but degradation of BPS and BPAF via direct photolysis is rather unessential.

Degradation of BPs by HO24-Sensitized Photolysis

In view of the fact that degradation of BPA by sensitized photolysis in presence of NOM was found to be as essential as biodegradation [19], it was reasonable to expect similar photolysis rates for BPF, BPS and BPAF. Indirect photolysis seems to be an especially important degradation pathway for BPS and BPAF, since the rates of their direct photolysis have been found to be negligible (section 3.3.1). By now, importance of HO24-sensitized photolysis has been investigated only for BPA and all the other BPs remained unexplored. Therefore, experiments assessing the sensitizing role of HO24 in the processes of degradation of BPF, BPS, BPAF and BPA (for comparison) under simulated solar light were designed.

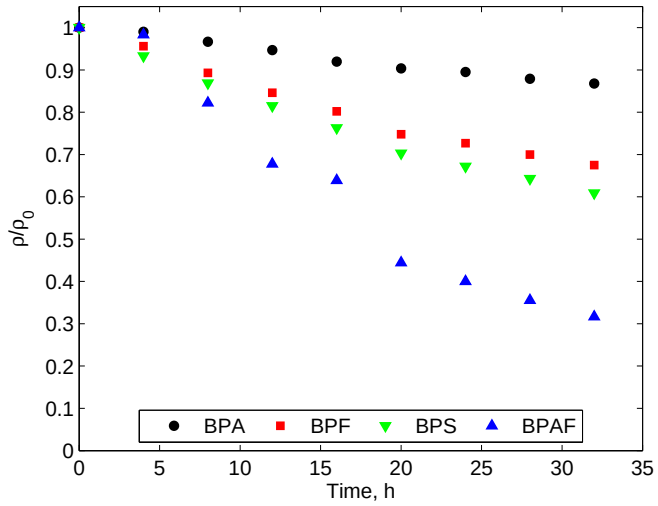

Figure 3.21: Degradation of BPA, BPF, BPS and BPAF in presence of HO24. ρ(HO24) = 8.5 mg (C) L^{-1}, ρ_0(BPA) = ρ_0(BPF) = ρ_0(BPS) = 10 mg L^{-1}, ρ_0(BPAF) = 3 mg L^{-1}, I_0 = 5 µE s^{-1}, pH 4.8 (not adjusted), T = 25 °C.

Table 3.10: Half-live times ($t_{1/2}$) for degradation of BPs by HO24-sensitized photolysis.

Compound	$t_{1/2}$, d
BPA	7.8
BPF	2.2
BPS	1.8
BPAF	0.75

Kinetic profiles of degradation of BPA, BPF, BPS and BPAF by HO24-sensitized photolysis are shown in Figure 3.21. The HO24-sensitized photolysis degradation rates can be ranked as BPAF>BPS>BPF>BPA, while the data on the degradation of BPs by direct photolysis given in section 3.3.1 suggest an inversed order: BPA>BPF>BPS>BPAF. This is possibly because the mechanisms of the BPs degradation by direct and HO24-sensitized photolysis are different. Direct photolysis of BPs was conducted in presence of iPrOH as a radical scavenger, and the BPs degradation was merely driven by photolytic cleavage. In the case of HO24-sensitized photolysis, HO24 absorbed nearly all the UVA photons due to the inner filter effect (subsection A.1.3), and the BPs degradation was primarily driven by ROS due to the sensitizing effect of HO24. However, the differences in the rates of HO24-sensitized photolysis of different BPs are unexpectedly large. BPs are structurally similar electron-rich compounds and it is reasonable to expect nearly equal reactivity of ROS towards them [104, 175]. Therefore, we suppose that the efficiency of

ROS generation could vary depending on the BPs presented. Since the observations of the enhanced degradation of BPs by autosensitized photolysis (subsection A.1.2) suggest that BPs transients formed upon photoexcitation were relatively stable, a significant degree of interactions between BPs and HO24 could be expected as well. Such interactions may affect the lifetimes of the triplet HO24 transients, ^{3}HO24*, responsible for the ROS generation [228].

Notably, the BPs half-live values ($t_{1/2}$) estimated for the process of HO24-sensitized photolysis (Table 3.10) are even higher than those reported for biodegradation [38, 54] (details on the $t_{1/2}$ calculation are given in subsection A.1.2). The value $t_{1/2}$ = 7.8 d obtained for BPA degradation by HO24-sensitized photolysis agrees well with the value $t_{1/2}$ = 7.2 d reported for degradation of BPA in presence of autochthonous NOM [19]. The $t_{1/2}$ values obtained for the degradation of BPF, BPS and BPAF have been reported in this study for the first time.

3.3.2 Role of OH Radicals

Kinetics

Among ROS generated by HO24-sensitized photolysis, ·OH posses the highest reactivity towards most of the organic compounds. Therefore ·OH are expected to play the major role in degradation processes [228]. Experiments with radical scavengers are well suited to estimate the roles and quantities of ·OH [17]. Use of iPrOH as a scavenger provides an important advantage for such experiments: It has a high scavenging selectivity for ·OH; iPrOH does not act as a light attenuator in the UVA range and is not expected to be able to affect the lifetime of $^1O_2$, which can participate in the degradation process as well [17, 229]. By now, the role of ·OH in degradation by HO24-sensitized photolysis has been investigated only for BPA and all the other BPs have been overlooked. Therefore, we used the scavenging effect of iPrOH to investigate the ·OH-mediated pathways of degradation of BPA (for comparison with literature data), BPF, BPS and BPAF and tried to distinguish them from processes driven by other ROS, e.g. $^1O_2$.

Profiles of the BPs degradation by HO24-sensitized photolysis in presence and absence of iPrOH obey the first-order kinetics and can be therefore directly compared with each other in terms of the first-order rate constants. Figure 3.22 summarizes the k values and demonstrates distinct changes in the BPs degradation rates resulted by addition of iPrOH (details on the calculation of the k values are given in subsection A.1.2). These data suggest that ·OH significantly contributed to the degradation of BPs, but their amounts varied among the different BPs. More rigorously, the pseudo-first-order rate constants k

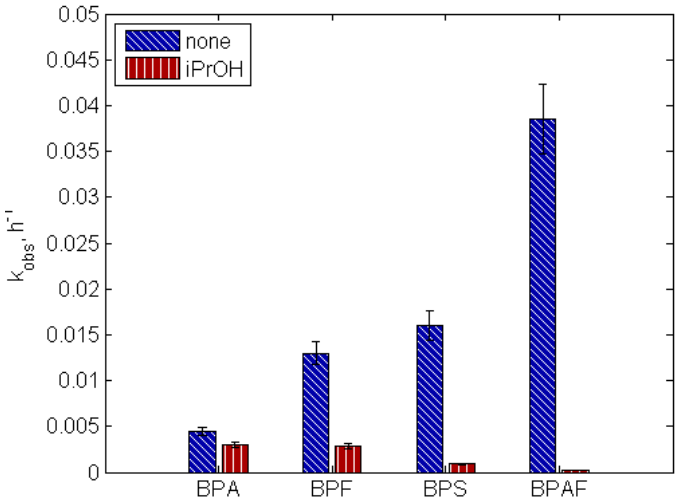

Figure 3.22: Degradation of BPs in presence of HO24 and iPrOH. ρ(HO24) = 8.5 mg (C) L^{-1}, ρ_0(BPF) = 10 mg L^{-1}, ρ_0(BPS) = 10 mg L^{-1}, ρ_0(BPAF) = 3 mg L^{-1}, c_0(iPrOH) = 140 mM. The k values are summarized in Table A.2

can be analyzed in terms of ·OH concentrations. By the analogy with Equation 3.4, k should be written as

$$k = k_{\cdot\text{OH-BPs}}[\cdot\text{OH}] + k_{iPrOH} \tag{3.16}$$

where $k_{\cdot\text{OH-BPs}}$ is the second-order rate constant of the reaction between BPs and ·OH (M^{-1} s^{-1}); [·OH] is the stationary concentration of ·OH (M) and k_{iPrOH} is the apparent rate constant of BPs degradation by HO24-sensitized photolysis in presence of iPrOH (s^{-1}).

Thus, Equation 3.16 shows that the term k grows with increasing [·OH] and k_{iPrOH} values. As demonstrated in Figure 3.22, in the order BPA>BPF>BPS>BPAF, the k values grow, whereas the k_{iPrOH} term decreases. Therefore, the k growth is due to the increase of the [·OH] term, since we suppose that $k_{\cdot\text{OH-BPs}}$ does not vary significantly. This supposition is based on the fact that the value $k_{\cdot\text{OH-BPA}} = 1 \times 10^{10}$ M^{-1} s^{-1} [102] is an exteremely high value, which is nearly equal to the diffusion controlled reaction rate constant $k_D = 1.5 \times 10^{10}$ M^{-1} s^{-1} [230] and therefore $k_{\cdot\text{OH-BPF}} \approx k_{\cdot\text{OH-BPF}} \approx k_{\cdot\text{OH-BPAF}} \approx k_{\cdot\text{OH-BPA}} \leq k_d$. Hence, this analysis demonstrate that the BPs degradation rates are directly dependent on the concentrations of ·OH.

Mechanism

·OH-attack on an aromatic ring resulting in the formation of catechol-like intermediates was reported to be the primary pathway of BPA degradation by NOM-sensitized photolysis [17]. Importantly, BPA cathechols have been found to cause an estrogenic response at concentrations one order higher than BPA and therefore assumed to have lower estrogenic activity [196]. Moreover, the extensive estrogenic activity data obtained for BPs-related compounds in ovariectomized mice and MCF-7 cells suggest an important relationship between estrogenic activity and BPs structure [196]. It has been shown that the introduction of an additional hydroxyl group into the aromatic ring or hydroxylation of the propane bridge group can significantly lower the activity [196]. By now, identification of the intermediates formed by HO24-sensitized photolysis was conducted for BPA only and we therefore paid a special attention to the analysis of the products of BPF, BPS and BPAF degradation.

Results of the HPLC-MS-MS/ToF analysis reveal predominance of catechol-like structures among the products of all the BPs investigated. Table 3.11 summarizes the MS data on the obtained $[M\text{-}H]^-$ values. Incorporation of an O-atom in the BPs phenolic rings can be readily figured out from the difference of 16 between the $[M\text{-}H]^-$ values of the parent BPs and their products. Further analysis of the MS-MS spectra (subsection A.1.7) confirms the catechol-like structures of the products given in Table 3.11. In view of the structure–estrogenic-activity relationship mentioned above, we dare to presume tentatively, that degradation via the detected catechols-mediated pathway should result in a decrease of the estrogenic activity for all the BPs investigated [196].

Table 3.11: HPLC-MS-ToF data on BPs and their intermediates formed by HO24-sensitized photolysis.

Compound name	$[M\text{-}H]^-$, m/z	Formula
BPA	227.1073	$C_{15}H_{16}O_2$
BPA catechol	243.1021	$C_{15}H_{16}O_3$
BPF	199.0766	$C_{13}H_{12}O_2$
BPF catechol	215.0712	$C_{13}H_{12}O_3$
BPS	249.0230	$C_{12}H_{10}SO_4$
BPS catechol	265.0176	$C_{12}H_{10}SO_5$
BPAF	355.0505	$C_{15}H_{10}F_6O_2$
BPAF catechol	361.0457	$C_{15}H_{10}F_6O_3$

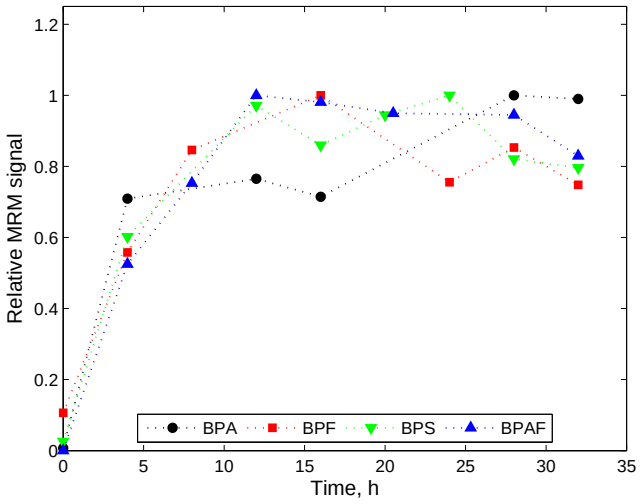

Figure 3.23: Results of HPLC-MRM measurements of the detected catechol intermediates of BPs formed by HO24-sensitized photolysis.

Formation of BPs' catechols was also followed throughout the reaction by HPLC coupled with a multiple reaction monitoring (MRM) mass analysis. Due to the possibility of the HPLC-MRM method to monitor the ions formed upon the target $[M\text{-}H]^-$ fragmentation, the BPs' catechol formation profiles could be obtained with a high selectivity. Figure 3.23 represents the relative profiles of the BPs' catechols formation. On the basis of the HPLC-MRM results, an assignment of the HPLC-UV peaks (from the chromatograms acquired in parallel) to the HPLC-MRM retention times can be conducted. Examination of the UV spectra of BPs' catechols demonstrate that hydroxylation caused a negligible shift of 3 nm to the longer wavelength range (subsection A.1.4). Therefore, the yields of the BPs' catechols generation can be estimated according to Equation 3.17 and compared with the values of BPs conversions (Table 3.12).

$$Y_{\text{BP catechol}} = \frac{A_{\text{BP catechol}}}{A_0(\text{BP})} \cdot 100\% \tag{3.17}$$

where $A_{\text{BP catechol}}$ and $A_0(\text{BP})$ are the HPLC-UV peak areas of the BP catechols and BPs, respectively.

As demonstrated in Table 3.12, BPAF conversion is similar to the $Y_{\text{BP catechol}}$ value of BPAF catechol suggesting that hydroxylation was the predominant degradation pathway. However, conversions of BPA, BPF and BPS are significantly larger that their $Y_{\text{BP catechol}}$ values and we therefore suppose involvement of alternative degradation pathways for

Table 3.12: Formation yields of BPs' catechols identified in the BPs degradation by HO24-sensitized photolysis.

Compound name	$Y_{\text{BP catechol}}$, %	BPs conversion, %
BPA catechol	4	10
BPF catechol	6	30
BPS catechol	4	40
BPAF catechol	57	70

these BPs. For these compounds, only traces of dicatechol-like products were detected, but their formation profiles could not be followed. Unfortunately, further identification of the BPs' intermediates by non-target HPLC-MS analysis was strongly limited by the presence of the compounds formed upon the degradation of HO24 itself. Nevertheless, the experiments with iPrOH together with the HPLC-MS-MS/ToF data on the BPs' catechols formation explicitly demonstrate that ·OH play an important role in the degradation of BPs by HO24-sensitized photolysis.

3.3.3 Effects of Fe^{3+}, HCO_3^- and NO_3^- on the BPs Degradation

In natural waters, generation of ROS is affected by the omnipresent inorganic constituents, such as Fe^{3+}, NO_3^- and HCO_3^-. Although it has been reported that, Fe^{3+} and NO_3^- may serve as additional ROS sources, Figure 3.24 shows that these ions caused neutral or rather negative effects on the BPs degradation. It is believed that Fe^{3+} may give rise to ·OH via photo-Fenton-like mechanism involving Fe^{2+} species formed upon a Fe^{3+} complexation by NOM [17, 228, 231]. Apparently, there was no substantial interaction between Fe^{3+} and HO24. The negative effect of NO_3^- can be caused by scavenging of ·OH or by direct light attenuation [228]. The value $k_{\text{·OH-}NO_3^-} = 2.8 \times 10^5$ M^{-1} s^{-1} [219] is almost 5 orders of magnitude lower than, e.g. $k_{\text{·OH-BPA}} = 1.0 \times 10^{10}$ M^{-1} s^{-1} [102]. Accordingly, the decrease in the BPs degradation rates was due to the light attenuation effect of NO_3^-. The observed negative effect of HCO_3^- on ·OH generation can be ascribed to scavenging due to the direct reaction between HCO_3^- and ·OH with relatively high $k_{\text{·OH-}HCO_3^-} = 1.0{\times}10^7$ M^{-1} s^{-1} [170]. Thus, BPs degradation by HO24-sensitized photolysis can be to some extent suppressed by the presence of Fe^{3+}, NO_3^- and HCO_3^- at concentrations typical for natural waters, but it is still significantly more rapid than that observed in the direct photolysis experiments.

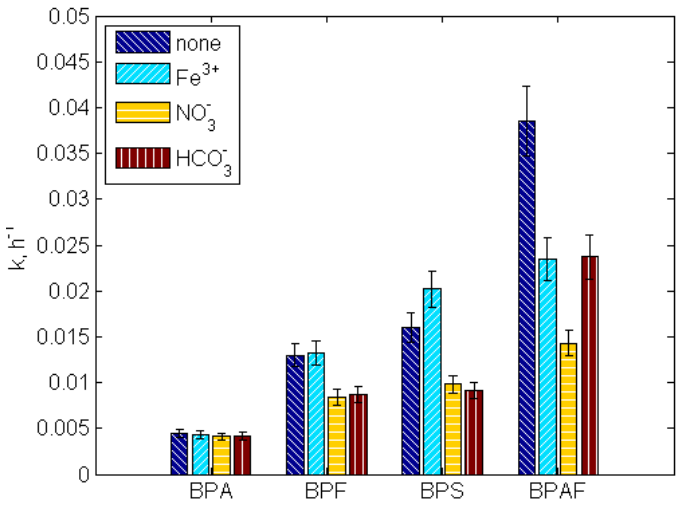

Figure 3.24: Effects of HCO_3^-, NO_3^- and Fe^{3+} on BPs degradation in presence of HO24. ρ(HO24) = 8.5 mg (C) L^{-1}, ρ_0(BPF) = 10 mg L^{-1}, ρ_0(BPS) = 10 mg L^{-1}, ρ_0(BPAF) = 3 mg L^{-1}, c(HCO_3^-) = 0.5 mM, c(NO_3^-) = 0.5 mM, c(Fe^{3+}) = 7 µM, $I_0 = 5$ µE s^{-1}, pH 4.8 (not adjusted), T = 25 °C. The k values are summarized in Table A.2.

3.3.4 Mineralization of Dissolved Organic Carbon (DOC) and Structural Changes of HO24

Results on the scavenging effect of iPrOH and HPLC-MS data presented in the previous subsection demonstrate predominance of the ·OH-driven oxidation of BPs in HO24-sensitized photolysis. It is important to note that due to a high content of electron-rich aromatic carbon, HO24 possesses high reactivity towards ·OH as well. Moreover, the process of the HO24-sensitized ·OH generation can occur via an electron transfer mechanism [232], in which HO24 can act as electron donor and partially degrade. Because of an inherent relation between the sensitizing properties of NOM and its molecular structure [19], it was important to follow the structural changes of HO24 in the process. To this end, the molecular size distribution and spectral properties of HO24 have been investigated by the SEC-DOC/UV/FL method. Below, we discuss the SEC chromatograms obtained in the BPA degradation experiments; the SEC chromatograms from the experiments with BPF, BPS and BPAF exhibit very similar profiles and are given in subsection A.1.5. All BPs could not be observed in SEC runs of the blank BPs solutions during the elution time and 6 h afterwards, therefore, they were assumed to be strongly retained in the column.

Figure 3.25 shows the SEC chromatograms of the samples before and after 32 h of irradiation.

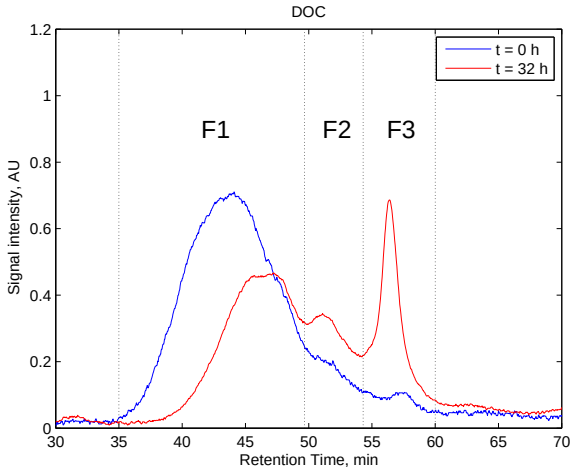

(a)

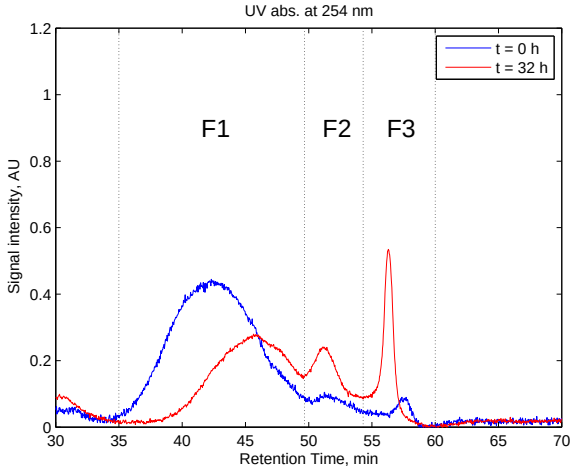

(b)

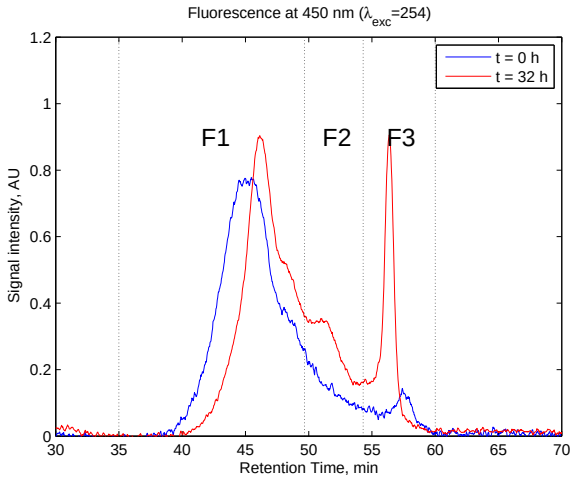

(c)

Figure 3.25: SEC-DOC/UV/FL chromatograms of the HO24 samples taken during degradation of BPA by HO24-sensitized photolysis.

Table 3.13: SEC/DOC/UV/FL analysis of HO24 fractions F1, F2 and F3 before and after 32 h of the HO24-sensitized photolysis. Percentages of differently detected fractions were calculated relatively to the initial integral DOC, UV and FL signals.

	F1		F2		F3		Sum	
	0 h	32 h	0 h	32 h	0 h	32 h	0 h	32 h
DOC, %	82	44	11	18	7	22	100	84
UV, %	87	47	8	17	5	15	100	79
FL, %	80	67	13	24	8	22	100	112

Analysis of the SEC-DOC signals reveals three major DOC fractions denoted as F1, F2 and F3. In accordance with the SEC data previously reported for lake Hohloh samples [233, 234], we suppose that F1, F2 and F3 correspond to the humic material, aromatic organic acids and the low-molecular-mass HO24 substances, respectively.

After 32 h of irradiation, the relative DOC content in the HO24 fractions had changed and its integral amount decreased (Table 3.13): DOC in F2 and F3 increased, whereas DOC in F1 descended and its maximum shifted towards longer retention times. These data argue for a fragmentation-mediated mineralization of HO24. Nevertheless, in spite of the partial mineralization, the integral UV_{254} absorbance and, thus, the aromaticity of the DOC did not significantly decreased during the process. Moreover, the fluorescence intensity in F2 and F3 increased, possibly due to the loss of high molecular fluorescence quenching.

These results suggest that HO24 mineralization involved not only the decay of aromatic carbon via ·OH-driven ring opening, but was accompanied by an electron donation that increased the electronic conjugation of HO24 as well. Summing up, we conclude that in the process of HO24-sensitized photolysis, a significant part of HO24 underwent fragmentation (up to the mineralization), but its spectral properties and sensitizing activity remained the same.

3.3.5 Kinetic Isotope Effects (KIEs) of Solvent and Dissolved Oxygen

In the previous subsection, we have demonstrated that HO24-sensitized generation of ·OH was accompanied by fragmentation of HO24 up to its partial mineralization. Even though the aromatic moieties of HO24 could be primarily targeted to ring opening via ·OH-attack, the unsaturated character of the HO24 DOC remained fairly constant during the process and its integral fluorescence even increased. It implied that HO24 could act as an electron donor for the generation of ·OH out of O_2 or other ROS [235]. In view

Table 3.14: KIEs of D_2O and $^{18}O_2$ for BPA degradation by HO24-sensitized photolysis.

Presenting compound	Expected reactivity of the single species $^3NOM^*$	$^1O_2$	·OH	Observed $k_{^{18}O,\ D}/k_{^{16}O,\ H}$
D_2O	high	high	normal	1.9
$^{18}O_2$	high	normal	low	1.3
$^{18}O_2$ + D_2O	high	high	low	1.3

of the fact that ROS consists of H- and O-atoms originating from H_2O and dissolved O_2, we have investigated the KIEs of D_2O and $^{18}O_2$ in order to better understand these transformations. The kinetic, HPLC-MS and SEC-DOC/UV-FL data obtained for the different BPs demonstrated great similarities in their degradation mechanisms and we have decided to conduct the KIEs experiments with BPA, as an exemplary BPs representative. The KIEs are expressed as a ratio of $k_{^{18}O,\ D}$ to $k_{^{16}O,\ H}$, where $k_{^{18}O,\ D}$ is the pseudo-first-order rate constants obtained for BPA degradation in presence of D_2O or $^{18}O_2$; $k_{^{16}O,\ H}$ is the apparent first-order rate constant obtained for BPA degradation in presence of H_2O or $^{16}O_2$.

Table 3.14 summarizes the available data on the KIEs of D_2O and $^{18}O_2$ on the reactivity of single species involved in the process of HO24-sensitized photolysis [229, 236, 237]. Firstly, $^3HO24^*$ quenching efficacy of D_2O and $^{18}O_2$ could be expected to be significantly lower than that of H_2O and $^{16}O_2$, respectively [229, 236]. Their substitution could result in the extended $^3HO24^*$ lifetimes and, thus $k_{^{18}O,\ D}/k_{^{16}O,\ H} > 1$. Then, the lifetime of $^1O_2$ is an order of magnitude higher in D_2O compared to H_2O, which should result in $k_{^{18}O,\ D}/k_{^{16}O,\ H} \geq 10$ [229]. The $^1O_2$ lifetimes in presence of $^{18}O_2$ in both H_2O and D_2O are identical [229], and we therefore assumed no $^{18}O_2$ KIE on $^1O_2$. And finally, for the ·OH generation in presence of D_2O and $^{18}O_2$, we suppose rather negative KIEs ($k_{^{18}O,\ D}/k_{^{16}O,\ H} \leq 0.9$) due to the lowering of the protonation and O-O bond breakage rates, respectively [237].

The last column of Table 3.14 summarizes the experimentally observed $k_{^{18}O,\ D}/k_{^{16}O,\ H}$ values. The positive KIE of D_2O with $k_{^{18}O,\ D}/k_{^{16}O,\ H} = 1.9$ observed is not high enough to regard the process as a $^1O_2$-driven one. By the analogy with the findings reported previously [238], the relatively low positive KIE of D_2O can be interpreted as predominance of an electron transfer mechanism mediated by $^3HO24^*$ transients. Furthermore, the positive KIE observed for $^{18}O_2$ imply, that increase in the $^3HO24^*$ lifetime prevailed over the ·OH generation retardation. Nevertheless, no synergy of the KIEs of $^{18}O_2$ and D_2O can be observed. Their combined KIE are the same as that of single $^{18}O_2$ and lower than the

D_2O KIE. We therefore suppose that despite the further $^3HO24^*$ lifetime increase, the overall degradation rate was limited by the ·OH generation efficiency. Interestingly, the latter is not significantly affected by the substitution of $^{16}O_2$ to $^{18}O_2$, but is rather associated with the $^3HO24^*$ lifetime. Moreover HPLC-MS-ToF analysis revealed that all the OH-groups in the BPA catechol molecule originated neither from dissolved $^{18}O_2$ nor from $D_2{}^{16}O$. It suggest that ·OH could be generated via a homolitic cleavage of the OH-groups of the HO24 molecules rather than via less facile mutual ROS reactions.

3.3.6 Interim Summary

Among the BPs investigated, only BPAF was stable under direct simulated solar irradiation. Nevertheless, in presence of HO24, degradation of all the BPs resulted in formation of catechol-like intermediates with the $t_{1/2}$ values in the range between 0.75 and 7.8 days. The rates of BPs degradation by HO24-sensitized photolysis were insignificantly affected by the presence of Fe^{3+}, NO_3^- and HCO_3^- at the concentrations typical for surface waters. Results of the KIEs experiments and experiments with iPrOH as a scavenger suggest that presence of HO24 led to generation of ·OH via the $^3HO24^*$-mediated mechanism. Although, the $^3HO24^*$-mediated ·OH generation was accompanied by the partial (up to 20%) mineralization of HO24, no retardation of the BPs degradation could be observed.

4 Summary

Recently, public concern about the environmental safety of BPA caused changes in legislation and stimulated an intensive search on BPA alternatives. As a result, the use of non-regulated BPs, such as BPF, BPS and BPAF, has drastically been broaden and the volumes of the total worldwide BPs production has reached 5.4 millions tons per year. By now, existing regulations deal with content of BPs in the end-products only and do not restrict the BPs emissions into the environment, e.g. by direct discharges from the wastewater treatment plants. Moreover, the conventional wastewater treatment is not capable to eliminate BPA below PNEC levels. Heterogeneous TiO_2 photocatalysis utilizes the energy of the solar light for generation of ROS and can essentially excel the alternative wastewater treatment methods in both energy efficiency and efficiency of BPs removal. In the natural environment, sunlight photolysis sensitized by NOM is an important pathway of the ROS-driven transformations of BPs, whose rates can exceed the rates of biodegradation. Thus, both the fundamental and practical knowledge on transformations of BPs in photocatalytic and photolytic processes is important for developing efficient water treatment techniques and for understanding the environmental fate of BPs.

In this perspective, the work explores potentials of TiO_2 photocatalysis and UV photolysis for the degradation of BPA focusing on the particular roles of the major ROS ($\cdot OH$ and h^+_{VB}) in the process (section 4.1); the sources, amounts and mobility of photocatalytically generated $\cdot OH$ are investigated in isotopic labeling experiments (section 4.2), and, finally, this work deals with the photolysis of BPA, BPF, BPS and BPAF occurring in presence of NOM as a sensitizer in order to estimate the potentials of environmental persistence of BPs and their transformation products (section 4.3).

4.1 Degradation of BPA by TiO_2 Photocatalysis and UV Photolysis

It has been reported that degradation of BPA by TiO_2 photocatalysis can be accompanied by formation of intermediates leading to an increase in the overall estrogenic activity of the solution [183]. Also, it has been pointed out [196], that *in vitro* and *in vivo* endocrine-disrupting activity of BPs is directly related to the molecular structure, particularly to the positions and number of hydroxyl groups in the aromatic rings. By now, only a few intermediates of BPA photocatalytic degradation were suggested on the base of HPLC-MS data on molecular ions or GC-MS spectral data, but no further reliable structural information has been obtained [180, 184–194, 239–241].

This study focuses on identification of aromatic, particularly phenolic, products of BPA and on elucidation of their formation pathways. The use of an enhanced HPLC–MS–MS/ToF approach allowed us to find out five new BPA intermediates. Among them, a hazardous DNA-binding agent, BPA 3,4-quinone (BPAQ), has been detected. To clarify the mechanism of BPAQ formation, a comparative study of BPA degradation by TiO_2 photocatalysis and UV photolysis at $\lambda = 254$ nm has been conducted. UV photolysis produced two catechol derivatives with potentially lower endocrine-disrupting activity in comparison to BPA. $\cdot OH_{free}$ scavenging experiments with tBuOH revealed oxidation of BPA at the TiO_2 surface. Hydroxylation of BPA by $\cdot OH_{free}$ in solution led to formation of drastically different intermediates (Figure 4.1). In particular, scavenging of $\cdot OH_{free}$ induced a mechanism change and intensified BPAQ formation. It imply that formation of BPAQ and its further quinone-like products proceeded via reaction of BPA catechols with h^+_{VB} or $\cdot OH_{surf}$ directly at the TiO_2 surface. Summing up, UV photolysis can be feasible for elimination of BPA rather than for its mineralization, whereas the photocatalytic process

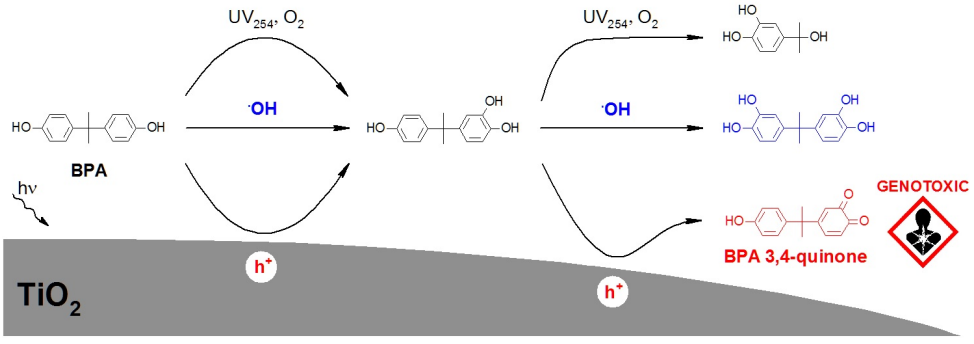

Figure 4.1: Principal differences in the pathways of BPA degradation by TiO_2 photocatalysis and UV photolysis.

provides complete BPA mineralization, but can proceed via h^+_{VB}-mediated conversion of BPA to potentially genotoxic quinone-like intermediates.

4.2 Relative Roles of Free and Surface-Bound OH Radicals in TiO_2 Photocatalysis

Methods of ESR trapping have been extensively used for ·OH detection [121, 139, 208, 209]. However, interpretation of ESR data remains a challenging task, because different types of ·OH, $\cdot OH_{free}$ and $\cdot OH_{surf}$, as well as h^+_{VB}, can react with the spin traps identically, so unambiguous assignment of the observed ESR signals is not always possible [14]. Nevertheless, data on degradation of isotopically labeled organic compounds with different adsorption affinities towards TiO_2 surface suggest that photocatalytic oxidation of organic compounds can occur via a dual $\cdot OH_{surf}/\cdot OH_{free}$-mediated mechanism [14, 139]. As far as we know, no quantitative data on the specific contributions of $\cdot OH_{surf}$ and $\cdot OH_{free}$ in the overall photocatalytic performance have been reported yet. The dual $\cdot OH_{surf}/\cdot OH_{free}$-mediated mechanism remains under debate and general understanding of photocatalytic oxidation is not consistent [12, 13].

The experiments on the remote photocatalytic oxidation described above allowed us to investigate the $\cdot OH_{free}$-driven oxidation of TCB selectively (Figure 4.2-a). We have evidenced a high quantum yield ($\Phi = 0.045$) of $\cdot OH_{free}$ generation, identical to that, reported as the overall quantum yield of ·OH generation in TiO_2 photocatalysis [212]. The results obtained in the isotopic labeling experiments with the use of $^{18}O_2$ dissolved in $H_2{}^{16}O$ suggest predominance of the h^+_{VB}-mediated H_2O oxidation pathway in formation of $\cdot OH_{free}$. Accordingly, these results demonstrate a low contribution (<5%) of dissolved O_2 in $\cdot OH_{free}$ formation, which can be interpreted in terms of the differences between the h^+_{VB}- and e^-_{CB}-mediated mechanisms.

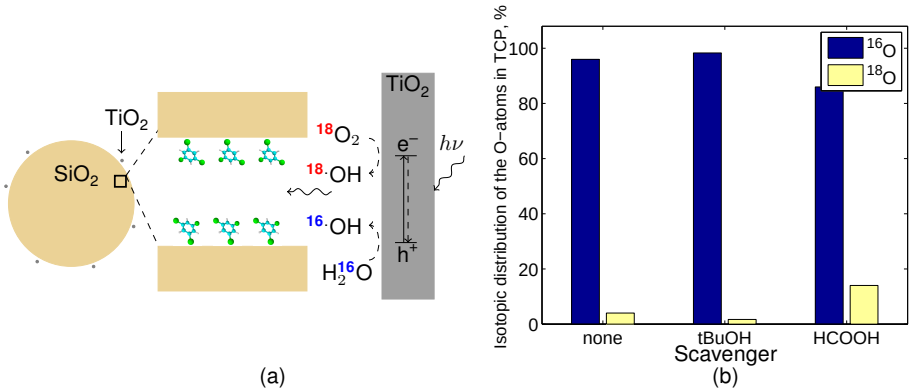

Figure 4.2: Scheme of remote photocatalytic oxidation of TCB in the SG pores (a) and influence of different scavengers on the O-atom incorporation in photocatalytically generated $\cdot OH_{free}$ (b).

Particularly, formation of $\cdot OH_{free}$ via e^-_{CB}-mediated reduction of dissolved O_2 can become more important when h^+_{VB}-mediated oxidation of H_2O is suppressed by addition of HCOOH as a h^+_{VB} scavenger (Figure 4.2-b). Taken together, the presented findings demonstrate a high importance of availability of the photocatalyst surface for h^+_{VB}-mediated oxidation of H_2O for $\cdot OH_{free}$ generation.

4.3 Degradation of BPA and its Analogues by NOM-Sensitized Photolysis

BPA ban has resulted in environmental spread of the other, non-regulated BPs, such as BPF, BPS and BPAF [7, 58]. Toxicological studies have shown that BPF and BPAF could possess toxicity, genotoxicity and estrogenic activity, similar to those of BPA, whereas BPS is supposed to be less harmful [196]. Photolysis in presence of NOM has recently been found to be one of the most important natural transformation pathways of BPA, whose rates may be comparable with the biodegradation rates [17, 19]. Unfortunately, the knowledge on the kinetic rates, mechanisms and primary intermediates of photolysis of BPA, BPF, BPS and BPAF currently remains scarce.

In the presented work, HO24 gained from the boggy lake Hohloh, Black Forest, Germany, was chosen as an NOM representative for investigation of HO24-sensitized photolysis of BPA, BPF, BPS and BPAF under simulated solar light. Comparison of the rates of HO24-sensitized and direct photolysis has shown that BPA, BPF and BPS are photolabile, whereas BPAF can be degraded in presence of NOM only. Presence of Fe^{3+}, NO_3^- and HCO_3^- at concentrations, typical for surface waters, did not influence the HO24-sensitized photolysis rates for all the BPs investigated. Radical scavenger experiments with iPrOH have suggested predominance of the ·OH-driven degradation pathway. Implication of an accurate mass HPLC-MS-MS/TOF analysis has revealed formation of catecholic intermediates and suggested the hydroxylation upon ·OH-attack to be the primary BPs degradation pathway. A moderate solvent KIE achieved by replacement of H_2O to D_2O has ruled out the contribution of the $^1O_2$-driven mechanism. Finally, the KIE of dissolved $^{18}O_2$ and the results on $D_2O/^{18}O_2$ isotopic labeling experiments have suggested that ·OH could directly originate from the excited HO24 transients (Figure 4.3).

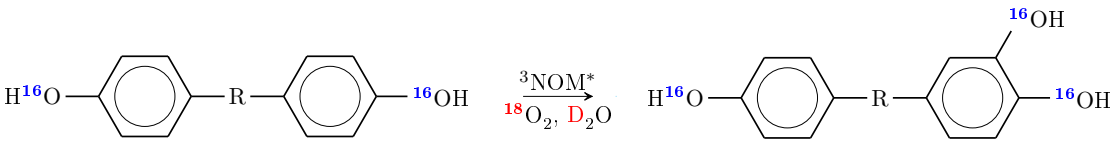

Figure 4.3: Proposed reaction of ·OH with BPs to form BPs' catechol in degradation by HO24-sensitized photolysis.

In summary, we can state that degradation by HO24-sensitized photolysis is an impor-

tant natural BPs transformation pathway, whose rates can be greater than, or at least equal to, the rates of biodegradation.

4.4 Suggestions for Future Work

In the presented study, genotoxic BPAQ and other potentially hazardous quinone-like intermediates were detected among the products of h^+_{VB}-mediated photocatalytic oxidation of BPA. By now, only a few biological studies supply limited information on BPAQ occurrence, and the data on the toxicity of the quinone/catechol-like BPA intermediates are scarce. Therefore, further toxicological research on these compounds together with a reliable quantification based on the use of authentic standards are strongly recommended.

The results on predominance of the H_2O oxidation pathway of the $\cdot OH_{free}$ generation suggest that more attention should be payed to a development of TiO_2 surfaces, which can be selectively accessed by H_2O and O_2 in order to drive the process exclusively via $\cdot OH_{free}$. Since $\cdot OH_{free}$ are as reactive as h^+_{VB}, but are much more mobile, a process, purely driven by $\cdot OH_{free}$, can open new improvement opportunities for photocatalytic treatment.

The results of the KIEs experiments suggest that $\cdot$OH generation can be directly dependent on the lifetimes of the $^3HO24^*$ transients. Additional photolysis experiments with a broader range of natural sensitizers and quenchers will help to predict environmental degradation rates of BPs. Further research on the environmental fate of BPs and the assessment of the related risks should also include toxicological studies of the BPs' catechols identified here.

5 Zusammenfassung

Konventionelle Abwasserbehandlungen sind nicht immer im Stande, endokrine Disruptoren wie BPs bis unter die PNEC Grenze abzubauen; trotzdem gibt es bis heute keine gesetzlichen BPs-Emissionsgrenzen. Aus dieser Perspektive behandelt die vorliegende Arbeit die Eignung der TiO_2-Photokatalyse, der UV-Photolyse und der HO24-sensibilisierten Photolyse zum Abbau von BPA, BPF, BPS und BPAF. Besonderes Augenmerk wird auf die Rolle spezifischer Reaktanden, wie ·OH, h^+_{VB} und $^1O_2$, im Abbauprozess gelegt.

UV Photolyse zeigte sich als zuverlässige Methode zum BPA-Abbau, jedoch nicht zu seiner Mineralisierung. TiO_2-Photokatalyse könnte hingegen eine schnelle BPA-Mineralisierung realisieren. Jedoch haben HPLC-MS-MS/ToF-Untersuchungen des BPA-Abbaumechanismusses gezeigt, dass die Photokatalyse zur Bildung potentiell genotoxischer BPA-Chinone oder weniger schädlichen BPA-Catechole führen kann, während bei der Photolyse ausschließlich BPA-Catechole entstehen. Experimente mit tBuOH als Radikalfänger bewiesen, dass die BPA-Chinone sich als Produkte der direkten h^+_{VB}-Oxidation von BPA-Catechole an der TiO_2-Oberfläche bilden.

Kinetische Untersuchungen der TiO_2-Photokatalyse mit nanoporösem SG-Träger ergaben eine hohe Quantenausbeute ($\Phi = 0.045$) der $\cdot OH_{free}$-Erzeugung. Ergebnisse der Isotopenmarkierung mit $^{18}O_2$ gaben Hinweise darauf, dass die direkte h^+_{VB}-Oxidation von H_2O den primären Reaktionsverlauf der $\cdot OH_{free}$-Bildung bestimmt. Die geringe (<5%) Einbindung von gelöstem $^{18}O_2$ in die gebildeten $\cdot OH_{free}$ wird wesentlich deutlicher (bis zu 20%), wenn die direkte H_2O-Oxidation durch Zugabe von HCOOH (als h^+_{VB}-Fänger) unterdrückt wird.

Der Abbau von BPs durch die HO24-sensibilisierte Photolyse zeigte sich als potentiell wichtiger Abbauweg, dessen Umsatzsrate größer oder gleich der des biologischen Abbaus sein kann. Vergleichsuntersuchungen der direkten Photolyse ergaben, dass BPA, BPF und BPS sich photolabil unter simuliertem Sonnenlicht verhalten, während BPAF nur unter Anwesenheit von HO24 abgebaut werden kann. HPLC-MS-MS/ToF-Ergebnisse zur Bildung von Catechol-Zwischenprodukten zusammen mit den Resultaten der Experimente mit ·OH-Radikalfänger lassen auf die Dominanz des ·OH-getriebenen BPs-Abbaus schließen. Der $^1O_2$-getriebenen Mechanismus konnte durch einen moderaten KIE des D_2O als Lösemittel ausgeschlossen werden. Der KIE des gelösten $^{18}O_2$ und die Ergebnisse der Versuche mit $D_2O/^{18}O_2$-Isotopenmarkierung deuteten an, dass die ·OH-Radikale direkt aus der angeregten HO24-Moleküle entstehen können.

Zusammenfassend lässt sich feststellen, dass sowohl die TiO_2-Photokatalyse als auch die HO24-sensibilisierte Photolyse ein hohes Potential zur Entfernung von BPs haben.

6 Experimental Section

6.1 Chemicals

6.1.1 Reagents and Solvents

All chemicals listed in Table 6.1 were used as received, except of those, which are marked by an asterisk. Further details on these additionally prepared reagents are given in section 6.3.

Table 6.1: List of reagents and solvents used in the study.

Compound	CAS Number	Grade	Supplier
Acetic acid	64-19-7	$\geq$ 99.9%	VWR
Acetone	67-64-1	99%	VWR
Acetonitrile	75-05-8	99%	VWR
Acetylacetone	123-54-6	99.5%	Fluka
Bisphenol A	80-05-7	$\geq$99%	Aldrich
Bisphenol AF	1478-61-1	97%	Aldrich
Bisphenol F	620-92-8	98%	Aldrich
Bisphenol S	80-09-1	98%	Aldrich
Dichloromethane	75-09-2	99.9%	Merck
Disodium phosphate	7558-79-4	p.a.	Merck
Formaldehyde	50-00-0	IC standard	Fluka
Formic acid	64-18-6	IC standard	Fluka
Helium	7440-59-7	99.9995%	Linde
HO24*			
Hydrogen peroxide	7722-84-1	p.a.	Fluka
Iron (II) perchlorate	335159-18-7	p.a.	Merck
Methanol	67-56-1	p.a.	Fluka

Sodium acetate	127-09-3	p.a.	Merck
Oxygen-18	32767-18-3	99%	Aldrich
Phenylglyoxilic acid	611-73-4	≥98%	Fluka
Potassium dihydrogenphosphate	7778-77-0	p.a.	Merck
Silica gel*	112926-00-8	for HPLC	Fluka
Silver nitrate	7761-88-8	p.a.	Merck
Synthetic air		≥99%	Linde
tert-Butanol*	75-65-0	99.5%	VWR
Titanium (IV) dioxide*	13463-67-7	≥95%	Aldrich
1,3,5-trichlorobenzene	108-70-3	p.a.	Aldrich
Uridine	58-96-8	≥99%	Sigma

6.1.2 Titanium Dioxide

TiO_2 powder AEROXIDE P25 (former Degussa P25) was obtained from Evonik Industries AG, Germany. The key physicochemical characteristics of P25 are summarized in Table 6.2 and illustrated by the electron micrographs in Figure 6.1. P25 is a highly crystalline nanosized mixed-phase photocatalyst with a band gap width corresponding to ca. 390 nm absorption edge [242]. The TEM micrograph in Figure 6.1-a shows a rather broad size distribution of single P25 particles. Although BET surface area of the bulk P25 is large, efficiency of P25 dispergation in water is limited by agglomeration. At pH 7, P25 forms highly polydisperse suspensions with an average particle size of ca. 1000 nm (Figure 6.1-b). Under typical photocatalytic treatment conditions ($\rho(TiO_2)$ between 0.1 and 1 g L^{-1}, ionic strength I between 0.01 and 0.1 M), TiO_2 suspensions are highly polydisperse and pH variations in the range between 5 and 8 does not strongly influence the average agglomerates size, but the zeta potential (ZP), and therefore the TiO_2 adsorption properties can vary significantly [243].

Table 6.2: Key characteristics of TiO_2 P25 particles [233, 243, 244].

Characteristics	Value
Crystal structure	ca. 75% anatase and 25% rutile
Average band gap width at 300 K	3.2 eV
BET surface area	50 ± 15 m^2 g^{-1}
Average particle diameter (TEM)	25 nm
pH of point of zero charge	6.3
Average agglomerate size at pH 7	1000 ± 500 nm

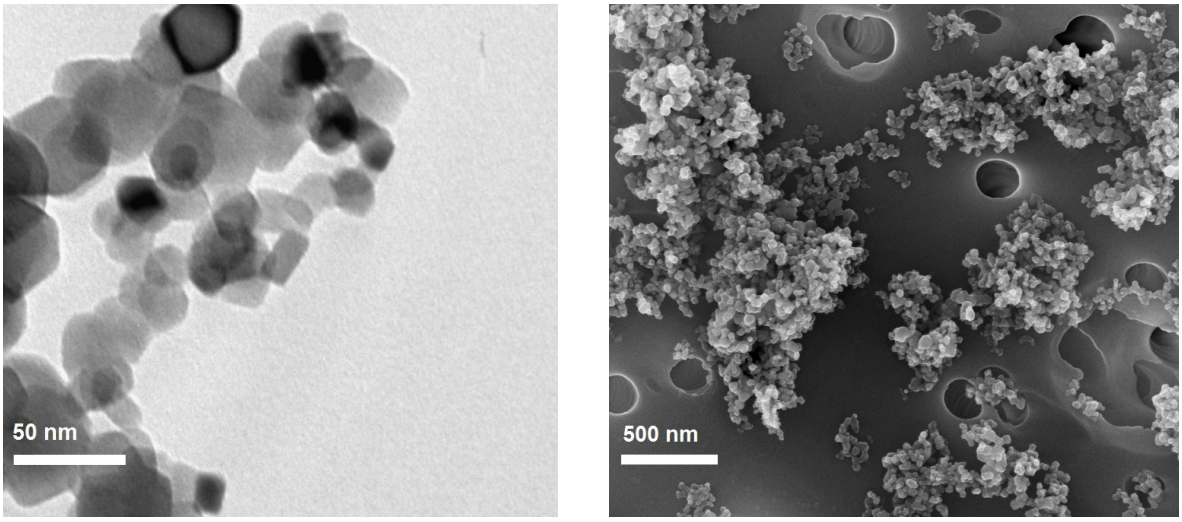

(a) (b)

Figure 6.1: Electron micrographs of TiO_2 P25 particles, re-dispersed on a carbon greed from AcN (a), and TiO_2 P25 agglomerates filtered out from water at pH 7 (b). The details on the measurement conditions are given in subsection 6.2.6.

6.1.3 NOM Sample

Here, NOM is represented by organic matter isolated from the brown water of the Hohloh Lake, Black Forest, Germany (for the details on isolation procedure see [16]). The lake Hohloh water is a boggy water with a high content of humic substances and low content of salts and anthropogenic impurities (Table 6.3). Over a 20 years period the Hohloh Lake water has had sufficiently constant characteristics [245]. The NOM sample used in this study was the 24th sample in a series and was therefore marked by the code HO24.

Aqueous HO24 solutions were prepared by dilution of the HO24 sample, preliminarily filtered through a 0.45 µm cellulose acetate filters.

Table 6.3: Key characteristics of the HO24 NOM sample.

DOC	26.1 mg(C) L^{-1}
Spectral absorption coefficient A (254 nm)	122.15 m^{-1}
pH	4.0
Electrical Conductivity (20 °C)	38.3 µS cm^{-1}
Cl^-	1.45 mg L^{-1}
SO_4^{2-}	1.29 mg L^{-1}
NO_3^-	0.92 mg L^{-1}
Ca	0.425 mg L^{-1}
Na	0.418 mg L^{-1}
Fe	0.310 mg L^{-1}
Si	0.204 mg L^{-1}
K	0.186 mg L^{-1}
Mg	0.143 mg L^{-1}
Al	0.113 mg L^{-1}
Zn	0.086 mg L^{-1}
Cu	0.012 mg L^{-1}
Mn	0.010 mg L^{-1}
Ba	0.003 mg L^{-1}
Pb	<0.015 mg L^{-1}
Sr	<0.010 mg L^{-1}
Co	<0.005 mg L^{-1}
Ni	<0.005 mg L^{-1}
P	<0.02 mg L^{-1}
Cr	<0.002 mg L^{-1}
Ti	<0.002 mg L^{-1}

6.2 Analytical Methods

6.2.1 Actinometry

Intensity of monochromatic 254 nm light generated by a low-pressure Hg lamp was measured by uridine actinometry [246]. Intensity of polychromatic UVA light generated by a solar simulator was determined by phenylglyoxylic acid actinometer [247, 248].

6.2.2 Carbon Dioxide Measurements

Concentration of CO_2, formed during the degradation experiments, was measured in the gas, leaving the tubular UV reactor, by an infrared CO_2-detector Ultramat 5 (Siemens, Germany). To provide an appropriate baseline detector response, CO_2-free synthetic air was used for the aeration. We assumed a complete CO_2 degassing of the highly aerated solution. The gas samples were taken using a gas-tight syringe.

In order to estimate efficiency of mineralization, CO_2 concentration was measured every 2 minutes during the first 30 min of the reactions and every 5 min afterwards. The volume of gas samples was 500 µL. The samples were injected into a flow of gas-carrier (N_2) continuously passing through the CO_2-detector. The gas-carrier detector flow rate was 1 L min^{-1}. The detector was connected with a PC via a digital-to-analog converter. Momentary values of CO_2 concentration were continuously recorded. For each injection, a corresponding peak "momentary concentration vs. time" was integrated numerically, and the concentration of CO_2 in each syringe sample was calculated according to Eq. (6.1).

$$c(\mathrm{CO_2}) = \frac{u_{\mathrm{N_2}}}{V_{syr}} \int_{t_{start}}^{t_{end}} \mathrm{c}^*_{\mathrm{CO_2}}(\mathrm{t})\,\mathrm{d}t \tag{6.1}$$

where $c(CO_2)$ is the concentration of CO_2 in the gas sample (M); u_{N_2} is the flow rate of the gas-carrier (L s^{-1}); V_{syr} is the volume of the syringe; $c^*_{CO_2}(t)$ is momentary concentration of CO_2 in the detector; t_{start} and t_{end} correspond to the start and the end of each peak.

Then, the total amount of generated CO_2 was calculated according to Eq. (6.2).

$$n_{t_i} = u_{aer} \int_0^{t_i} \mathrm{c}(\mathrm{CO_2})\,\mathrm{d}t \tag{6.2}$$

where n_{t_i} is the amount of CO_2 accumulated up to time t_i; u_{aer} is the flow rate of synthetic air used for the reactor aeration.

6.2.3 High Performance Liquid Chromatography with Ultraviolet (HPLC-UV) and Tandem Mass-Spectrometric Time of Flight (HPLC-MS-MS/ToF) Detection

A HPLC chromatograph Agilent 1100 with a Diode Array Detector (Agilent Technologies, Waldbronn, Germany) was used for the HPLC-UV measurements. HPLC-MS-ToF measurements were conducted using an Agilent 1290 HPLC system coupled with a 6540 UHD Q-ToF mass spectrometer (Agilent Technologies, Waldbronn, Germany) operated in the negative ionization mode.

HPLC-MS-MS measurements were performed using the HPLC chromatograph Agilent 1100 coupled with a triple quadrupole mass-spectrometric detector Applied Biosystems 3000 (MDS Sciex Instruments, Concord, ON, Canada). MS-MS fragmentation was carried out at -30 eV and -60 eV in negative ionization mode. All HPLC measurements were conducted using a 125-4 mm LiChrospher C-18 5 µm column (Merck Milipore, Schwalbach, Germany). Structures of detected intermediates were proposed according to the comparison of the estimated and experimentally measured logarithms of octanol-water partition coefficients ($\log P$). The estimations were done according to the principle of isolating carbons [249]. Analysis of all the HPLC-MS data obtained was performed using the "ACD Spectrus Processor" software.

6.2.4 Size Exclusion Chromatography (SEC) and DOC Analysis

SEC chromatograms were recorded using the SEC system described in detail elsewhere [233, 250]. In short, the samples of 2 mL volume were injected in an aqueous phosphate eluent flowing through a 250-20 mm Novogrom column (Alltech Grom, Germany) packed with a Toyopearl HW 50S resin (Tosoh Corp., Japan) at a flow rate of 1 mL min^{-1}. Quantification of DOC was performed on the basis of the infrared detection of the CO_2 formed by a photochemical oxidation of the sample in a rotating thin-film reactor [250]. DOC measurements were performed by a wet chemical method using a Sievers TOC Analyzer 820 (Sievers Instruments, Boulder, USA). All the SEC and DOC samples were preliminarily filtered through a 0.45 µm cellulose acetate filters.

6.2.5 Correlation between log*P* and HPLC Retention Time

To establish a correlation between HPLC retention times and $\log P$ coefficients, three compounds with known $\log P$ values were used as calibration standards. Their properties

Table 6.4: The standards and parameters of the log P–RT calibration.

Standard compound	log P_{calc}	log P_{exp}	RT, min	R^2
2-(3-Hydroxyphenyl)acetic acid	0.77 ± 0.22	0.85 [251]	7.1 ± 0.2	0.9987
4-Hydroxybenzaldehyde	1.39 ± 0.26	1.38 [251]	8.7 ± 0.2	
BPA	3.43 ± 0.23	3.4 [31]	13.7 ± 0.2	

are given in Table 6.4. Aqueous solutions of the standards of 50 mg L^{-1} concentration were mixed and analyzed using the HPLC-UV method under the conditions used further in all the measurements. The average values of three replicates were used for the calibration. Both experimental and calculated log P coefficients exhibited linear dependence on HPLC retention times. Thus, log P values for all the BPA intermediates were further calculated out of their retention times using the following linear calibration function:

$$\log P_{calc} = 0.39\mathrm{RT} - 1.96 \tag{6.3}$$

where RT is the HPLC retention time (min).

6.2.6 Scanning Electron Microscopy (SEM) and Transmission Electron Microscopy (TEM)

Samples for SEM and TEM measurements were obtained from 0.1 g L^{-1} TiO_2 aqueous suspension by isolation of TiO_2 agglomerates on polycarbonate filters with 0.2 µm pores. After drying, the SEM samples were coated by platinum using sputter deposition in order to avoid distortion due to a charging effect. The coating was done in the laboratory of electron microscopy of KIT. SEM was conducted on a Leo Gemini 1530 (Zeiss, Jena, Germany) electron microscope operated at an acceleration voltage of 2 keV. TEM micrographs were obtained using a Philips CM200-FEG (Philips, Amsterdam, The Netherlands) electron microscope operated at 200 keV acceleration voltage.

6.2.7 Gas Chromatography-Mass-Spectrometry (GC-MS)

GC-MS analysis was carried out using a gas chromatograph Agilent 7890A equipped with a split/splitless injector, a mass spectrometer Agilent 5975 and an analytical column HP-5MS 30 m×0.32 mm×0.25 µm (Agilent Technologies, Waldbronn, Germany). The samples of 1 µl volume were injected in the injector in a splitless mode at 200 °C. The flow rate of the carrier gas (He) was 1.6 mL min^{-1}. The GC oven temperature was kept at

45 °C for 3 min, then ramped to 240 °C at the rate of 20 °C min^{-1} and held at 240 °C for 4 min. The temperatures of the ion source and the MS interface were 250 °C and 230 °C, respectively. Mass spectra were obtained in an electron impact ionization mode at 70 eV. The MS fragments at m/z of 145 and 196 were used for quantification of TCB and TCP, respectively.

6.2.8 Dispersive Liquid Microextraction (DLME)

In the experiments on remote photocatalysis (section 3.2), a DLME method was adopted for one-step extraction and preconcentration of TCB and its degradation product, TCP. For this purpose, 5 mL aqueous suspension samples each containing 0.15 mg of TCB retained on 20 mg of SiO_2 were extracted by a cloudy solution formed of dichloromethane (DCM). The cloudy solution was formed by injection of a mixture of DCM with acetone as a dispersing solvent. The acetone-DCM ratio was varied tin order to estimate the DLME performance and to compare it with conventional liquid-liquid extraction (LLE) by 1 ml of DCM. The results for relative standard deviation (RSD) and extraction recovery are given in Table 6.5. The values of acetone-DCM volume ratios are given in brackets.

Table 6.5: Comparison of TCB GC-MS signal intensity, RSD values and extraction recovery of the developed DLME procedure related to the conventional LLE method.

Method	TCB GC-MS peak area	Recovery, % (N = 3)	RSD, %
DLME (10:1)	2.0e7	20.5	8.1
DLME (5:1)	1.6e7	32.3	4.9
DLME (2:1)	1.0e7	51.5	3.0
LLE (0:1)	0.7e7	72.0	2.4

On the comparison of the data presented in Table 6.5, we chosen 5:1 acetone-DCM ratio for further experiments.

6.2.9 Dynamic Light Scattering (DLS)

To ensure the TiO_2 suspension stability during photocatalytic processes (section 3.1), ZP of TiO_2 particles was monitored by laser Doppler micro-electrophoresis using a Zetasizer Nano ZS analyzer (Malvern Instruments Ltd, Malvern, UK). Before the ZP measurements, the ionic strength of the samples was increased by addition of several NaCl crystals and the samples were incubated in the analyzer cell at 20 °C for 1 min.

6.3 Equipment and Procedures

6.3.1 Tubular UV Reactor

The experiments on BPA degradation were conducted in a 200 mL reactor filled with 180 mL solution and equipped with a coaxial quartz tube, pH-electrode, aeration dispenser outlets and outlet for CO_2 sampling (Figure 6.2).

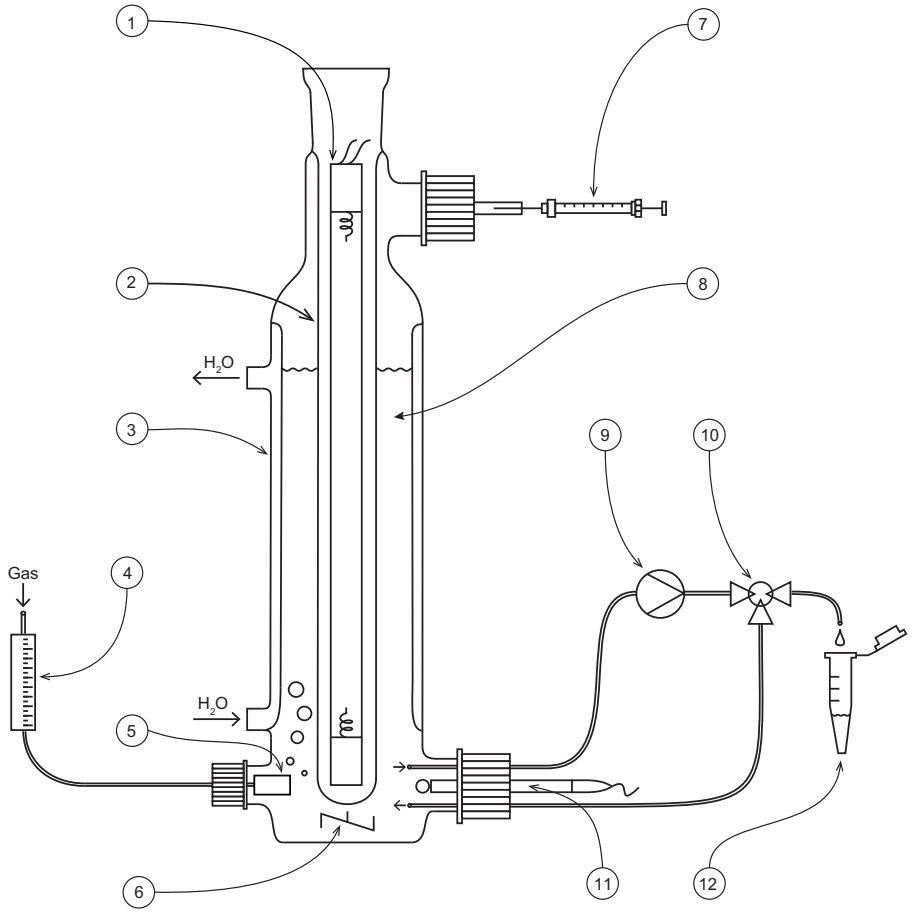

Figure 6.2: Tubular UV reactor used for BPA degradation. (1) UV lamp; (2) quartz tube; (3) thermostating jacket; (4) gas flow meter; (5) gas diffuser; (6) magnetic stirrer; (7) gas-tight syringe for CO_2-sampling; (8) BPA solution; (9) sampling pump with capillary tubes; (10) sampling valve; (11) pH electrode; (12) sampling tube.

An aluminum dispenser connected to a gas tank through a flow controller was used to aerate the solution. The aeration flow was adjusted to 0.21 L min-1 and remained constant in all experiments. A static temperature regime was maintained by thermostated cooling water running through the outer jacket of the reactor. All experiments were run with magnetic stirring. The quartz tube and the UV lamp were cooled by the air flow of room

temperature. The low-pressure ozone-free Hg lamp (UVI 40 4C, UV-Technik Meyer, Ortenberg, Germany), made of doped quartz to cut off the Hg VUV line at λ=184.9 nm, had a monochromatic spectrum at λ=254 nm and 4 µE s^{-1} irradiance measured by uridine actinometry. The UV lamp was turned on for 30 min before every experiment to reach the thermal equilibrium. Stability of the UV intensity was checked with a digital UV radiometer (Epigap Optronic GmbH, Germany) according to [252].

The TiO_2 load was 0.1 mg L^{-1} in all experiments, since this value was previously reported to be the most optimal one in terms of the efficiency of light absorption and catalyst demand [190, 253, 254]. Before the photocatalytic experiments, organic impurities of the TiO_2 surface were removed by 12 h calcination at 300 °C. After 30 min of sonication in a ultrasonic bath for dispergation, the aliquot of BPA solution was added to the photocatalyst suspension. The mixture was kept in the dark for 30 min to reach adsorption equilibrium [255]. The initial BPA concentration of 220 µM was chosen to maximize the coverage of the photocatalyst surface by BPA molecules [256]. Typically, in aqueous media, BPA exists in unionized form ($pK_{a\text{-}I}$ = 9.6, $pK_{a\text{-}II}$ = 10.2 [31]) and pH has only a small effect on BPA adsorption on TiO_2 [205]. Therefore, the media was not buffered, but the pH was monitored throughout the experiments. As a result, the pH varied between 4.7 and 6.7 with the initial pH value of 6.7. Conditions for all the photolytic and photocatalytic experiments were identical.

A peristaltic pump continuously pumped the suspension through the capillary tube cycle. To take a sample for HPLC-MS measurements the cycling was interrupted with a valve, and 1 mL of the suspension flow was directed to a sampling tube. In photocatalytic experiments, the samples were centrifuged before analysis to separate the TiO_2 suspension. The effect of tBuOH (54 mM), a scavenger of $\cdot OH_{free}$, on the rates of UV photolysis and photocatalysis was estimated by conducting three replicates. In these experiments, double-distilled tBuOH was used.

6.3.2 Solar Simulator

A solar simulator Oriel Sol 3A (Newport Corp., Stratford, CT, USA) was used as source of a spatially uniform field of UVA light for the experiments on remote photocatalysis and sensitized photolysis (Figure 6.3). The samples were placed in a water bath filled with circulating water, which was thermostated at 20 °C. In order to prevent sedimentation of TiO_2 and SiO_2 particles, the samples were rigorously mixed via magnetic stirring. The sample volume was varied, but irradiation pathlength was kept constant at 4 cm. The samples were covered by a filter WG 295 from Schott AG, Germany, in order to cut-off

irradiation below 295 nm. The UVA light intensity determined by phenylglyoxylic acid actinometry was 5 µE s^{-1} in all the positions of the sample box.

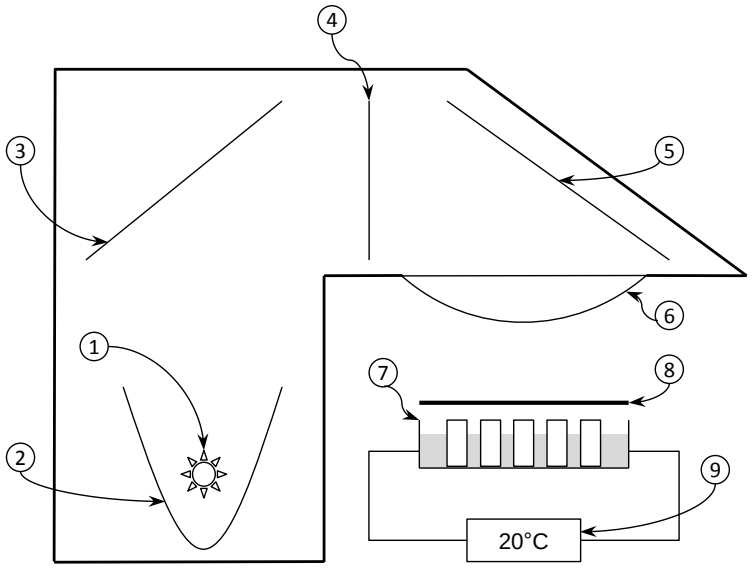

Figure 6.3: Scheme of the solar simulator. (1) 1 kW Xe lamp; (2) ellipsoidal reflector; (3) mirror; (4) atmosphere attenuation filter; (5) mirror; (6) collimating lens; (7) sample box; (8) 295 nm cut-off filter; (9) thermostate.

The TiO_2 load was 0.1 mg L^{-1}. Before each experiment, TiO_2 suspension was sonicated during 30 min, then mixed with a probe compound and scavenger. The mixture was kept in the dark for 30 min to reach adsorption equilibrium. The initial concentration of the probe compound, 1,3,5-trichlorobenzene (TCB), in aqueous solutions was 33 µM, which corresponded to the TCB water solubility [257]. In the experiments with TCB adsorbed in the SG pores, the SG load was 20 mg per 5 mL of the overall sample volume, which corresponded to a 165 µM TCB concentration. The SG load of 20 mg corresponded to the minimal TCB amount, which could be measured with a minimal error of the sample preparation.

6.3.3 Adsorption in the SG Pores

1,3,5-trichlorobenzene (TCB) was used as a probe compound in the remote photocatalysis experiments (section 3.2). TCB was evaporated from a solid in a gas-tight flask thermostated at 80 °C in the GC oven and then continuously purged by a 2 ml min^{-1} He

flow to a SiO_2-column set for adsorption. The SiO_2-column was packed with mesoporous SG of high-purity grade was obtained from Fluka, Germany. Its main properties are given in (Table 6.6). The adsorption rate was monitored by MS detection at m/z of 145 (Figure 6.5). The MS parameters were identical to those, set in all GC-MS measurements.

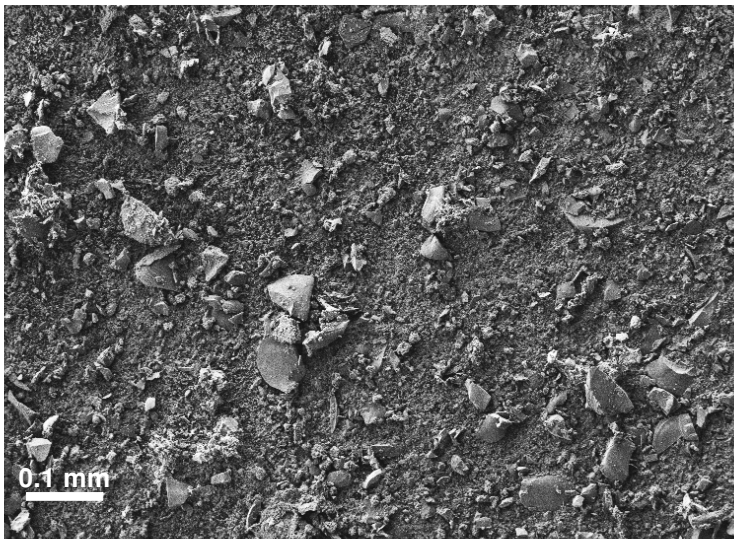

Figure 6.4: SEM micrographs of a SG and P25 particles mixture after 6 h of photocatalytic reaction. The details on the measurement conditions are given in subsection 6.2.6.

The TCB MS signal obtained with an empty column was used as a reference for completion of the TCB adsorption. Once the TCB breakthrough was observed on the same level as for the empty column reference, the adsorption process was terminated. In order to estimate the maximum mass of TCB adsorbed (q_{max}), several enriched SG samples were eluted with dichloromethane and q_{max} was found to be 0.149 g g^{-1}. Then, amounts of TCB adsorbed at given time were calculated from a ratio between the momentary and maximum values of MS signals:

$$n_{ads} = \frac{q_{max} m_{\mathrm{SG}}}{M_{\mathrm{TCB}}} \frac{I_t}{I_{max}} \tag{6.4}$$

where n_{ads} is amount of TCB adsorbed (mol) at time t; q_{max} is the maximum mass of TCB adsorbed (g g^{-1}); m_{SG} is the mass of the SG phase; M_{TCB} is the TCB molar mass (g mol^{-1}); I_t and I_{max} are momentary and maximal TCB signals of MS detector at m/z of 145, respectively.

Table 6.6: Main characteristics of the SG phase used in the study.

Characteristic	Value
Particle size (d), µm	10 - 60
Density (ρ_{SG}), g mL^{-1}	1.39
Pore size, nm	4 [258]
BET surface area, m^2 g^{-1}	460 [258]

Obtained isotherm of TCB adsorption was then analyzed by means of the BET method:

$$\frac{1}{n_{ads}(p_0/p-1)} = \frac{1}{n_m C} + \frac{C-1}{n_m C}\frac{p}{p_0} \tag{6.5}$$

where n_{ads} is amount of TCB adsorbed (mol); p_0/p is a reciprocal of a relative TCB pressure taken as I_{max}/I_t value; n_m and C are TCB amount constituting a monolayer of surface coverage and the BET constant, respectively.

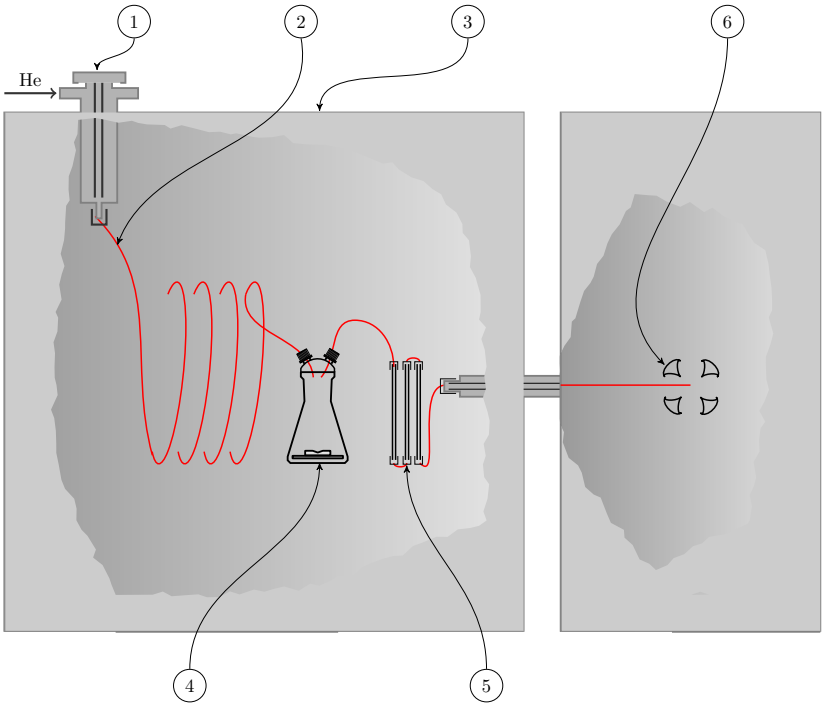

Figure 6.5: GC-MS setup developed for monitoring of the TCB adsorption in the SiO_2 pores.(1) GC inlet with flow controller; (2) 5 m×0.32 mm deactivated silica capillary; (3) GC oven;(4) gas-tight flask with solid TCB sample; (5) SiO_2 particles packed in multiple columns; (6) quadrupole mass-analyzer.

6.3.4 Isotopic Labeling Experiments

In the experiments with isotopically labeled O_2, TiO_2 suspensions enriched with $^{18}O_2$ were prepared in a pressurized cell depicted in Figure 6.6. Before each experiment, 0.2 L of TiO_2 suspension was subjected to multiple evacuation cycles by a vacuum pump with subsequent He purging until dissolved $^{16}O_2$ was completely replaced. Then, the solution was exposed to 1 atm of $^{18}O_2$ under vigorous magnetic stirring until its concentration reached 8 mg L^{-1}. An O_2-microsensor Unisense (Unisense A/S, Aarhus N, Denmark) was used to monitor the overall O_2 concentration. $^{18}O_2$-enriched samples were taken via a sampling port without opening the cell by 5 ml gas-tight syringes, which were immediately closed by plugs after sampling. Finally, 5 mL vials were filled with $^{18}O_2$-saturated solutions in a glovebox under a nitrogen atmosphere with an approximate $^{16}O_2$ content of 40 ppm and closed. The samples were isolated from the atmosphere by a quartz plate with the sealed membrane caps glued on.

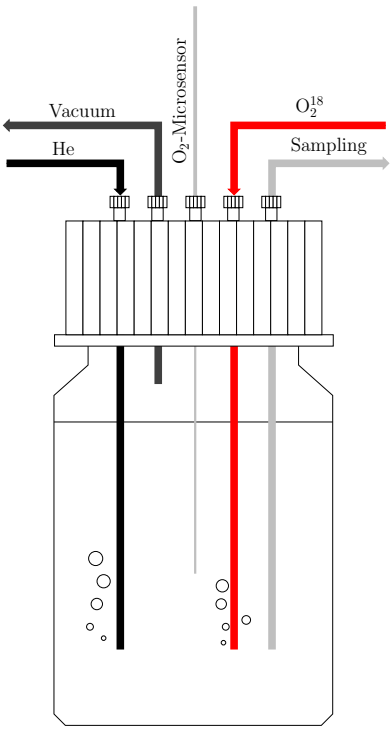

Figure 6.6: The pressurized cell for preparation of TiO_2 suspensions enriched with $^{18}O_2$. The suspension and the headspace volumes were 0.2 L and 0.05 L, repectively.

List of Abbreviations and Symbols

AOPs	advanced oxidation processes
BPs	bisphenols
BPA	bisphenol A
BPAF	bisphenol AF
BPAQ	bisphenol A quinone
BPF	bisphenol F
BPS	bisphenol S
CB	conduction band
DCM	dichloromethane
DFT	density functional theory
DLME	dispersive liquied microextraction
DLS	dynamic light scattering
DOC	dissolved organic carbon
EDCs	endocrine disruptive compounds
e^-_{CB}	conduction band electron
GC	gas chromatography
HO24	Hohloh Lake NOM sample
h^+_{VB}	valence band hole
HPLC	high performance liquid chromatography
IC	internal conversion
iPrOH	isopropanol
ISC	inter-system crossing
L-H	Lanmuir–Hinshelwood formalism
LLE	liquid-liquid extraction
MRM	multiple reaction monitoring
MS	mass spectrometry
MS-MS	tandem mass spectrometry
NOM	natural organic matter

$\cdot OH_{free}$	free hydroxyl radical
$\cdot OH_{free}$	surface-bound hydroxyl radical
PCs	polycarbonates
PNEC	predicted no effect concentration
ROS	reactive oxygen species
RSD	relative standard deviation
SEC	size exclusion chromatography
SEM	scanning electron microscopy
SG	silica gel
STM	scanning tunneling microscopy
tBuOH	tert-butanol
TCB	1,3,5-trichlorobenzene
TCP	2,4,6-trichlorophenol
TEM	transition electron microscopy
TOC	total organic carbon
ToF	time of flight mass spectrometry
US EPA	United States Environmental Protection Agency
UV	ultraviolet
VB	valence band
VUV	vacuum ultraviolet
ZP	zeta potential

Bibliography

(1) Merchant Research & Consulting Bisphenol A (BPA): World Market Outlook and Forecast up to 2018., 2014.

(2) Flint, S.; Markle, T.; Thompson, S.; Wallace, E. *Journal of Environmental Management* **2012**, *104*, 19–34.

(3) Liao, C.; Liu, F.; Moon, H.-B.; Yamashita, N.; Yun, S.; Kannan, K. *Environmental Science & Technology* **2012**, *46*, 11558–11565.

(4) Song, S.; Song, M.; Zeng, L.; Wang, T.; Liu, R.; Ruan, T.; Jiang, G. *Environmental Pollution* **2014**, *186*, 14–19.

(5) Liao, C.; Liu, F.; Guo, Y.; Moon, H.-B.; Nakata, H.; Wu, Q.; Kannan, K. *Environmental Science & Technology* **2012**, *46*, 9138–9145.

(6) Liao, C.; Liu, F.; Kannan, K. *Environmental Science & Technology* **2012**, *46*, 6515–6522.

(7) Liao, C.; Kannan, K. *Journal of Agricultural and Food Chemistry* **2013**, *61*, 4655–4662.

(8) Song, S. J.; Ruan, T.; Wang, T.; Liu, R. Z.; Jiang, G. B. *Environmental Science & Technology* **2012**, *46*, 13136–13143.

(9) Kisch, H. *Angewandte Chemie International Edition* **2013**, *52*, 812–847.

(10) Linsebigler, A. L.; Lu, G.; Yates, J. T. *Chemical Reviews* **1995**, *95*, 735–758.

(11) Fox, M. A.; Dulay, M. T. *Chemical Reviews* **1993**, *93*, 341–357.

(12) Ohtani, B. *Journal of Photochemistry and Photobiology C: Photochemistry Reviews* **2010**, *11*, 157–178.

(13) Ohtani, B. *Physical Chemistry Chemical Physics* **2014**, *16*, 1788–1797.

(14) Sun, Y.; Pignatello, J. J. *Environmental Science & Technology* **1995**, *29*, 2065–2072.

(15) Henderson, M. A. *Surface Science Reports* **2011**, *66*, 185–297.

(16) Frimmel, F. H.; Abbt-Braun, G.; Heumann, K. G.; Hock, B.; Luedemann, H. D.; Spiteller, M., *Refractory organic substances in the environment*; Wiley-VCH: 2002.

(17) Zhan, M.; Yang, X.; Xian, Q.; Kong, L. *Chemosphere* **2006**, *63*, 378–386.

(18) Barbieri, Y.; Massad, W. A.; Diaz, D. J.; Sanz, J.; Amat-Guerri, F.; Garcia, N. A. *Chemosphere* **2008**, *73*, 564–571.

(19) Chin, Y.-P.; Miller, P. L.; Zeng, L.; Cawley, K.; Weavers, L. K. *Environmental Science & Technology* **2004**, *38*, 5888–5894.

(20) Fukazawa, H.; Watanabe, M.; Shiraishi, F.; Shiraishi, H.; Shiozawa, T.; Matsushita, H.; Terao, Y. *Journal of Health Science* **2002**, *48*, 242–249.

(21) Yamamoto, T.; Yasuhara, A.; Shiraishi, H.; Nakasugi, O. *Chemosphere* **2001**, *42*, 415–418.

(22) Azevedo, D. d. A.; Lacorte, S.; Viana, P.; Barceló, D. *Journal of the Brazilian Chemical Society* **2001**, *12*, 532–537.

(23) Rudel, R. A.; Melly, S. J.; Geno, P. W.; Sun, G.; Brody, J. G. *Environmental Science & Technology* **1998**, *32*, 861–869.

(24) Vethaak, A. D.; Lahr, J.; Schrap, S. M.; Belfroid, A. C.; Rijs, G. B. J.; Gerritsen, A.; de Boer, J.; Bulder, A. S.; Grinwis, G. C. M.; Kuiper, R. V.; Legler, J.; Murk, T. A. J.; Peijnenburg, W.; Verhaar, H. J. M.; de Voogt, P. *Chemosphere* **2005**, *59*, 511–524.

(25) Latorre, A.; Lacorte, S.; Barcela, D. English *Chromatographia* **2003**, *57*, 111–116.

(26) Funakoshi, G.; Kasuya, S. *Chemosphere* **2009**, *75*, 491–497.

(27) Zhang, Y.; Zhou, J. L. *Chemosphere* **2008**, *73*, 848–853.

(28) Kuch, H. M.; Ballschmiter, K. *Environmental Science & Technology* **2001**, *35*, 3201–3206.

(29) Edmonds, J. S.; Nomachi, M.; Terasaki, M.; Morita, M.; Skelton, B. W.; White, A. H. *Biochemical and Biophysical Research Communications* **2004**, *319*, 556–561.

(30) Nelson, A. M.; Long, T. E. *Polymer International* **2012**, *61*, 1485–1491.

(31) Staples, C. A.; Dorn, P. B.; Klecka, G. M.; O'Block, S. T.; Harris, L. R. *Chemosphere* **1998**, *36*, 2149–2173.

(32) Chen, M. Y.; Ike, M.; Fujita, M. *Environmental Toxicology* **2002**, *17*, 80–86.

(33) Yamamoto, T.; Yasuhara, A. *Chemosphere* **1999**, *38*, 2569–2576.

(34) Kang, J.-H.; Kondo, F.; Katayama, Y. *Toxicology* **2006**, *226*, 79 –89.

(35) Geens, T.; Goeyens, L.; Covaci, A. *International Journal of Hygiene and Environmental Health* **2011**, *214*, 339 –347.

(36) Fic, A.; Zegura, B.; Sollner, M.; Metka Filipic, D.; Peterlin Masic, L. *Archives of Industrial Hygiene and Toxicology* **2013**, *64*, 189–200.

(37) Shelnutt, S.; Kind, J.; Allaben, W. *Food and Chemical Toxicology* **2013**, *57*, 284–295.

(38) EPA *Bisphenol A alternatives in thermal paper. Draft for public comment*; Report; 2014.
(39) Artham, T.; Doble, M. *Macromolecular Bioscience* **2008**, *8*, 14–24.
(40) Chun, H.; Yizhong, W.; Hongxiao, T. *Chemosphere* **2000**, *41*, 1205–1209.
(41) Cabaton, N.; Dumont, C.; Severin, I.; Perdu, E.; Zalko, D.; Cherkaoui-Malki, M.; Chagnon, M. C. *Toxicology* **2009**, *255*, 15–24.
(42) Fromme, H.; Küchler, T.; Otto, T.; Pilz, K.; Müller, J.; Wenzel, A. *Water Research* **2002**, *36*, 1429–1438.
(43) Li, Y.; Burns, K. A.; Arao, Y.; Luh, C. J.; Korach, K. S. *Environmental Health Perspectives* **2012**, *120*, 1029–1035.
(44) Matsushima, A.; Liu, X.; Okada, H.; Shimohigashi, M.; Shimohigashi, Y. *Environmental Health Perspectives* **2010**, *118*, 1267–1272.
(45) Barraza, L. *The Journal of Law, Medicine & Ethics* **2013**, *41*, 9–12.
(46) Dodds, E. C.; Lawson, W. *Nature* **1936**, *137*, 996.
(47) Morrissey, R. E.; George, J. D.; Price, C. J.; Tyl, R. W.; Marr, M. C.; Kimmel, C. A. *Fundamental and Applied Toxicology* **1987**, *8*, 571–582.
(48) Krishnan, A. V.; Stathis, P.; Permuth, S. F.; Tokes, L.; Feldman, D. *Endocrinology* **1993**, *132*, 2279–2286.
(49) Fuerhacker, M; Scharf, S; Weber, H *Chemosphere* **2000**, *41*, 751 –756.
(50) Wang, G. H.; Wu, F.; Zhang, X.; Luo, M. D.; Deng, N. S. *Fresenius Environmental Bulletin* **2006**, *15*, 61–67.
(51) Cao, G. P.; Lu, J. L.; Wang, G. Y. *Journal of Environmental Sciences-China* **2012**, *24*, 846–851.
(52) Liu, Y.; Zhang, X.; Wu, F. *Applied Clay Science* **2010**, *49*, 182 –186.
(53) Ike, M.; Chen, M. Y.; Danzl, E.; Sei, K.; Fujita, M. *Water Science and Technology* **2006**, *53*, 153–159.
(54) p,p′Bisphenols and Diglycidyl Ethers of p,p′Bisphenols., US EPA, Materials for November 8, 2012 Meeting of Scientific Guidance Panel (SGP), Biomonitoring California: Nov. 2012.
(55) Fu, M.; Li, Z.; Gao, H. *Chemosphere* **2007**, *69*, 1009–1016.
(56) Kawahata, H.; Ohta, H.; Inoue, M.; Suzuki, A. *Chemosphere* **2004**, *55*, 1519–1527.
(57) Fernandez, M. P.; Ikonomou, M. G.; Buchanan, I. *Science of The Total Environment* **2007**, *373*, 250–269.
(58) Liao, C.; Liu, F.; Alomirah, H.; Loi, V. D.; Mohd, M. A.; Moon, H.-B.; Nakata, H.; Kannan, K. *Environmental Science & Technology* **2012**, *46*, 6860–6866.

(59) Molina-Molina, J. M.; Amaya, E.; Grimaldi, M.; Saenz, J. M.; Real, M.; Fernandez, M. F.; Balaguer, P.; Olea, N. *Toxicology and Applied Pharmacology* **2013**, *272*, 127 –136.

(60) Feng, Y.; Yin, J.; Jiao, Z.; Shi, J.; Li, M.; Shao, B. *Toxicology Letters* **2012**, *211*, 201–209.

(61) Matsushima, A.; Kakuta, Y.; Teramoto, T.; Koshiba, T.; Liu, X.; Okada, H.; Tokunaga, T.; Kawabata, S.-i.; Kimura, M.; Shimohigashi, Y. *Journal of Biochemistry* **2007**, *142*, 517–524.

(62) Vinas, R.; Watson, C. S. *Environmental Health Perspectives* **2013**, *121*, 352–358.

(63) Rubin, B. S. *The Journal of Steroid Biochemistry and Molecular Biology* **2011**, *127*, 27–34.

(64) Takeuchi, T.; Tsutsumi, O.; Ikezuki, Y.; Takai, Y.; Taketani, Y. *Endocrine Journal* **2004**, *51*, 165–169.

(65) Witorsch, R. *Food and Chemical Toxicology* **2002**, *40*, 905 –912.

(66) Olea, N; Pazos, P; Exposito, J *European Journal of Cancer Prevention* **1998**, *7*, S17–S24.

(67) Nagel, S. C.; vom Saal, F. S.; Thayer, K. A.; Dhar, M. G.; Boechler, M.; Welshons, W. V. *Environmental Health Perspectives* **1997**, *105*, 70.

(68) Bolger, R.; Wiese, T. E.; Ervin, K.; Nestich, S.; Checovich, W. *Environmental Health Perspectives* **1998**, *106*, 551.

(69) Judy, B. M.; Nagel, S. C.; Thayer, K. A.; Vom Saal, F. S.; Welshons, W. V. *Toxicology and Industrial Health* **1999**, *15*, 12–25.

(70) Perez, P.; Pulgar, R.; Olea-Serrano, F.; Villalobos, M.; Rivas, A.; Metzler, M.; Pedraza, V.; Olea, N. *Environmental Health Perspectives* **1998**, *106*, 167–174.

(71) Vandenberg, L. N.; Hunt, P. A.; Myers, J. P.; Saal, F. S. V. *Reviews on Environmental Health* **2013**, *28*, 37–58.

(72) Chouhan, S.; Yadav, S. K.; Prakash, J.; Swati; Singh, S. P. *Annals of Microbiology* **2014**, *64*, 13–21.

(73) Rochester, J. R. *Reproductive Toxicology* **2013**, *42*, 132–155.

(74) Teeguarden, J. G.; Hanson-Drury, S. *Food and Chemical Toxicology* **2013**, *62*, 935–948.

(75) Geens, T.; Aerts, D.; Berthot, C.; Bourguignon, J.-P.; Goeyens, L.; Lecomte, P.; Maghuin-Rogister, G.; Pironnet, A.-M.; Pussemier, L.; Scippo, M.-L.; Loco, J. V.; Covaci, A. *Food and Chemical Toxicology* **2012**, *50*, 3725 –3740.

(76) Suzuki, T.; Nakagawa, Y.; Takano, I.; Yaguchi, K.; Yasuda, K. *Environmental Science & Technology* **2004**, *38*, 2389–2396.

(77) Hotchkiss, A. K.; Rider, C. V.; Blystone, C. R.; Wilson, V. S.; Hartig, P. C.; Ankley, G. T.; Foster, P. M.; Gray, C. L.; Gray, L. E. *Toxicological Sciences* **2008**, *105*, 235–259.

(78) Kwak, H.-I.; Bae, M.-O.; Lee, M.-H.; Lee, Y.-S.; Lee, B.-J.; Kang, K.-S.; Chae, C.-H.; Sung, H.-J.; Shin, J.-S.; Kim, J.-H., et al. *Environmental Toxicology and Chemistry* **2001**, *20*, 787–795.

(79) Kang, J.-H.; Aasi, D.; Katayama, Y. *CRC Critical Reviews in Toxicology* **2007**, *37*, 607–625.

(80) Vos, J. G.; Dybing, E.; Greim, H. A.; Ladefoged, O.; Lambré, C.; Tarazona, J. V.; Brandt, I.; Vethaak, A. D. *CRC Critical Reviews in Toxicology* **2000**, *30*, 71–133.

(81) Stoker, C; Rey, F; Rodriguez, H; Ramos, J.; Sirosky, P; Larriera, A; Luque, E.; Muñoz-de Toro, M *General and Comparative Endocrinology* **2003**, *133*, 287–296.

(82) Kang, I.; Yokota, H.; Oshima, Y.; Tsuruda, Y.; Oe, T.; Imada, N.; Tadokoro, H.; Honjo, T. *Environmental Toxicology and Chemistry* **2002**, *21*, 2394–2400.

(83) Oehlmann, J.; Schulte-Oehlmann, U.; Tillmann, M.; Markert, B. *Ecotoxicology* **2000**, *9*, 383–397.

(84) Sohoni, P.; Tyler, C.; Hurd, K; Caunter, J; Hetheridge, M; Williams, T; Woods, C; Evans, M; Toy, R; Gargas, M, et al. *Environmental Science & Technology* **2001**, *35*, 2917–2925.

(85) Levy, G.; Lutz, I.; Krüger, A.; Kloas, W. *Environmental Research* **2004**, *94*, 102–111.

(86) Crain, D. A.; Eriksen, M.; Iguchi, T.; Jobling, S.; Laufer, H.; LeBlanc, G. A.; Guillette Jr, L. J. *Reproductive Toxicology* **2007**, *24*, 225–239.

(87) Oehlmann, J.; Schulte-Oehlmann, U.; Bachmann, J.; Oetken, M.; Lutz, I.; Kloas, W.; Ternes, T. A. *Environmental Health Perspectives* **2006**, *114*, 127–133.

(88) Marcial, H. S.; Hagiwara, A.; Snell, T. W. *Environmental Toxicology and Chemistry* **2003**, *22*, 3025–3030.

(89) Baek, H. J.; Park, M. H.; Lee, Y. D.; Kim, H. B. *Fish Physiology and Biochemistry* **2003**, *28*, 413–414.

(90) Moller, L.; Helweg, C.; Pratt, C. H.; Worup, A.; Skak, C., *Evaluation of Alternatives for Compounds under Risk Assessment in the EU, Bisphenol A*; Danish Environmental Protection Agency: 2004.

(91) Arditsoglou, A.; Voutsa, D. *Environmental Science and Pollution Research* **2008**, *15*, 228–236.

(92) Mohapatra, D.; Brar, S.; Tyagi, R.; Surampalli, R. *Chemosphere* **2010**, *78*, 923 –941.

(93) EU COUNCIL DIRECTIVE (91/271/EEC) concerning urban waste water treatment. (1991).

(94) Kreuzinger, N.; Clara, M.; Strenn, B.; Kroiss, H. *Water Science and Technology* **2004**, *50*, 149–156.

(95) Jiang, J.; Yin, Q.; Zhou, J.; Pearce, P. *Chemosphere* **2005**, *61*, 544 –550.

(96) Andreozzi, R.; Caprio, V.; Insola, A.; Marotta, R. *Catalysis Today* **1999**, *53*, 51–59.

(97) Esplugas, S.; Bila, D. M.; Krause, L. G. T.; Dezotti, M. *Journal of Hazardous Materials* **2007**, *149*, 631–642.

(98) Huber, M. M.; Canonica, S.; Park, G.-Y.; von Gunten, U. *Environmental Science & Technology* **2003**, *37*, 1016–1024.

(99) Katsumata, H.; Kawabe, S.; Kaneco, S.; Suzuki, T.; Ohta, K. *Journal of Photochemistry and Photobiology A: Chemistry* **2004**, *162*, 297–305.

(100) Krichevskaya, M.; Klauson, D.; Portjanskaja, E.; Preis, S. *Ozone: Science & Engineering* **2011**, *33*, 211–223.

(101) Rivas, F. J.; Encinas, n.; Acedo, B.; Beltrán, F. J. *Journal of Chemical Technology & Biotechnology* **2009**, *84*, 589–594.

(102) Rosenfeldt, E. J.; Linden, K. G. *Environmental Science & Technology* **2004**, *38*, 5476–5483.

(103) Young, T.; Geng, M.; Lin, L.; Thagard, S. M. *Journal of Advanced Oxidation Technologies* **2013**, *16*, 89–101.

(104) Bielski, B. H. J.; Cabelli, D. E.; Arudi, R. L.; Ross, A. B. *Journal of Physical and Chemical Reference Data* **1985**, *14*, 1041–1100.

(105) Dainton, F.; Rowbottom, J *Transactions of the Faraday Society* **1953**, *49*, 1160–1173.

(106) Gericke, K.-H.; Klee, S.; Comes, F. J.; Dixon, R. N. *The Journal of Chemical Physics* **1986**, *85*, 4463–4479.

(107) Urey, H.; Dawsey, L.; Rice, F. *Journal of the American Chemical Society* **1929**, *51*, 1371–1383.

(108) Neyens, E.; Baeyens, J. *Journal of Hazardous Materials* **2003**, *98*, 33 –50.

(109) Kaneco, S.; Rahman, M. A.; Suzuki, T.; Katsumata, H.; Ohta, K. *Journal of Photochemistry and Photobiology A: Chemistry* **2004**, *163*, 419–424.

(110) Zapata, A.; Oller, I.; Rizzo, L.; Hilgert, S.; Maldonado, M.; Sanchez-Perez, J.; Malato, S. *Applied Catalysis B: Environmental* **2010**, *97*, 292 –298.

(111) Eliasson, B; Hirth, M; Kogelschatz, U *Journal of Physics D: Applied Physics* **1987**, *20*, 1421.

(112) Zhao, J.; Chen, C.; Ma, W. *Topics in Catalysis* **2005**, *35*, 269–278.

(113) Habisreutinger, S. N.; Schmidt-Mende, L.; Stolarczyk, J. K. *Angewandte Chemie International Edition* **2013**, *52*, 7372–7408.

(114) Landau, L. D.; Lifshitz, D. M., *Quantum mechanics (Non-relativistic theory)*; Institute of Physical Problems, USSR Academy of Sciences: 1958.

(115) Harrison, W. A., *Electronic structure and the properties of solids: the physics of the chemical bond*; Courier Dover Publications: 2012.

(116) Harrison, W. A., *Elementary electronic structure*; World Scientific Singapore: 2004.

(117) Fujishima, A.; Zhang, X.; Tryk, D. A. *Surface Science Reports* **2008**, *63*, 515–582.

(118) Gupta, S.; Tripathi, M. *Chinese Science Bulletin* **2011**, *56*, 1639–1657.

(119) Rothenberger, G.; Moser, J.; Graetzel, M.; Serpone, N.; Sharma, D. K. *Journal of the American Chemical Society* **1985**, *107*, 8054–8059.

(120) Su, R.; Bechstein, R.; So, L.; Vang, R. T.; Sillassen, M.; Esbjoernsson, B.; Palmqvist, A.; Besenbacher, F. *Journal of Physical Chemistry C* **2011**, *115*, 24287–24292.

(121) Hurum, D. C.; Agrios, A. G.; Gray, K. A.; Rajh, T.; Thurnauer, M. C. *The Journal of Physical Chemistry B* **2003**, *107*, 4545–4549.

(122) Hurum, D.; Agrios, A. G.; Gray, K. A.; Rajh, T.; Thurnauer, M. C. *Abstracts of Papers American Chemical Society* **2001**, *222*.

(123) Ding, Z.; Lu, G. Q.; Greenfield, P. F. *Journal of Physical Chemistry B* **2000**, *104*, 4815–4820.

(124) Deskins, N. A.; Kerisit, S.; Rosso, K. M.; Dupuis, M. *Journal of Physical Chemistry C* **2007**, *111*, 9290–9298.

(125) Andronic, L.; Andrasi, D.; Enesca, A.; Visa, M.; Duta, A. *Journal of Sol-Gel Science and Technology* **2011**, *58*, 201–208.

(126) Collins-Martinez, V.; Ortiz, A. L.; Elguezabal, A. A. *International Journal of Chemical Reactor Engineering* **2007**, *5*.

(127) Bickley, R. I.; Gonzalez-Carreno, T.; Lees, J. S.; Palmisano, L.; Tilley, R. J. D. *Journal of Solid State Chemistry* **1991**, *92*, 178–190.

(128) Hurum, D. C.; Gray, K. A.; Rajh, T.; Thurnauer, M. C. *Journal of Physical Chemistry B* **2005**, *109*, 977–980.

(129) Deskins, N. A.; Rousseau, R.; Dupuis, M. *The Journal of Physical Chemistry C* **2009**, *113*, 14583–14586.

(130) Kerisit, S.; Deskins, N. A.; Rosso, K. M.; Dupuis, M. *The Journal of Physical Chemistry C* **2008**, *112*, 7678–7688.

(131) Mercado, C. C.; Knorr, F. J.; McHale, J. L.; Usmani, S. M.; Ichimura, A. S.; Saraf, L. V. *The Journal of Physical Chemistry C* **2012**, *116*, 10796–10804.

(132) Diebold, U. *Surface Science Reports* **2003**, *48*, 53–229.

(133) Morgan, B. J.; Watson, G. W. *Physical Review B* **2009**, *80*, 233102.

(134) Onda, K.; Li, B.; Zhao, J.; Jordan, K. D.; Yang, J.; Petek, H. *Science* **2005**, *308*, 1154–1158.

(135) Hoffmann, M. R.; Martin, S. T.; Choi, W.; Bahnemann, D. W. *Chemical Reviews* **1995**, *95*, 69–96.

(136) Rabani, J.; Yamashita, K.; Ushida, K.; Stark, J.; Kira, A. *The Journal of Physical Chemistry B* **1998**, *102*, 1689–1695.

(137) Thompson, T. L.; Yates, J. T. *Chemical Reviews* **2006**, *106*, 4428–4453.

(138) Fujishima, A.; Rao, T. N.; Tryk, D. A. *Journal of Photochemistry and Photobiology C: Photochemistry Reviews* **2000**, *1*, 1–21.

(139) Zhang, J.; Nosaka, Y. *The Journal of Physical Chemistry C* **2014**, *118*, 10824–10832.

(140) Wahlstroem, E.; Vestergaard, E. K.; Schaub, R.; Raennau, A.; Vestergaard, M.; Laegsgaard, E.; Stensgaard, I.; Besenbacher, F. *Science* **2004**, *303*, 511–513.

(141) Hirakawa, T.; Daimon, T.; Kitazawa, M.; Ohguri, N.; Koga, C.; Negishi, N.; Matsuzawa, S.; Nosaka, Y. *Journal of Photochemistry and Photobiology A: Chemistry* **2007**, *190*, 58–68.

(142) Xiang, Q.; Yu, J.; Wong, P. K. *Journal of Colloid and Interface Science* **2011**, *357*, 163 –167.

(143) Ollis, D. *Topics in Catalysis* **2005**, *35*, 217–223.

(144) Konstantinou, I. K.; Albanis, T. A. *Applied Catalysis B: Environmental* **2004**, *49*, 1 –14.

(145) Butler, E. C.; Davis, A. P. *Journal of Photochemistry and Photobiology A: Chemistry* **1993**, *70*, 273 –283.

(146) Uyguner, C. S.; Bekbolet, M. *Desalination* **2005**, *176*, 167 –176.

(147) Coleman, H. M.; Eggins, B. R.; Byrne, J.; Palmer, F. L.; King, E. *Applied Catalysis B: Environmental* **2000**, *24*, L1 –L5.

(148) Gaya, U. I.; Abdullah, A. H. *Journal of Photochemistry and Photobiology C: Photochemistry Reviews* **2008**, *9*, 1 –12.

(149) Poulios, I.; Aetopoulou, I. *Environmental Technology* **1999**, *20*, 479–487.

(150) Poulios, I.; Micropoulou, E.; Panou, R.; Kostopoulou, E. *Applied Catalysis B: Environmental* **2003**, *41*, 345–355.

(151) Houas, A.; Lachheb, H.; Ksibi, M.; Elaloui, E.; Guillard, C.; Herrmann, J. . *Applied Catalysis B: Environmental* **2001**, *31*, 145–157.

(152) Tang, W. Z.; An, H. *Chemosphere* **1995**, *31*, 4157–4170.

(153) Pelizzetti, E.; Minero, C. *Electrochimica Acta* **1993**, *38*, 47–55.

(154) Valencia, S.; Cataño, F.; Rios, L.; Restrepo, G.; Marín, J. *Applied Catalysis B: Environmental* **2011**, *104*, 300–304.

(155) Ollis, D. F. *The Journal of Physical Chemistry B* **2005**, *109*, 2439–2444.

(156) Monllor-Satoca, D.; Gomez, R.; Gonzalez-Hidalgo, M.; Salvador, P. *Catalysis Today* **2007**, *129*, 247–255.

(157) Brinkmann, T. Alkalischer und solarinduzierter Abbau von natürlicher organischer Materie., Ph.D. Thesis, Universät Karlsruhe, 2003.

(158) De Laurentiis, E.; Prasse, C.; Ternes, T. A.; Minella, M.; Maurino, V.; Minero, C.; Sarakha, M.; Brigante, M.; Vione, D. *Water Research* **2014**, *53*, 235–248.

(159) De Laurentiis, E.; Chiron, S.; Kouras-Hadef, S.; Richard, C.; Minella, M.; Maurino, V.; Minero, C.; Vione, D. *Environmental Science & Technology* **2012**, *46*, 8164–8173.

(160) Lee, E.; Shon, H. K.; Cho, J. *Journal of Hazardous Materials* **2014**, *276*, 1–9.

(161) Lindeman, L. P.; Guffy, J. C. *The Journal of Chemical Physics* **1958**, *29*, 247–248.

(162) Zhang, D. H.; Zhang, J. Z. H. *The Journal of Chemical Physics* **1993**, *98*, 6276–6283.

(163) Bahnemann, D; Cunningham, J; Fox, M.; Pelizzetti, E; Pichat, P; Serpone, N; Helz, G.; Zepp, R.; Crosby, D. *Lewis, Boca Raton, FL* **1994**, 261.

(164) Williamson, C. E.; Stemberger, R. S.; Morris, D. P.; Frost, T. M.; Paulsen, S. G. *Limnology and Oceanography* **1996**, *41*, 1024–1034.

(165) Frimmel, F. H.; Bauer, H.; Putzien, J.; Murasecco, P.; Braun, A. M. *Environmental Science & Technology* **1987**, *21*, 541–545.

(166) Zepp, R. G.; Schlotzhauer, P. F.; Sink, R. M. *Environmental Science & Technology* **1985**, *19*, 74–81.

(167) Blough, N.; Zepp, R. *Active Oxygen in Chemistry*, Foote, C., Valentine, J., Greenberg, A., Liebman, J., Eds.; Structure Energetics and Reactivity in Chemistry, Vol. 2; Springer Netherlands: 1995; Chapter 8, pp 280–333.

(168) Tratnyek, P. G.; Hoigne, J. *Environmental Science & Technology* **1991**, *25*, 1596–1604.

(169) Yasuhisa, T.; Hideki, H.; Muneyoshi, Y. *International Journal of Biochemistry* **1993**, *25*, 491–494.

(170) Buxton, G. V.; Greenstock, C. L.; Helman, W. P.; Ross, A. B. *Journal of Physical and Chemical Reference Data* **1988**, *17*, 513–886.

(171) Adams, G. E.; Boag, J. W.; Michael, B. D. *Transactions of the Faraday Society* **1965**, *61*, 1417–1424.

(172) Buffle, M.-O.; Schumacher, J.; Meylan, S.; Jekel, M.; von Gunten, U. *Ozone: Science & Engineering* **2006**, *28*, 247–259.

(173) Von Gunten, U. *Water Research* **2003**, *37*, 1443 –1467.

(174) Elovitz, M. S.; von Gunten, U.; Kaiser, H.-P. *Ozone: Science & Engineering* **2000**, *22*, 123–150.

(175) Dorfman, L. M. *NSRDS* **1973**.

(176) Kondrakov, A. O.; Ignatev, A. N.; Frimmel, F. H.; Braese, S.; Horn, H.; Revelsky, A. I. *Applied Catalysis B: Environmental* **2014**, *160-161*, 106–114.

(177) Gueltekin, I.; Ince, N. H. *Journal of Environmental Management* **2007**, *85*, 816–832.

(178) Tsai, W.-T.; Lee, M.-K.; Su, T.-Y.; Chang, Y.-M. *Journal of Hazardous Materials* **2009**, *168*, 269–275.

(179) Chong, M. N.; Jin, B.; Chow, C. W. K.; Saint, C. *Water Research* **2010**, *44*, 2997–3027.

(180) Rodríguez, E. M.; Fernández, G.; Klamerth, N.; Maldonado, M. I.; Alvarez, P. M.; Malato, S. *Applied Catalysis B: Environmental* **2010**, *95*, 228–237.

(181) Baeza, C.; Knappe, D. R. U. *Water Research* **2011**, *45*, 4531–4543.

(182) Lam, S.-M.; Sin, J.-C.; Abdullah, A. Z.; Mohamed, A. R. *Ceramics International* **2013**, *39*, 2343–2352.

(183) Chiang, K.; Lim, T. M.; Tsen, L.; Lee, C. C. *Applied Catalysis A-General* **2004**, *261*, 225–237.

(184) Lee, J.-M.; Kim, M.-S.; Kim, B.-W. *Water Research* **2004**, *38*, 3605–3613.

(185) Thiruvenkatachari, R.; Kwon, T. O.; Moon, I. S. *Separation Science and Technology* **2005**, *40*, 2871–2888.

(186) Mezcua, M.; Ferrer, I.; Hernando, M. D.; Fernandez-Alba, A. R. *Food Additives and Contaminants* **2006**, *23*, 1242–1251.

(187) Nomiyama, K.; Tanizaki, T.; Koga, T.; Arizono, K.; Shinohara, R. *Archives of Environmental Contamination and Toxicology* **2007**, *52*, 8–15.

(188) Torres, R. A.; Nieto, J. I.; Combet, E.; Petrier, C.; Pulgarin, C. *Applied Catalysis B-Environmental* **2008**, *80*, 168–175.

(189) Subagio, D. P.; Srinivasan, M.; Lim, M.; Lim, T.-T. *Applied Catalysis B: Environmental* **2010**, *95*, 414–422.

(190) Chenzhong Jia Yanxin Wang, C. Z. Q. Q. S. K.; Yao, S. K. *Environmental Engineering Science* **2012**, *29*, 630–637.

(191) Sin, J.-C.; Lam, S.-M.; Mohamed, A. R.; Lee, K.-T. *International Journal of Photoenergy* **2012**, *2012*.

(192) Maroga Mboula, V.; Héquet, V.; Andrès, Y.; Pastrana-Martínez, L. M.; Doña-Rodríguez, J. M.; Silva, A. M. T.; Falaras, P. *Water Research* **2013**, *47*, 3997–4005.

(193) Ohko, Y.; Ando, I.; Niwa, C.; Tatsuma, T.; Yamamura, T.; Nakashima, T.; Kubota, Y.; Fujishima, A. *Environmental Science & Technology* **2001**, *35*, 2365–2368.

(194) Watanabe, N.; Horikoshi, S.; Kawabe, H.; Sugie, Y.; Zhao, J. C.; Hidaka, H. *Chemosphere* **2003**, *52*, 851–859.

(195) Neamtu M., M.; Frimmel, F. H. *Water Research* **2006**, *40*, 3745–3750.

(196) Kitamura, S.; Suzuki, T.; Sanoh, S.; Kohta, R.; Jinno, N.; Sugihara, K.; Yoshihara, S.; Fujimoto, N.; Watanabe, H.; Ohta, S. *Toxicological Sciences* **2005**, *84*, 249–259.

(197) Sörensen, M.; Frimmel, F. H. *Water Research* **1997**, *31*, 2885–2891.

(198) Cabrera, M. I.; Alfano, O. M.; Cassano, A. E. *Journal of Physical Chemistry* **1996**, *100*, 20043–20050.

(199) Atkinson, A.; Roy, D. *Environmental and Molecular Mutagenesis* **1995**, *26*, 60–66.

(200) Atkinson, A.; Roy, D. *Biochemical and Biophysical Research Communications* **1995**, *210*, 424–433.

(201) Izzotti, A.; Kanitz, S.; D'Agostini, F.; Camoirano, A.; De Flora, S. *Mutation Research/Genetic Toxicology and Environmental Mutagenesis* **2009**, *679*, 28–32.

(202) De Flora, S.; Micale, R. T.; La Maestra, S.; Izzotti, A.; D'Agostini, F.; Camoirano, A.; Davoli, S. A.; Troglio, M. G.; Rizzi, F.; Davalli, P.; Bettuzzi, S. *Toxicological Sciences* **2011**, *122*, 45–51.

(203) Ye, X.; Zhou, X.; Needham, L. L.; Calafat, A. M. *Analytical and Bioanalytical Chemistry* **2011**, *399*, 1071–1079.

(204) Li, Y.; Wen, B.; Yu, C.; Chen, C.; Ji, H.; Ma, W.; Zhao, J. *Chemistry A European Journal* **2012**, *18*, 2030–2039.

(205) Lee, J. W.; Kwon, T. O.; Thiruvenkatachari, R.; Moon, I. S. *Journal of Environmental Sciences-China* **2006**, *18*, 193–200.

(206) Peltonen Kimmo Antti Zitting, K. H. I. A. *Photochemistry and Photobiology* **1986**, *43*, 481–484.

(207) Kondrakov, A. O.; Ignatev, A. N.; Lunin, V. V.; Frimmel, F. H.; Braese, S.; Horn, H. *Applied Catalysis B: Environmental* **2015**, *submitted*.

(208) Coronado, J. M.; Soria, J. *Catalysis Today* **2007**, *123*, 37–41.

(209) Nosaka, Y.; Komori, S.; Yawata, K.; Hirakawa, T.; Nosaka, A. Y. *Physical Chemistry Chemical Physics* **2003**, *5*, 4731–4735.

(210) Rinke, M.; Zetzsch, C. *Berichte der Bunsengesellschaft für physikalische Chemie* **1984**, *88*, 55–62.

(211) Draper, R. B.; Fox, M. A.; Pelizzetti, E.; Serpone, N. *The Journal of Physical Chemistry* **1989**, *93*, 1938–1944.

(212) Sun, L. Z.; Bolton, J. R. *Journal of Physical Chemistry* **1996**, *100*, 4127–4134.

(213) Minero, C.; Mariella, G.; Maurino, V.; Vione, D.; Pelizzetti, E. *Langmuir* **2000**, *16*, 8964–8972.

(214) Erbs, W.; Desilvestro, J.; Borgarello, E.; Graetzel, M. *The Journal of Physical Chemistry* **1984**, *88*, 4001–4006.

(215) Lin, H. F.; Ravikrishna, R; Valsaraj, K. *Separation and Purification Technology* **2002**, *28*, 87 –102.

(216) Wahab, H. S.; Bredow, T.; Aliwi, S. M. *Chemical Physics* **2008**, *353*, 93–103.

(217) Bhatkhande, D. S.; Sawant, S. B.; Schouten, J. C.; Pangarkar, V. G. *Journal of Chemical Technology and Biotechnology* **2004**, *79*, 354–360.

(218) Kyung, H.; Lee, J.; Choi, W. *Environmental Science & Technology* **2005**, *39*, 2376–2382.

(219) Jiang, P. Y.; Katsumura, Y.; Ishigure, K.; Yoshida, Y. *Inorganic Chemistry* **1992**, *31*, 5135–5136.

(220) Brunauer, S.; Emmett, P. H.; Teller, E. *Journal of the American Chemical Society* **1938**, *60*, 309–319.

(221) López-Aranguren, P; Saurina, J; Vega, L.; Domingo, C *Microporous and Mesoporous Materials* **2012**, *148*, 15–24.

(222) Dimitriu, M.; Ivan, L.-M.; Dorohoi, D.-O. *Romanian Journal of Physics* **2008**, *53*, 79–84.

(223) Kikuchi, Y.; Sunada, K.; Iyoda, T.; Hashimoto, K.; Fujishima, A. *Journal of Photochemistry and Photobiology A: Chemistry* **1997**, *106*, 51–56.

(224) Cussler, E. L., *Diffusion: mass transfer in fluid systems*; Cambridge university press: 2009.

(225) Pang, X.; Chen, C.; Ji, H.; Che, Y.; Ma, W.; Zhao, J. *Molecules* **2014**, *19*, 16291–16311.

(226) Kondrakov, A. O.; Ignatev, A. N.; Revelsky, I. A.; Frimmel, F. H.; Braese, S.; Horn, H. *Environmental Science & Technology* **2015**, *in preparation.*

(227) Jang, B. N.; Wilkie, C. A. *Polymer Degradation and Stability* **2004**, *86*, 419 –430.

(228) Vione, D.; Minella, M.; Maurino, V.; Minero, C. *Chemistry-A European Journal* **2014**.

(229) Schweitzer, C.; Schmidt, R. *Chemical Reviews* **2003**, *103*, 1685–1757.

(230) Koenig, S. H.; Brown, R. D. *Proceedings of the National Academy of Sciences* **1972**, *69*, 2422–2425.

(231) Vione, D.; Falletti, G.; Maurino, V.; Minero, C.; Pelizzetti, E.; Malandrino, M.; Ajassa, R.; Olariu, R.-I.; Arsene, C. *Environmental Science & Technology* **2006**, *40*, 3775–3781.

(232) Bauer, M.; Heitmann, T.; Macalady, D. L.; Blodau, C. *Environmental Science & Technology* **2007**, *41*, 139–145.

(233) Tercero Espinoza, L. A. Heterogeneous photocatalysis with titanium dioxide suspensions containing bromide and dissolved organic carbon., Ph.D. Thesis, Karlsruhe Institute of Technology, 2010.

(234) Huber, S. A.; Balz, A.; Frimmel, F. H. *Fresenius' Journal of Analytical Chemistry* **1994**, *350*, 496–503.

(235) Dalrymple, R. M.; Carfagno, A. K.; Sharpless, C. M. *Environmental Science & Technology* **2010**, *44*, 5824–5829.

(236) Stryer, L. *Journal of the American Chemical Society* **1966**, *88*, 5708–5712.

(237) Monnier, J. R.; Medlin, J.; Barteau, M. *Journal of Catalysis* **2001**, *203*, 362–368.

(238) Canonica, S.; Jans, U.; Stemmler, K.; Hoigne, J. *Environmental Science & Technology* **1995**, *29*, 1822–1831.

(239) Guo, C.; Ge, M.; Liu, L.; Gao, G.; Feng, Y.; Wang, Y. *Environmental Science & Technology* **2009**, *44*, 419–425.

(240) Peller, J. R.; Mezyk, S. P.; Cooper, W. J. *Research on Chemical Intermediates* **2009**, *35*, 21–34.

(241) Tao, H.; Hao, S.; Chang, F.; Wang, L.; Zhang, Y. R.; Cai, X. H.; Zeng, J. S. D. *Water Air and Soil Pollution* **2011**, *214*, 491–498.

(242) Wang, G.; Xu, L.; Zhang, J.; Yin, T.; Han, D. *International Journal of Photoenergy* **2012**, *2012*, 9.

(243) Suttiponparnit, K.; Jiang, J.; Sahu, M.; Suvachittanont, S.; Charinpanitkul, T.; Biswas, P. *Nanoscale Research Letters* **2011**, *6*, 27.

(244) Doll, T. E. Photochemischer und photokatalytische Abbau von Carbamazepin, Clofibrinsäure, Iomeprol und Iopromid., Ph.D. Thesis, Universität Karlsruhe, 2004.

(245) Espinoza, L. A. T.; Malerba, R. R.; Frimmel, F. H. *Catalysis Today* **2010**, *151*, 84 –88.

(246) Wang, S. Y. *Photochemistry and Photobiology* **1962**, *1*, 135–145.

(247) Defoin, A.; Defoin-Straatmann, R.; Hildenbrand, K.; Bittersmann, E.; Kreft, D.; Kuhn, H. *Journal of Photochemistry* **1986**, *33*, 237 –255.

(248) Kuhn, H.; Braslavsky, S.; Schmidt, R *Pure and Applied Chemistry* **2004**, *76*, 2105–2146.

(249) Petrauskas, A.; Kolovanov, E. *Perspectives in Drug Discovery and Design* **2000**, *19*, 99–116.

(250) Huber, S. A.; Frimmel, F. H. *Analytical Chemistry* **1991**, *63*, 2122–2130.

(251) Hansch, C. H.; Leo, A.; Hoekman, D., *Exploring Qsar: Hydrophobic, Electronic, and Steric Constants*; American Chemical Society: 1995.

(252) DVGW UV-Geraete zur Desinfektion in der Wasserversorgung., Standard, 2006.

(253) Stafford, U.; Gray, K. A.; Kamat, P. V. *Research on Chemical Intermediates* **1997**, *23*, 355–388.

(254) Curco, D.; Gimenez, J.; Addardak, A.; Cervera-March, S.; Esplugas, S. *Catalysis Today* **2002**, *76*, 177–188.

(255) Tsai, W.-T. *Journal of Environmental Science and Health, Part C* **2006**, *24*, 225–255.

(256) Zheng, D.; Wang, N.; Wang, X.; Tang, Y.; Zhu, L.; Huang, Z.; Tang, H.; Shi, Y.; Wu, Y.; Zhang, M.; Lu, B. *Journal of Hazardous Materials* **2012**, *199*, 426–432.

(257) Yalkowsky, S. H.; Orr, R. J.; Valvani, S. C. *Industrial & Engineering Chemistry Fundamentals* **1979**, *18*, 351–353.

(258) Lopez-Aranguren, P.; Saurina, J.; Vega, L.; Domingo, C. *Microporous and Mesoporous Materials* **2012**, *148*, 15 –24.

List of Figures

List of Tables

A

A.1 Supplementary Data

A.1.1 DLS Data

Stability of TiO_2 suspensions in the experiments described in section 3.1 was controlled by ZP measurements. For this, 1 ml suspension samples were incubated in a ZP analyzer cell (subsection 6.2.9) for 1 min and then ZP measurements were conducted (Table A.1).

Table A.1: Zeta-potential of TiO_2 particles during BPA photocatalytic degradation.

Time, min	ZP, mV
0	-40
60	-28
80	-22
100	-19
Mean	-27
St. Dev.	8.38

A.1.2 Additional Kinetic Data on BPs Photolysis

As discussed in section 3.3.1, we presumed an enhancement of BPs degradation by direct photolysis via autosensitization. In particular, we supposed that interactions of the excited BPs transients with each other or dissolved O_2 led to promotion of the degradation via generation of ·OH. A comparison of the kinetic constants given in Figure A.1 indicated that a presence of iPrOH strongly affected the kinetics of BPs degradation.

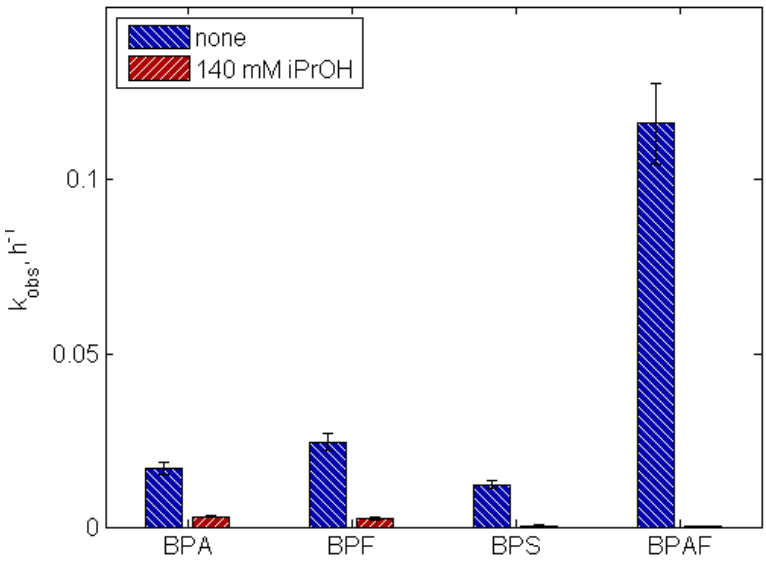

Figure A.1: Effect of iPrOH on degradation of BPs by direct photolysis under simulated solar light. ρ_0(BPA) = ρ_0(BPF) = ρ_0(BPS) = 10 mg L^{-1}, ρ_0(BPAF) = 3 mg L^{-1}, I_0 = 5 µE s^{-1}, c_0(iPrOH) = 140 mM, pH 7, T = 25 °C.

In addition, a change in the initial BPF concentration from ρ_0(BPF) = ρ_0(BPS) = 10 mg L^{-1} to ρ_0(BPF) = ρ_0(BPS) = 1 mg L^{-1} resulted in a k = 0.0033 h^{-1}, which was much closer to that measured in the experiments with iPrOH. Thus, we conducted all the experiment on the direct photolysis in presence of 140 mM of iPrOH in order to avoid generation of ·OH upon autosensitized side reactions of BPs.

As discussed in subsection 3.3.2, all the profiles of BPs degradation by HO24-sensitized photolysis were analyzed under the first-order kinetics approximation. As an example, Figure A.2 shows plots $ln\frac{c(\text{BPs})}{c_0(\text{BPs})}$ *vs.* t for the degradation of BPs by HO24-sensitized photolysis in presence/absence of iPrOH. Depicted kinetic profiles were satisfactory fitted by a linear regression. The calculated k and R^2 values for these and all the other BPs degradation profiles are summarized in Table A.2.

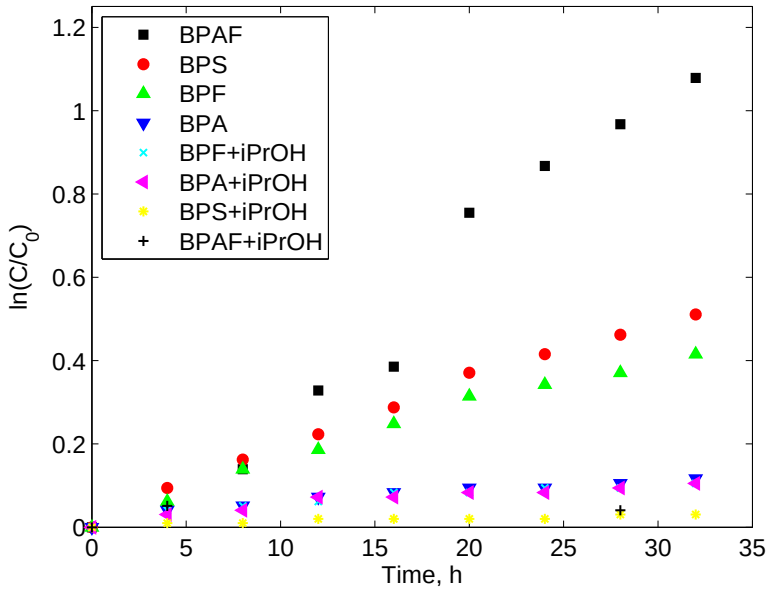

Figure A.2: $ln\frac{c(\text{BPs})}{c_0(\text{BPs})}$ - t dependence for BPs degradation by HO24-sensitized photolysis in presence/absence of iPrOH. $\rho_0(\text{BPA}) = \rho_0(\text{BPF}) = \rho_0(\text{BPS}) = 10$ mg L^{-1}, $\rho_0(\text{BPAF}) = 3$ mg L^{-1}, $I_0 = 5$ µE s^{-1}, $c_0(\text{iPrOH}) = 140$ mM, pH 4.8 (not adjusted), T = 25 °C.

Table A.2: Parameters of the linear regression obtained for the kinetic profiles of BPs under the first-order rate approximation.

Process	k, h^{-1}	R^2
BPA	0.002	0.9884
BPA + iPrOH	0.003	0.8934
BPA + HO24	0.004	0.9799
BPA + HO24 + iPrOH	0.003	0.9228
BPA + HO24 + Fe^{3+}	0.004	0.9949
BPA + HO24 + NO_3^-	0.004	0.9965
BPA + HO24 + HCO_3^-	0.0042	0.9912
BPF	0.025	0.9970
BPF + iPrOH	0.002	0.9652
BPF + HO24	0.013	0.9876
BPF + HO24 + iPrOH	0.003	0.8988
BPF + HO24 + Fe^{3+}	0.013	0.9980
BPF + HO24 + NO_3^-	0.008	0.9912

BPF + HO24 + HCO_3^-	0.009	0.9848
BPS	0.012	0.9953
BPS + iPrOH	0	
BPS + HO24	0.016	0.9923
BPS + HO24 + iPrOH	0	
BPS + HO24 + Fe^{3+}	0.020	0.9906
BPS + HO24 + NO_3^-	0.01	0.9997
BPS + HO24 + HCO_3^-	0.01	0.9971
BPAF	0.196	0.9627
BPAF + iPrOH	0	
BPAF + HO24	0.039	0.9679
BPAF + HO24 + iPrOH	0	
BPAF + HO24 + Fe^{3+}	0.024	0.9872
BPAF + HO24 + NO_3^-	0.014	0.9889
BPAF + HO24 + HCO_3^-	0.024	0.9991

A.1.3 Estimation of the Inner Filter Effect of HO24

In order to estimate the fraction of simulated solar light absorbed by HO24, we measured its UV-vis absorption spectrum in the range between 300 and 800 nm.

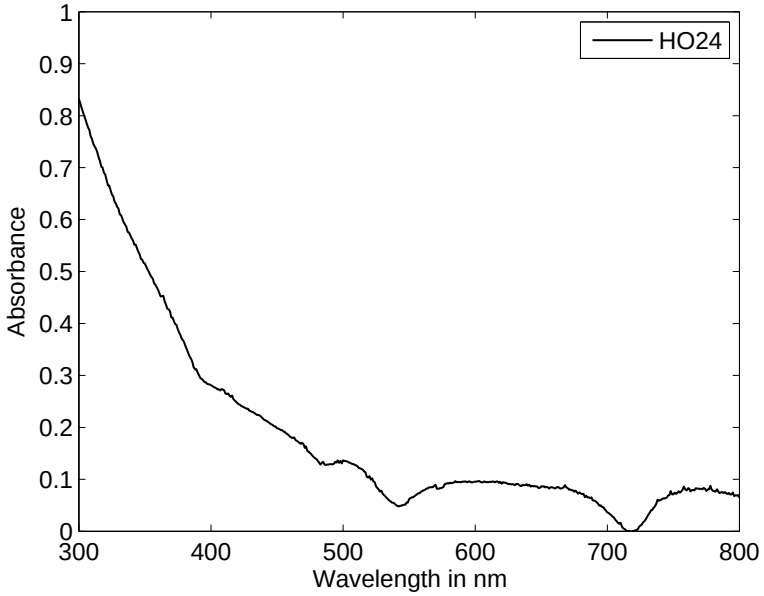

Figure A.3: UV-vis spectrum of the aqueous solution of HO24. ϱ_0(HO24) = 0.0085 gC L^{-1}, pH 4.0 (not adjusted), path length – 4 cm, chosen according to the irradiation path length used (subsection 6.3.2).

UV-vis measurements were conducted using a spectrophotometer Cary 50, Varian. The fraction of solar irradiation absorbed by HO24 in presence of BPs was evaluated by the inner filter model [197, 244]:

$$F_{\mathrm{HO24}} \cong \sum_{\lambda_i} F_{\mathrm{HO24},\lambda_i} = \sum_{i} \frac{\epsilon_{\mathrm{HO24},\lambda_i}\rho(\mathrm{HO24})}{\mu(\mathrm{BPs},\lambda_i)\rho(\mathrm{BPs}) + \epsilon_{\mathrm{HO24},\lambda_i}\rho(\mathrm{HO24})} \tag{A.1}$$

where F_{HO24} is the fraction of UVA light absorbed by HO24; $\mu(\mathrm{BPs},\lambda_i)$ and $\epsilon_{\mathrm{HO24},\lambda_i}$ are the extinction coefficients of BPs and HO24 expressed in M^{-1} cm^{-1} and gC L^{-1} cm^{-1}, respectively; ρ(BPs) and ρ(HO24) are the concentrations of BPs and HO24 in g L^{-1} and gC L^{-1}, correspondingly.

Thus, calculation on the base of the absorbance data extracted from the UV-vis spectra given in Figure A.3 and Figure 3.19 according to Equation A.1 resulted in $F_{\mathrm{HO24}} \approx 99\%$ and $F_{\mathrm{BPA}} = F_{\mathrm{BPF}} = F_{\mathrm{BPS}} = F_{\mathrm{BPAF}} \leq 1\%$.

A.1.4 UV Spectra of BPs' Catechols

The UV spectra of BPs' catechols (Figures A.4-A.7) were extracted from the HPLC-UV data obtained in parallel with HPLC-MRM measurements. The assignment of the HPLC-UV peaks to the BPs' catechols was conducted on their retention times on HPLC-MRM chromatograms. The spectra of BPA, BPS and BPAF catechols are given as averages over multiply DAD signals in order to improve the signal-to-noise ratio.

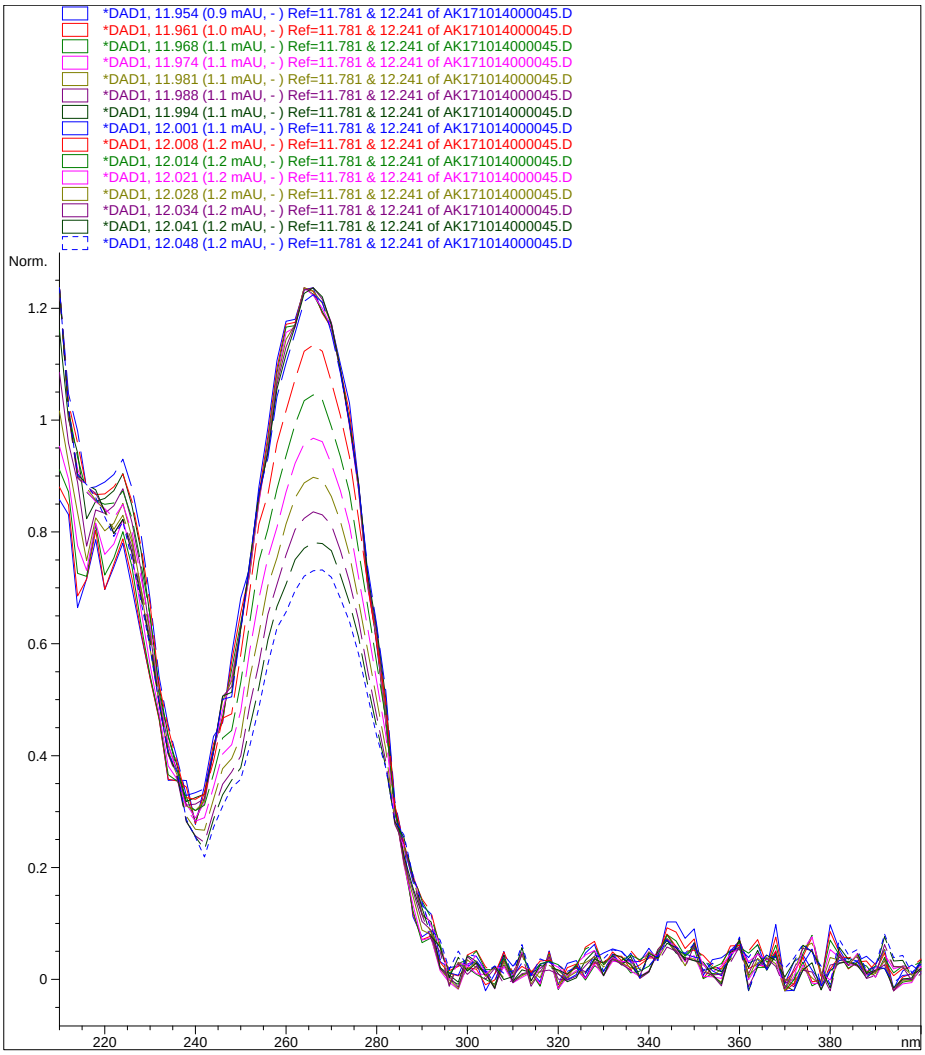

Figure A.4: Averaged UV spectrum of BPA catechol.

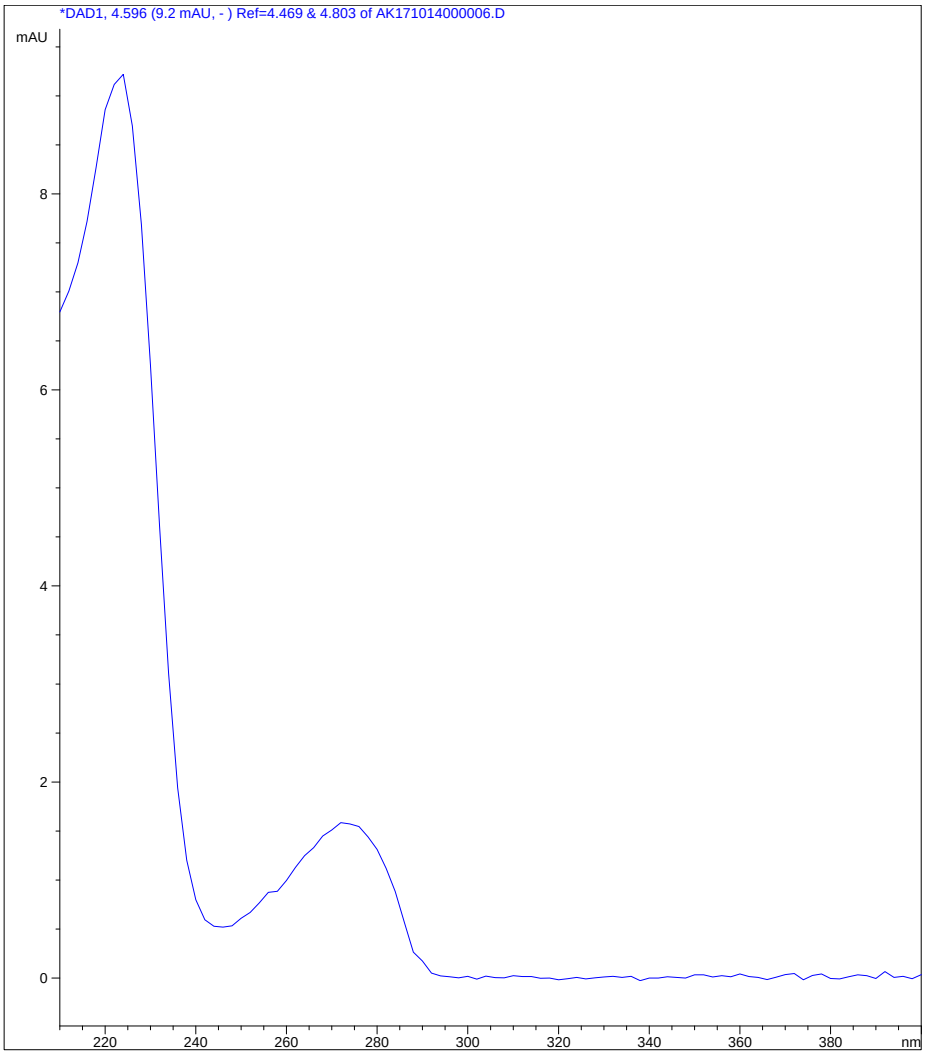

Figure A.5: UV spectrum of BPF catechol.

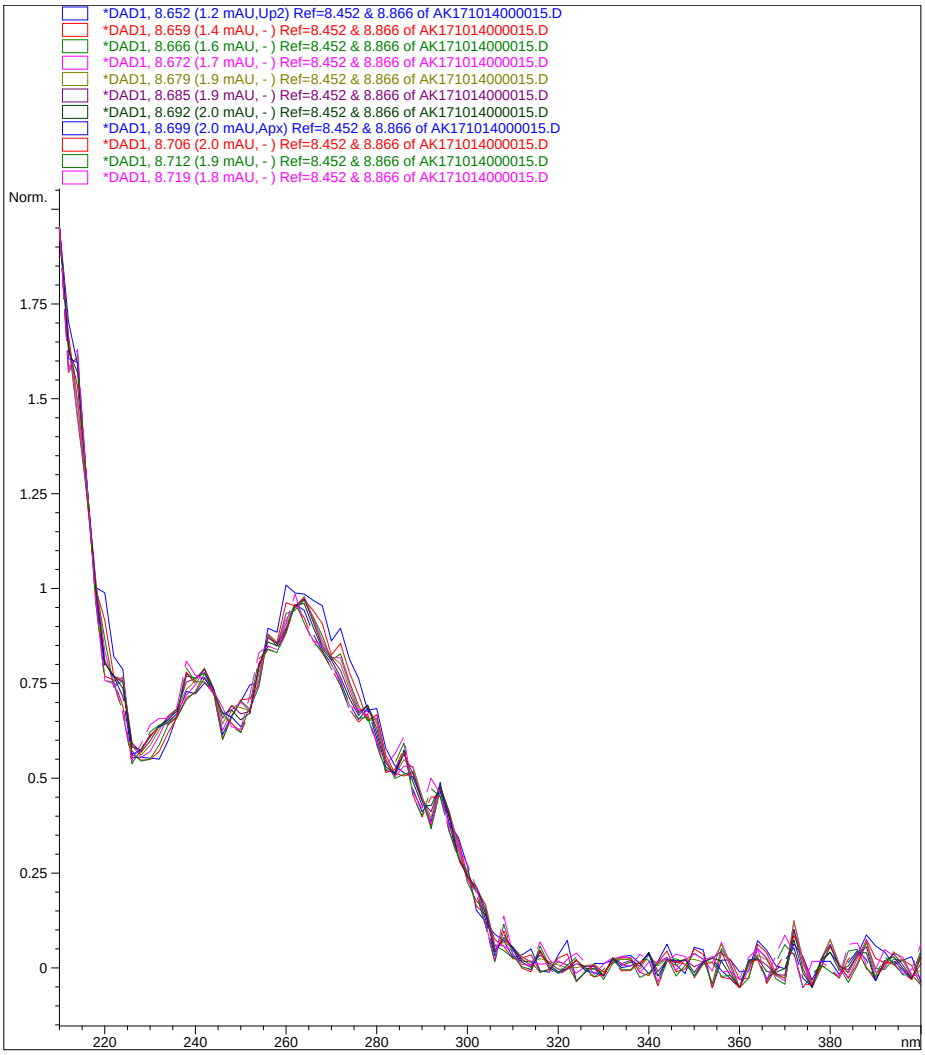

Figure A.6: Averaged UV spectrum of BPS catechol.

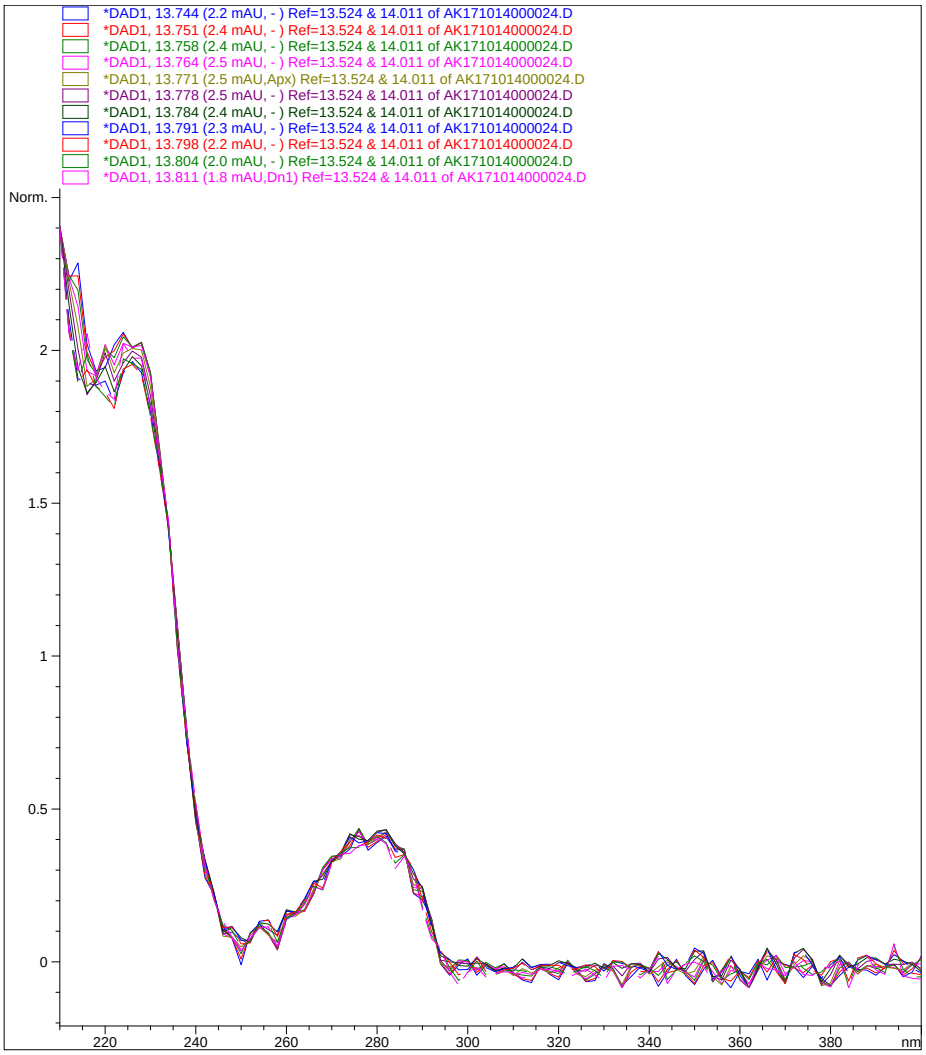

Figure A.7: Averaged UV spectrum of BPAF catechol.

A.1.5 DOC and SEC Data on HO24 Transformations

Firstly, we compared decrease in the total DOC content with the BPs concentrations decrease observed after 32 h of degradation (Table A.3). Even though we would assume that the degraded part of BPs was mineralized, changes in their concentrations were much lower as the total DOC decrease for all the BPs examined. It suggested that the DOC losses occurred due to the mineralization of HO24 and it was therefore reasonable to expect its significant structural changes.

Table A.3: Rates of HO24-sensitized photolysis.

Compound	Irradiation time, h		$\Delta\rho$(BPs(DOC)) degraded, mg(C) L^{-1}
	0	32	
BPA, mg L^{-1}	10	9.0	1
BPA + HO24, mgC L^{-1}	16.4	10.9	5.5
BPF, mg L^{-1}	10	6.8	3.2
BPF + HO24, mgC L^{-1}	16.3	9.9	6.4
BPS, mg L^{-1}	10	6.1	3.9
BPS + HO24, mgC L^{-1}	14.2	8.5	5.7
BPAF, mg L^{-1}	1.8	0.6	1.2
BPAF + HO24, mgC L^{-1}	10.1	4.3	5.8

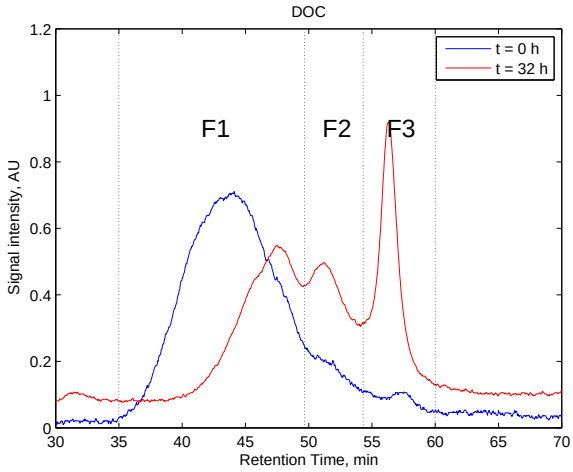

(a)

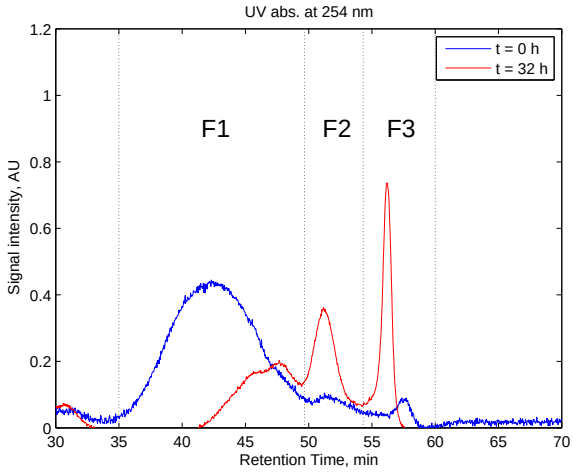

(b)

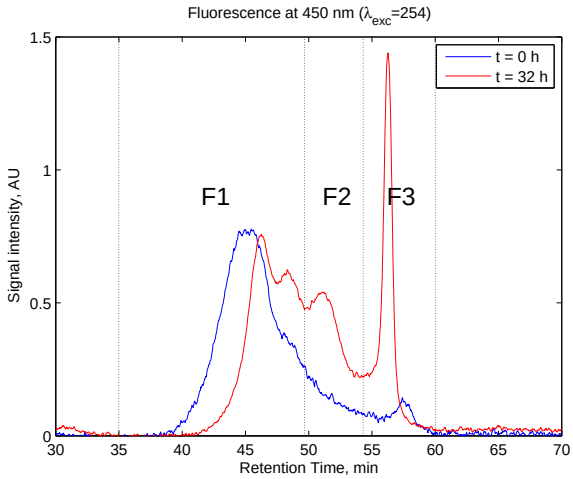

(c)

Figure A.8: SEC-DOC/UV/FL chromatograms of the HO24 samples taken during degradation of BPF by HO24-sensitized photolysis.

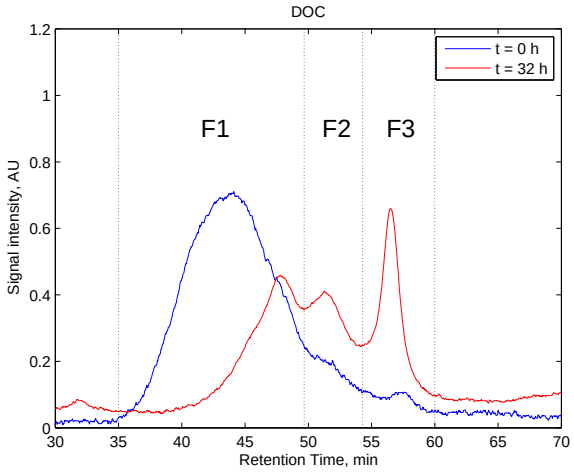

(a)

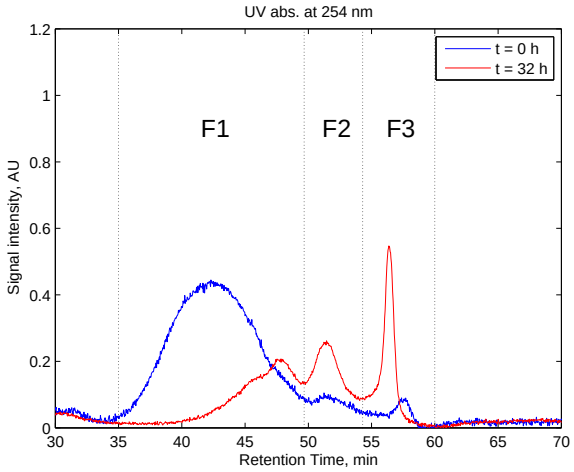

(b)

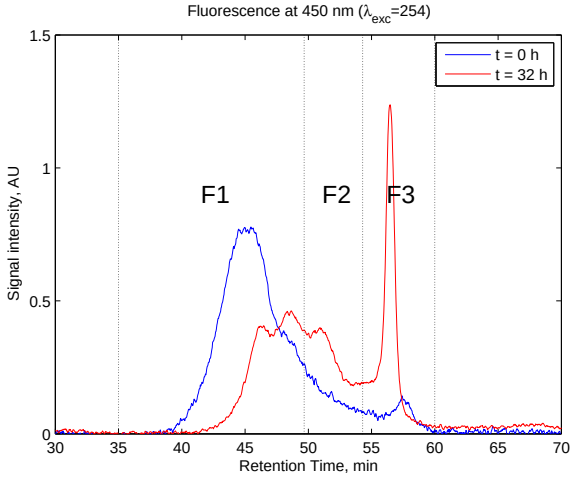

(c)

Figure A.9: SEC-DOC/UV/FL chromatograms of the HO24 samples taken during degradation of BPS by HO24-sensitized photolysis.

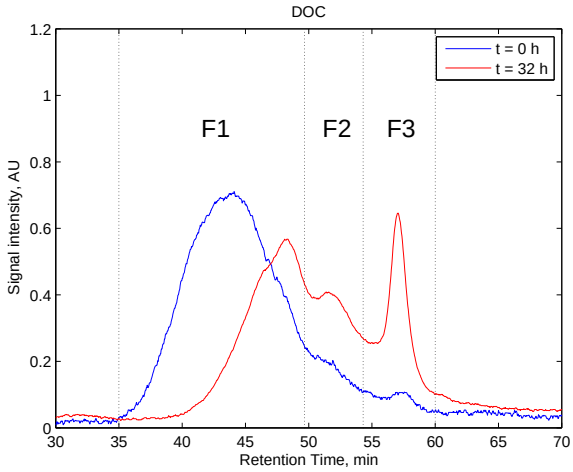

(a)

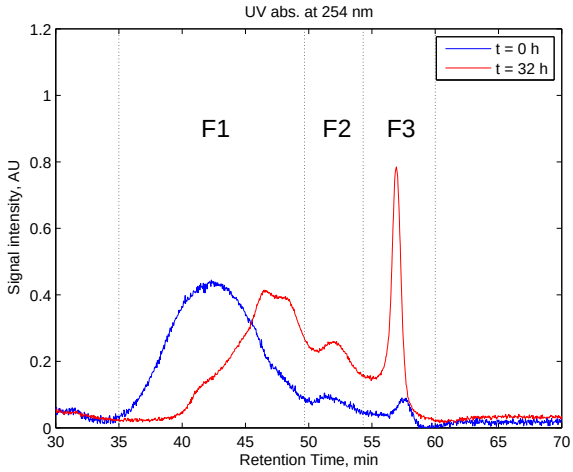

(b)

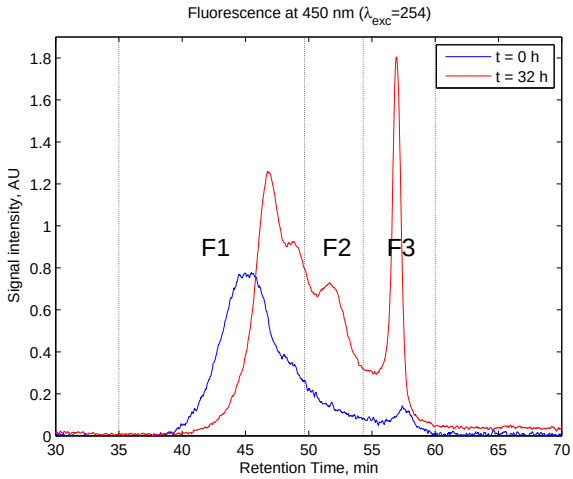

(c)

Figure A.10: SEC-DOC/UV/FL chromatograms of the HO24 samples taken during degradation of BPAF by HO24-sensitized photolysis.

A.1.6 Estimations of SG Particles Geometry

The ratio of a SG pore entrance area to the solution volume was calculated as follows

$$S = \frac{S_{SG\ pores}}{V_{solution}} f \tag{A.2}$$

where $S_{SG\ pores}$ is the total SG pore entrance area; f is the SG to solution volumes ratio arising due to the one-dimensional consideration as depicted in Figure 3.16 in order to reduce the diffusion parameters to the common overall solution volume. Under assumption of cubic geometry of the SG particles, $S_{SG\ pores}$ is given by

$$S_{SG\ pores} = \frac{V_{SG\ pores}}{d} = \frac{m_{SG}}{d}\left(\frac{1}{\rho_{SG}} - \frac{1}{\rho(\mathrm{SiO_2})}\right) \tag{A.3}$$

where d is an average particle size; m_{SG} is the total SG phase mass; ρ_{SG} and $\rho(\mathrm{SiO_2})$ are SG and SiO_2 densities, respectively.
By turn, the SG to solution volumes ratio f equals to

$$f = \frac{V_{solution}}{V_{SG\ pores}} \tag{A.4}$$

A.1.7 MS-MS Spectral Data

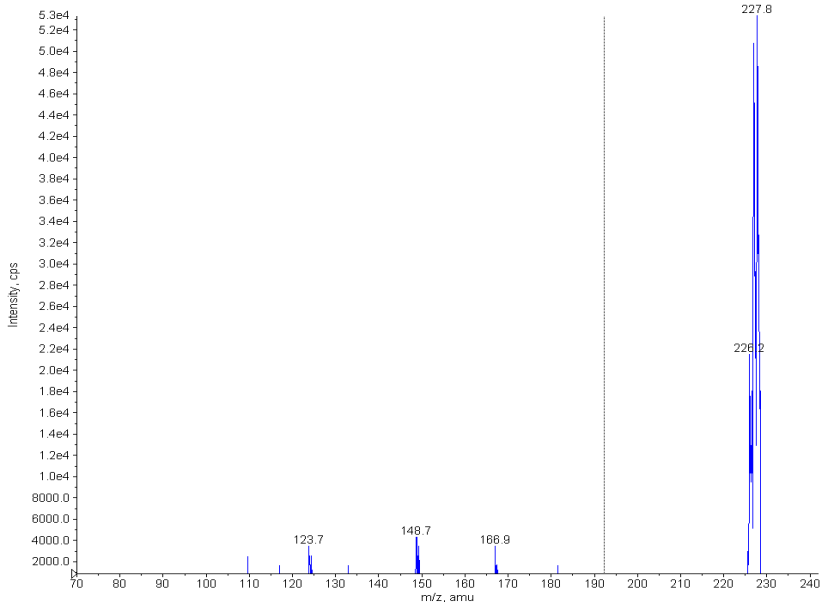

Figure A.11: MS-MS spectrum of intermediate **1**.

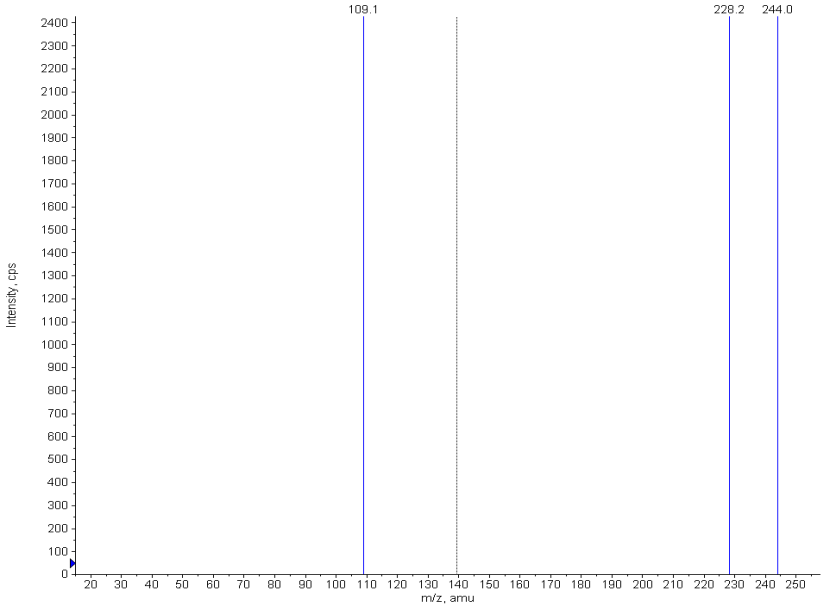

Figure A.12: MS-MS spectrum of intermediate **2**.

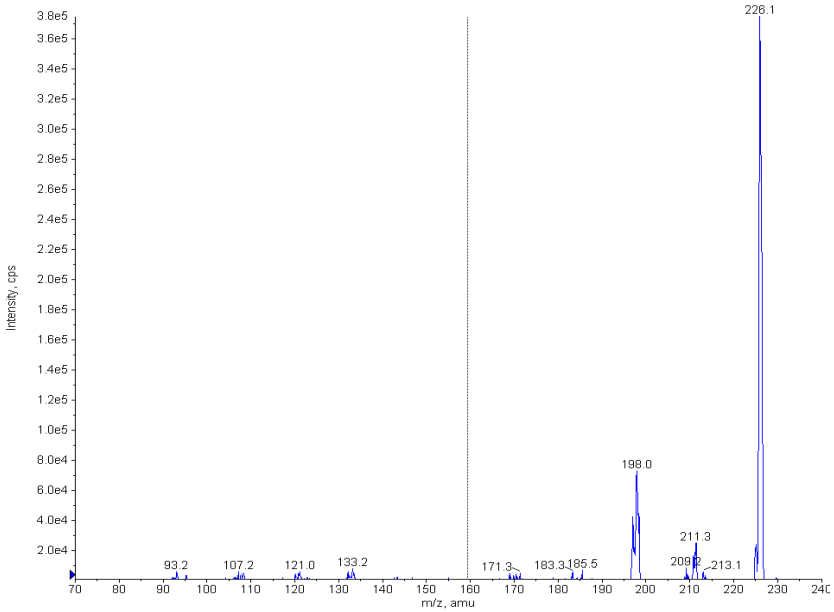

Figure A.13: MS-MS spectrum of intermediate **3**.

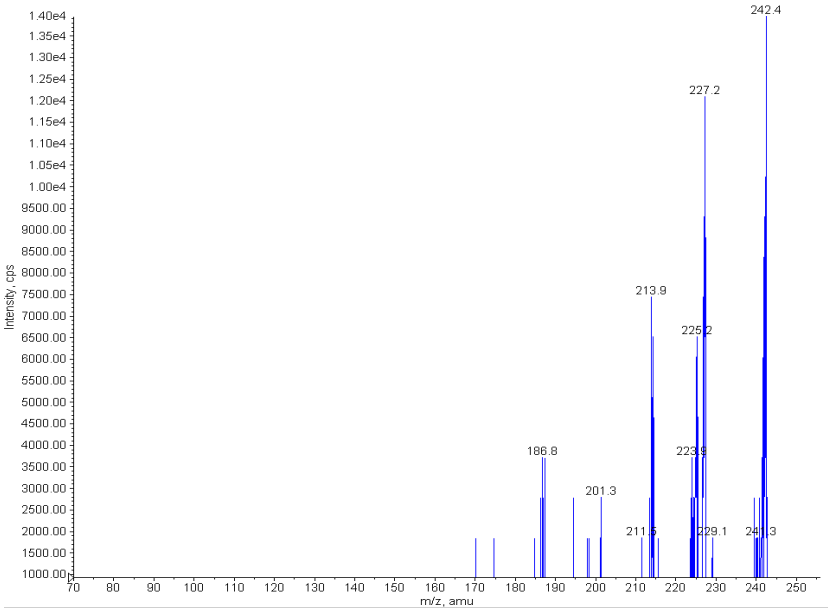

Figure A.14: MS-MS spectrum of intermediate **4**.

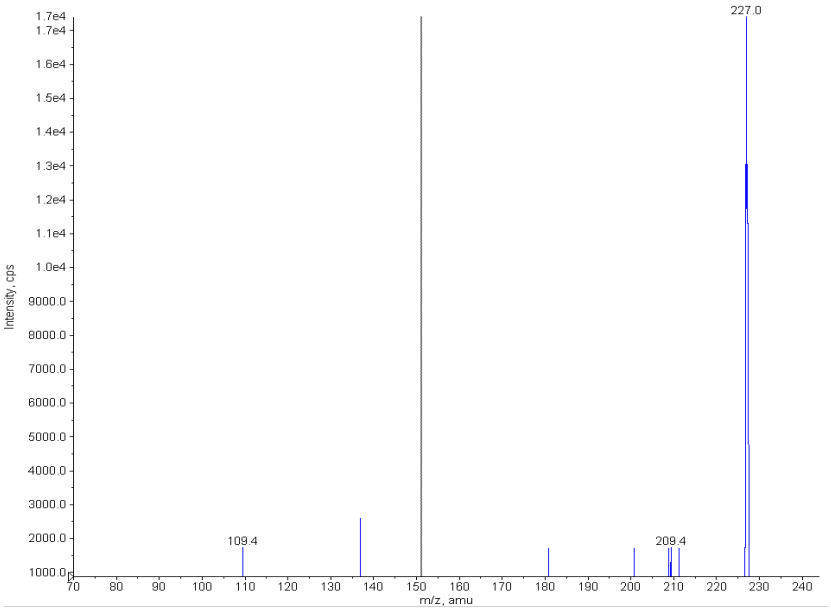

Figure A.15: MS-MS spectrum of intermediate **5**.

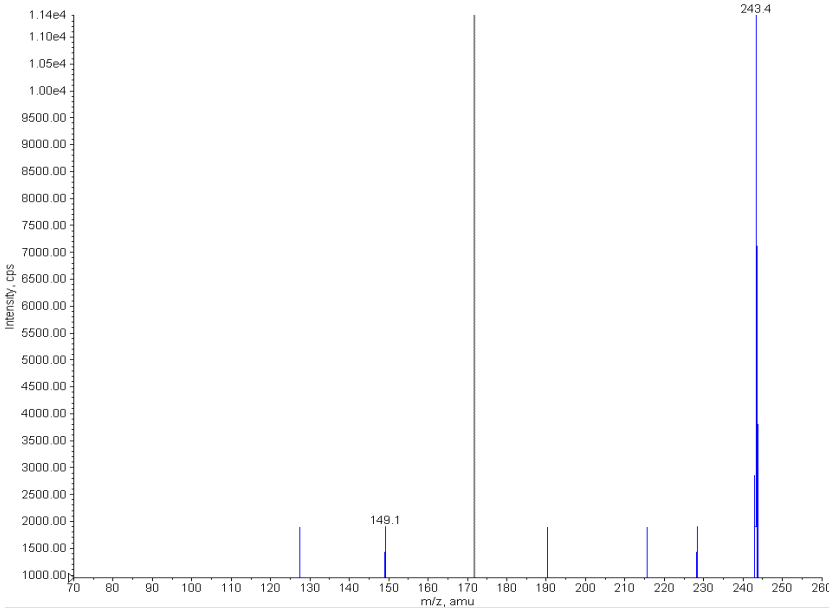

Figure A.16: MS-MS spectrum of intermediate **6**.

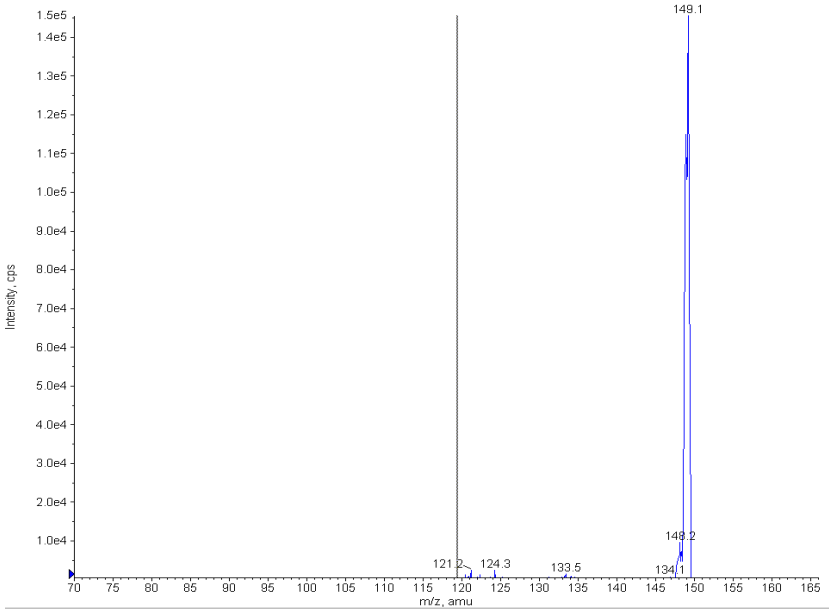

Figure A.17: MS-MS spectrum of intermediate **7**.

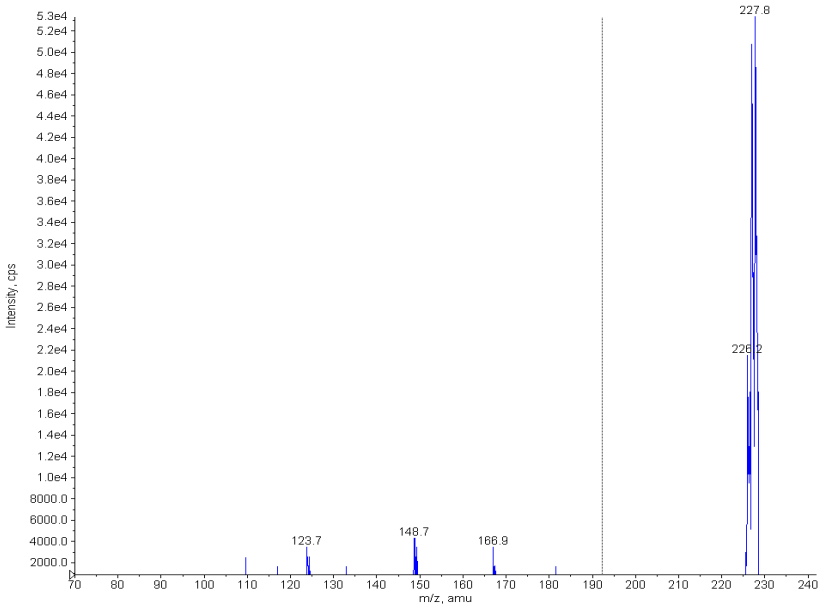

Figure A.18: MS-MS spectrum of BPA catechol.

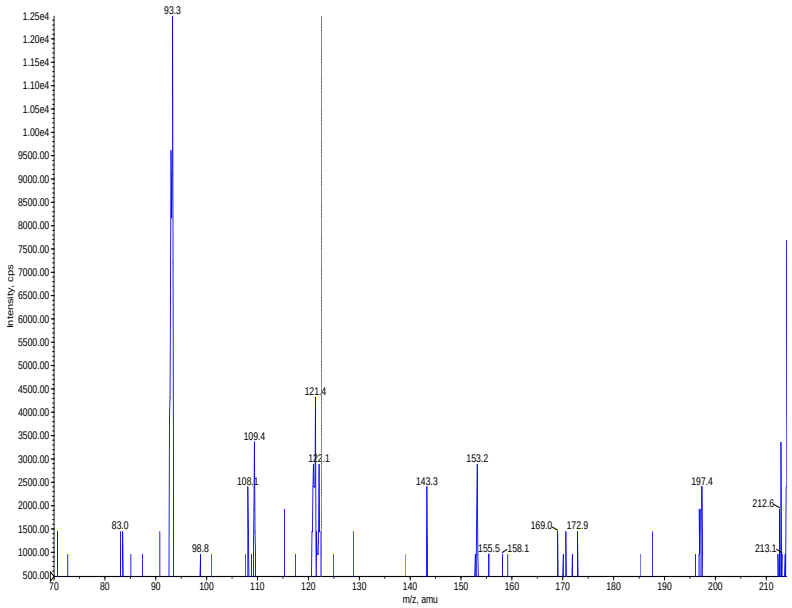

Figure A.19: MS-MS spectrum of BPF catechol.

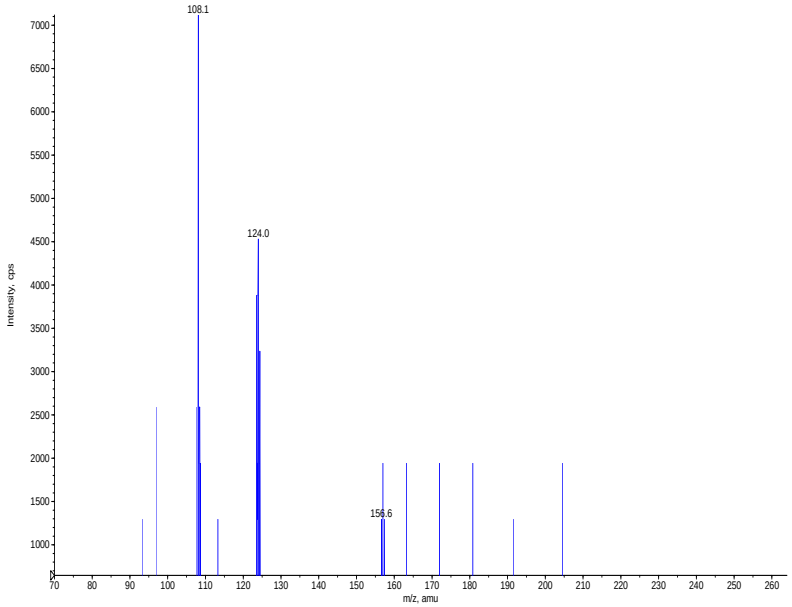

Figure A.20: MS-MS spectrum of BPS catechol.

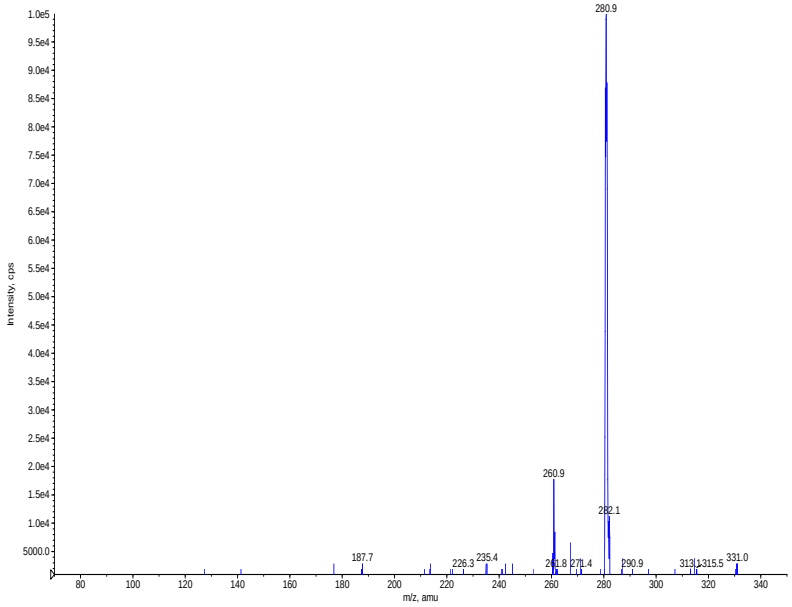

Figure A.21: MS-MS spectrum of BPAF catechol.

B

B.1 Publications

- Kondrakov A. O., Ignatev A. N., Frimmel F.H., Bräse S., Horn H., Revelsky I. A. Formation of genotoxic quinones during bisphenol A degradation by TiO_2 photocatalysis and UV photolysis: a comparative study. *Applied Catalysis B: Environmental*, **2014**, *160*, 106-114.

Selected Proceedings

- Kondrakov A. O., Ignatev A. N., Delay M., Frimmel F.H., Bräse S., Horn H., Bräse S. Quantification of the hydroxyl radicals, electron/electron-holes and oxidative reactive species generated in UV-illuminated aqueous TiO_2 suspensions by kinetic modeling of methanol photocatalytic degradation. *Wasser 2013 GDCh Conference*, **2013**, May 8-10, Goslar, Germany.

- Kondrakov A. O., Ignatev A. N., Frimmel F.H., Bräse S., Horn H. Diverse reaction pathways of photocatalytic elimination of bisphenol A in aqueous suspensions of titanium dioxide: kinetics modeling study and identification of intermediates. *IOA-EA3G Conference*, **2013**, April 23-24, Berlin, Germany.

B.2 Acknowledgements

This work has been done at the Chair of Water Chemistry and Water Technology of the Engler-Bunte-Institute at the Karlsruhe Institute of Technology (KIT) between January 2012 and December 2014 under the financial support of the bilateral research program of the state Baden-Württemberg "ZO IV – Innovation und Exzellenz: Beherrschung komplexer Systeme".

I dedicate my greatest appreciation to Prof. Dr. Fritz H. Frimmel, Prof. Dr. Igor A. Revelsky, Prof. Dr. Stefan Bräse and Prof. Dr. Harald Horn for the opportunity to participate in the ZO IV program and to carry out this study at the KIT. I greatly acknowledge the continuous support of all the scientific advisers of this work, namely of Dr. Alexander I. Revelsky, Dr. Alexey N. Ignatev, Dr. Alexey B. Tarasov and Dr. Dmitry A. Chepelyansky.

I give my special thanks to Dr. Gudrun Abbt-Braun, Ursula Schäfer, Silvia Heck and Stephanie West for their constant organizational assistance. I would like to thank Axel Heidt, Elli Karle, Rafael Peschke, and Matthias Weber for all the measurements they conducted for this work. I am grateful to Dr. Marius Majewsky, Dr. Thomas Glauner, Dr. Marco Scheuer, Dr. Alexey S. Cherevan, Thiemo Zehle, Gaby Römling and Rosaura Etcheguia for their valuable contributions in the results of this study and for the successful work together. It was a pleasure for me, to work in a pleasant and prosperous atmosphere of the team of the Chair of Water Chemistry and Water Technology; many thanks to you all!

I am very grateful that Annika Völp was taking such good care of me and our newborn daughter Yelena during all the time I worked on the thesis. Her support has been of great help for accomplishment of my postgraduate study.